Application of 2-D Digital Image Correlation (DIC) method to Damage Characterization of Cementitious Composites under Dynamic Tensile Loads

by

Yiming Yao

A Thesis Presented in Partial Fulfillment
of the Requirements for the Degree
Master of Science

Approved July 2013 by the
Graduate Supervisory Committee:

Barzin Mobasher, Chair
Subramaniam Dharmarajan
Narayanan Neithalath

ARIZONA STATE UNIVERSITY

August 2013

ABSTRACT

The main objective of this study is to investigate the mechanical behaviour of cementitious based composites subjected dynamic tensile loading, with effects of strain rate, temperature, addition of short fibres etc. Fabric pullout model and tension stiffening model based on finite difference model, previously developed at Arizona State University were used to help study the bonding mechanism between fibre and matrix, and the phenomenon of tension stiffening due to the addition of fibres and textiles. Uniaxial tension tests were conducted on strain-hardening cement-based composites (SHCC), textile reinforced concrete (TRC) with and without addition of short fibres, at the strain rates ranging from 25 s^{-1} to 100 s^{-1}. Historical data on quasi-static tests of same materials were used to demonstrate the effects including increases in average tensile strength, strain capacity, work-to-fracture due to high strain rate. Polyvinyl alcohol (PVA), glass, polypropylene were employed as reinforcements of concrete. A state-of-the-art phantom v7 high speed camera was setup to record the video at frame rate of 10,000 fps. Random speckle pattern of texture style was made on the surface of specimens for image analysis. An optical non-contacting deformation measurement technique referred to as digital image correlation (DIC) method was used to conduct the image analysis by means of tracking the displacement field through comparison between the reference image and deformed images. DIC successfully obtained full-filed strain distribution, strain versus time responses, demonstrated the bonding mechanism from perspective of strain field, and corrected the stress-strain responses.

ACKNOWLEDGEMENTS

I would like to specially thank my advisor Dr. Barzin Mobasher, who provides me the opportunity to work in the field of research that I could go through variety of excited topics and experimental programs. Let alone all the attention, invaluable intellectual insights he gave me. I also want to extend my appreciation to Dr. Subramaniam D. Rajan and Dr. Narayanan Neithalath who served as my committee members, helping and supervising my progress in Master's degree program.

I would also like to thank Dr. Amir Bonakdar, who actually taught me many skills including preparing and conducting experiment, data analysis and all of his supports and ideas throughout my research work. Outstanding work done by my peers, Dr. Deju Zhu, Dr. Flavio de Andrade Silva, and Dr. Chote Soranakom established the basis and a straight forward path that I could follow up and extended my work to further areas.

I greatly appreciate the assistance provided by Mr. Peter Goguen and Mr. Kenny Witczak for all of their great works in the laboratory, especially the trouble-shooting and maintenance on testing devices. Without their help, I could definitely not finish my experiments.

Absolutely, I would express my gratitude to my dear colleagues and friend, Virkam Dey, Karan Aswani, and Robert Kachala for their help and more importantly, the great time we spent together.

To my grandmother, may god be with you

To my families and my girlfriend who always understand and support me

TABLE OF CONTENTS

Page

CHAPTER Page

CHAPTER Page

LIST OF FIGURES

Page

Page

Page

Page

Page

Page

LIST OF TABLES

Page

Page

1. INTRODUCTION TO HIGH SPEED TENSILE TEST METHODOLOGY AND DIGITAL IMAGE CORRELATION (DIC) METHOD

1.1 High Speed Tensile Test Methodology

1.1.1 INTRODUCTION

This part discusses the various components of a high speed testing system, uniaxial tensile response cementitious composites at high strain rates and image analysis of the tests. The components of the test set up in addition to test procedures, data reduction approaches, and material property calculations are described. The high strain rate testing system includes MTS 5 kip servo-hydraulic tensile testing machine, MTS FlexTest SE control panels, laser extensometer, force measurement and data acquisition system.

1.1.2 APPARATUS

The high strain rate testing system, shown as Figure 1.1, includes MTS 5 kip servo-hydraulic tensile testing machine, MTS Flex SE control panels, laser extensometer, and data acquisition system. Each of the components will be described in the following subsections. Schematic diagram of this testing system is shown in Figure 1.2.

Figure 1.1 High Strain Rate Testing System

1.1.3 MTS TEST MACHINE

MTS 5 kip servo-hydraulic test frame (Figure 1.3 (a)) operating in an open loop mode was used to perform high strain rate testing. The velocity of the stroke/actuator is controlled by the servo-valve (Figure 1.3(b)). Different velocities are manually obtained by opening the servo-valve to different levels. The more open the servo valve, the higher the velocity of the actuator. A slack adaptor (Figure 1.3(c)) is used to facilitate the specimen setup and allows the stroke to accelerate to the needed test speed before the specimen is loaded. The current system is capable of developing cross head velocity up to 550 inch/second.

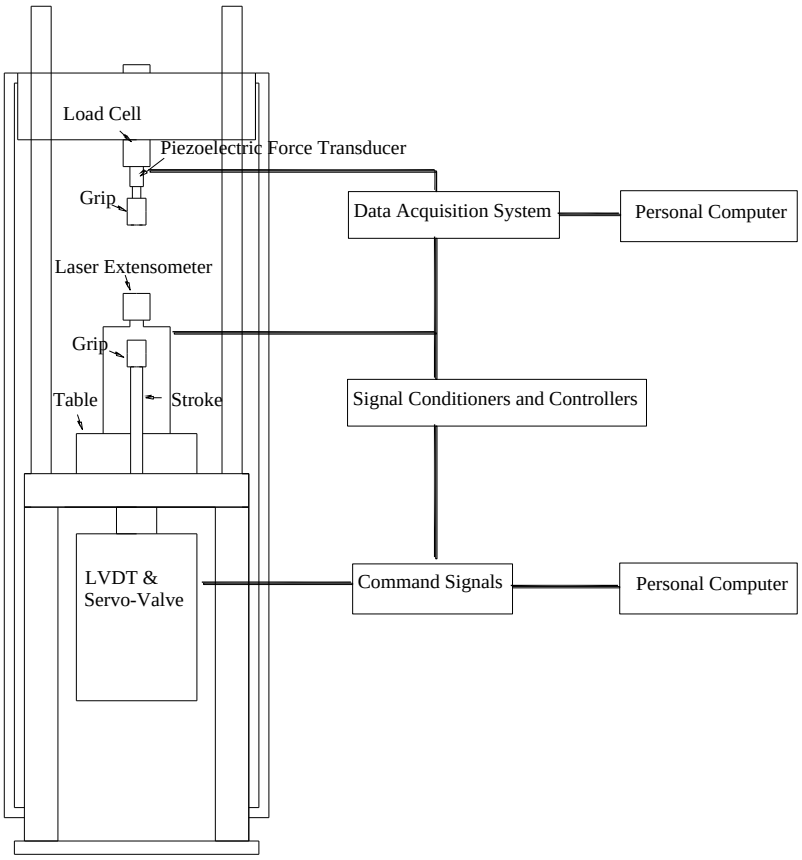

Figure 1.2 Schematic Diagram of Testing System

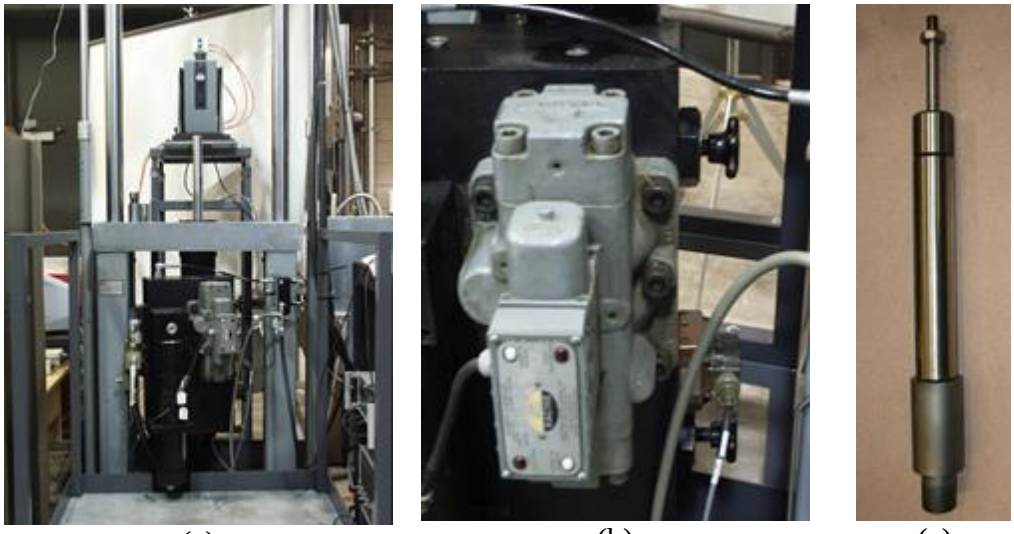

(a) (b) (c)

Figure 1.3 (a) MTS Testing Machine (b) Servo-Valve (c) Slack Adaptor

1.1.4 SIGNAL CONDITIONERS AND CONTROL PANELS

1.1.4.1 FlexTest SE Controllers

A state-of-the-art new MTS FlexTest SE control panels (Figure 1.4 (a)) and HP computer (Figure 1.4 (b)) for controlling the testing machine have been installed and calibrated.

(a) (b)

Figure 1.4 (a) MTS FlexTest SE Controller (b) HP Computer

1.1.4.2 Dual Charge Amplifier

A Kistler 5010B dual charge amplifier (Figure 1-5) is used for conditioning the signal from the piezoelectric force transducer. Details are presented in the force measurement section.

The charge amplifier type 5002 is a DC amplifier with very high input impedance and capacitive negative feedback, intended to convert the electric charge from a piezoelectric transducer into a proportional voltage on the low impedance amplifier output. The calibration factor setting (adjustment of transducer sensitivity of the amplifier) makes it possible to standardize the amplifier

sensitivities. The overall measuring ranges of the charge amplifier are given in pC for each 10V output voltage. However, the range in practice is given differently – as mechanical units per volt of output voltage making allowance for the sensitivity of the connected transducer (calibration factor, expressed in pC per M.U.).

Figure 1.5 Dual Charge Amplifier

There are three different options for time constants (long, medium and short) on the charge amplifier. The time constants are determined by the bleeder resistance and the range capacitor, and so are dependent on the measuring range. The time constant in the negative feedback circuit causes an exponential discharge of the range capacitor. The calibration factor calculated at long time constant is used in this study. It starts with the fact that all charge amplifiers have some drift on the output voltage. This drift is re-zeroed every time the reset/operate function on the amplifier is used. However, there are instances when it is not possible to use reset the control drift. If the time period is long enough, amplifier drift may

accumulate to produce an unacceptable offset in the signal. Enabling a time constant constrains the drift rate. This is because a time constant is effectively a high-pass filter and a linear drift has zero frequency and is thus blocked by the filtering action. The pulses, being high frequency, transmit right through the filter without distortion.

1.1.4.3 High Rate Control Panel

To obtain the high speed function of the MTS machine, a high rate control panel is needed (Figure 1.6). The switch with the key on the left side is used to select the closed loop option or the high rate option. For the current high strain rate testing, the switch is also set at high rate option. The blue button is the actuator reset button which resets the actuator/stroke to original position after test. The yellow button is the arm button that indicates the system is ready for high rate test when it is lit. When the arm button is pushed down, the red button on the right side of the panel is lit. The red fire button triggers the high rate test when pushed down.

Figure 1.6 High Rate Control Panel

1.1.5 GRIPPING SETS

To ensure low inertial forces in the high strain rate testing, it is important to maintain the weight of the grips as low as possible while ensuring a rigid attachment of the specimens to the grips. A new gripping system for dynamic tests was

designed using internal wedges that were held inside the female portion of screw connectors. The grip wedges and gripping arrangement are shown in Figure 1.7 and Figure 1.8. The total weight of the grip system is 6.8 lb. Four steel wedges (1.0" wide, 2" long) are used to grip the specimen at both ends. The entire length of the wedge grip faces was serrated in order to improve the contact with the test specimen. These wedges are housed inside hollow connecting rods. The grip was tightened by turning the screw assembly that pushes the grip against two slanted surfaces inside the wedge. Furthermore, care must be exercised to ensure that there is no relative sliding of the two faces of the grip as the wedge components slide and tighten.

(a)

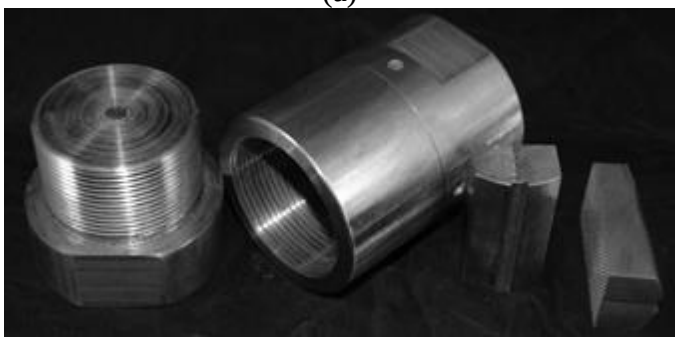

(b)

Figure 1.7 Stainless steel parts used for gripping a) thin specimen such as pure fabrics and aluminum sheet and b) thick composites

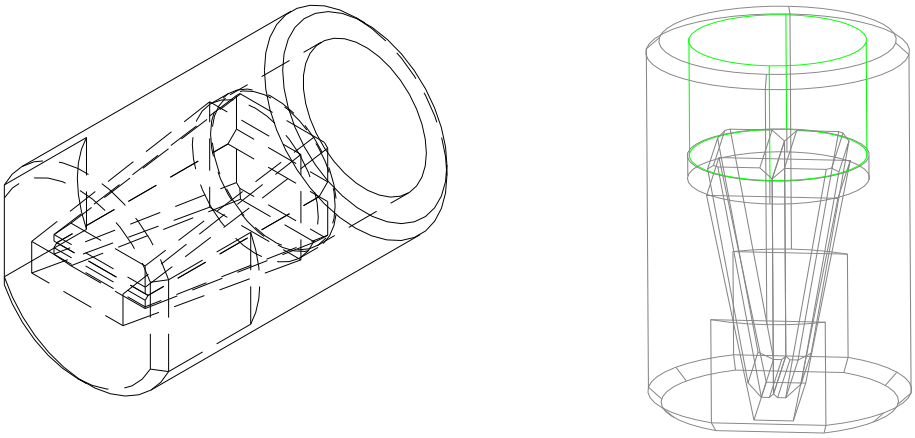

Figure 1.8 Schematic of Grip Set

1.1.6 FORCE MEASUREMENT

Strain gage based load cells are too soft and compliant at high strain rates. The frequency response of a standard load cell may not be sufficient to detect and measure the events which occur in a short duration.

Figure 1.9 Piezoelectric Force Transducer

A piezoelectric force transducer that is significantly stiffer than the conventional load cells will be used for high strain rate testing. In the current testing, the force was measured by a Kistler 9041A piezoelectric force transducer (Figure 1.9) with a capacity of 90 kN and rigidity of 7.5 kN/μm and frequency response of 33 kHz.

The piezoelectric force transducer is connected to the charge amplifier as discussed in previous section to generate the force measurement in terms of analog voltage output for the data acquisition purposes.

1.1.7 DATA ACQUISITION

A 4-channel data acquisition card has been installed on another computer that is used only for data acquisition purpose. Using this new PCI.X (66 MHz / 32 bit PCI card) data acquisition card, data can be continuously transferred to the PC host at 200 MBytes/s with four data channels. The card has 64 MBytes (32 M Samples) memory as standard and can operate at the maximum sampling rate of 10 M/s. All the four channels on the data acquisition card (Figure 1.10) are used to acquire the electrical signals. Two of the channels provide sinusoidal wave signals from laser extensometer, one is analog output from piezoelectric force transducer and one is analog output from LVDT/stroke.

Figure 1.10 Four-Channel Data Acquisition Card

The two connections on the left side are for external triggers that are not used in the current test. The internal trigger function of the card is used for triggering the test event. Using SBench 5.3 software system, the signals from four

channels stored in the onboard memory can be displayed on the computer screen and digitized and exported as ASCII files.

As the trigger is pushed, the actuator accelerates to reach and maintain the preset speed. During this range of travel, the conical portion of the slack adaptor contacts the actuator and transfers the force to the specimen. The slack adaptor consists of a sliding bar with a conical end that travels within a hollow tube with a matching conical fitting. The hollow tube travels freely with the actuator at the specified velocity before making contact with the sliding bar. This eliminates the inertial effect of the actuator and the lower grip during the acceleration stage. However, the sudden engagement with the upper portion of the setup generates a high amplitude stress wave, causing oscillations at the system's natural frequency [46]. To reduce the inertia effect, lightweight grips are recommended in dynamic tensile tests [59]. The stainless steel grips are shown in Figure 1.7 and weigh approximately 1500 grams (for gripping textiles) and about 2500 grams (for gripping TRC samples). Specimens are installed between two steel wedges with serrated faces. Piezoelectric load washers are recommended for dynamic tests because conventional load cell has a much lower response frequency.

1.1.8 Data Processing

The signals from the piezoelectric force-link and the LVDT of actuator were recorded at a sampling rate of 250 kHz and contained high frequency noise which was filtered using a low-pass filter with cut-off frequency of 3 kHz to obtain the specimen response. An example of the recorded responses of textile-reinforced

cement composite generated by the high speed testing setup after applying the low-pass filter is given in Figure 1.11. The figure presents the recorded force (in volts) versus time (in seconds) of the entire test. Due to the resistance provided by the test specimen, the test duration took less than 3 milliseconds at an average velocity of 2500 mm/s.

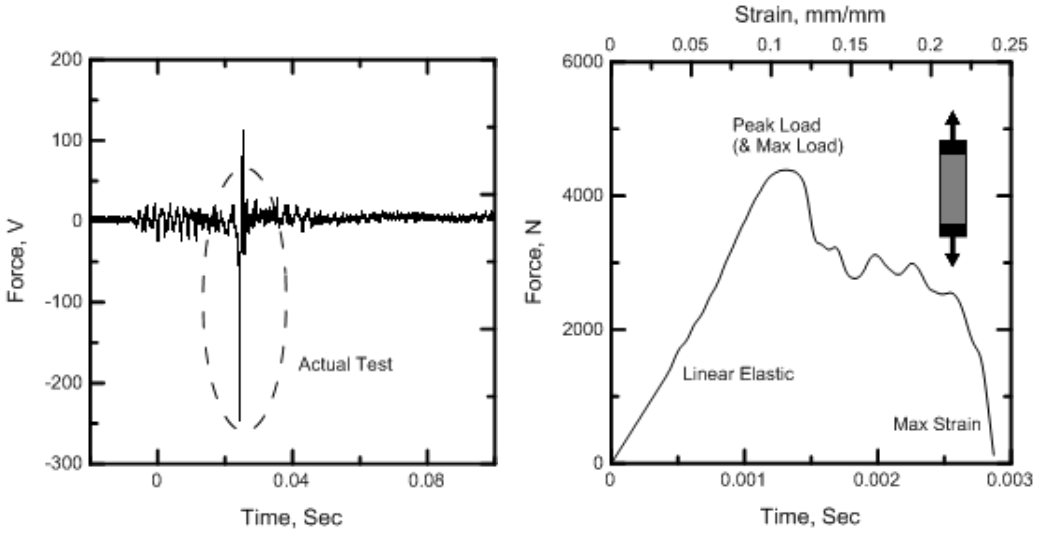

(a) (b)

Figure 1.11 Tensile force is plotted vs. time: a) entire test period and b) actual test period

Figure 1.11b shows a closer observation of the force response and the corresponding displacement history of the same sample during the actual test. The starting point of loading was used as the zero time (t=0). The strain rate is defined as the slope of displacement -time curve divided by the gauge length of test specimen. Using the cross sectional area and gage length of the specimen, the nominal stress versus strain curve can be calculated. Toughness is evaluated using the total area under the stress–strain curve. The stress–strain curves were calculated for all specimens and the Young's modulus, tensile strength (peak stress),

maximum strain and toughness. The reported results reflect the average and standard deviation values of each set.

1.2 Digital Image Correlation (DIC) method

1.2.1 Introduction and applications

In the past decades, contacting deformation measurement techniques and devices including linear variable differential transformer (LVDT) and electrical-resistance strain gage were widely used in the field of experimental mechanics. However, both LVDT and strain gage only measure the displacement or strain at isolate locations that the deformation behavior of materials are not fully investigated. Additionally, the experiments are limited by disadvantages of these methods including the effective working range, which results in varieties types of LVDT and strain gages; environments such as the effect of temperature on strain gages; extra effort in experiment preparation like soldering, wiring and mounting; extra cost due to the disposable devices. Thus there is a demand on newer measurement techniques. Optical techniques such as moiré interferometry [1], holography [2] and speckle inteferometry [3] have been proven to be matured techniques to analyze macroscopic parameters and are being applied successfully in many different applications. However, all the interferometric techniques have stringent requirements for system's stability. Moreover, the processing of fringe patterns is laborious and time-consuming [4]. This technical difficulty has raised many researchers' attention and computerized procedures [5] have been developed to automate the processing of the data from the fringe patterns.

In the thirty years, a non-contacting optical technique, digital image correlation, has been developed by Sutton et al. [6, 7, 8, 9] and Bruck, et al. [10]. As of recent years, DIC was widely applied to measurement of displacements and strains in many fields such as material science, mechanical engineering, biomechanics and structural engineering. The applications include strain measurements for anisotropic plastic deformation during tension testing [11], strain measurements in a CuAlBe shape memory alloy [12], analysis of glassy polymer networks under uniaxial compression test [13], determination of displacement distributions in bolted steel tension elements [14], deformation measurement of fiber composite pressure vessel [15]. Besides the applications on full-field deformation measurement, DIC has also been used for many other further purposes including the investigation of the bond between FRP and masonry [16], evaluation of kissing bond in composite adhesive lap joints [17], tracking fatigue damage evolution of fiber reinforced composites [18], calibrating the constitutive models of steel beams subjected to local buckling [19], etc.

On the other hand, DIC technique can also be used together with other measurement method. For example, Rouchier et. al [20] conducted the damage monitoring in fibre reinforced mortar by combined DIC and acoustic emission; damage in CFRP composites was conducted by Goidescu et. al [21] using DIC, infrared thermography and X-ray tomography. He et. al [22] characterized the nonlinear shear properties for composite materials based on a combination of finite element method for stress calculation and DIC for measurement of deformation. The combination not only improved the accuracy of material properties but also

provided an opportunity to extract material properties from experiments where the stress and strain fields are non-uniform and simple stress approximation is not feasible, reported by authors.

However, the deformation measurements of cement based composites tested under dynamic loads using DIC method is very limited. Koerber et. Al [23] characterized the unidirectional carbon-epoxy IM7-8552 in transverse compression and in-plane shear, both under quasi-static and dynamic tests at strain rates up to 350 s^{-1}. Full-field strain measurement was conducted using DIC method, the process of in-plain shear and off axis compression failure modes was monitored and the fracture angle was measured. Silva et. al determined the displacement field and calculated spacing for sisal fiber cement composites under direct tension tests at strain rates ranging from 5.5×10^{-6} to 24.6^{-6} [24]. Different displacement levels were also observed after the first crack formation. The DIC process was conducted using a MATLAB code developed by Mobasher et. al [25], while the analysis was performed again using a more advanced tool in present paper.

1.2.2 DIC discipline

Digital image correlation is no exception, and algorithms are employed that take the physics of the underlying deformation processes into account [26]. Due to the miniscule motions that are often of interest in engineering applications, the resolution requirements are much higher than for most other applications. To accurately measure the stress-strain curve for many engineering materials, length changes on the order of 10^{-5} m/m have to be resolved. The algorithm developed by

Sutton et al. [6, 7, 8, 9] targeted towards providing high resolution with minimal systematic errors. At the same time, a state-of-the-art phantom high camera mounted with high quality lens manufactured by Nikon was employed in the research.

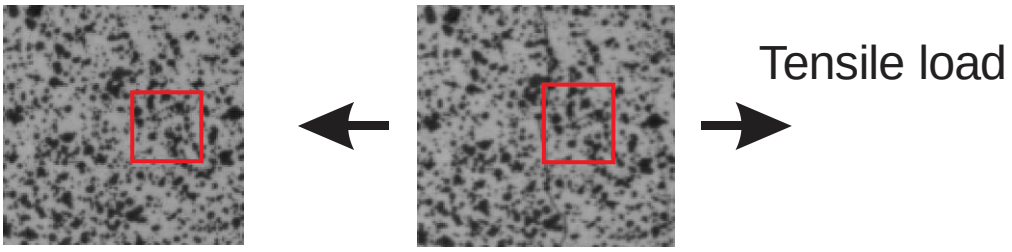

(a) (b)

Figure 1.12 (a) Reference image; (b) Deformed image.

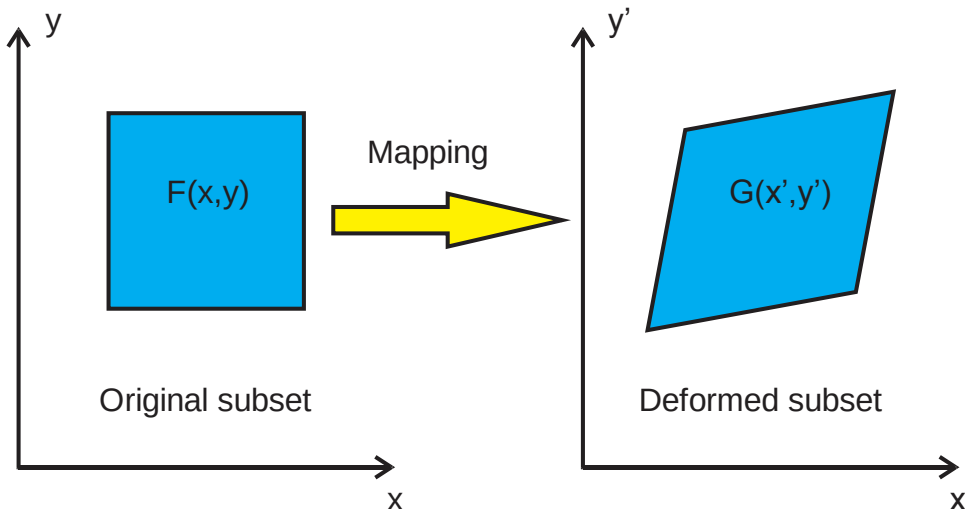

Figure 1.13 Principle of digital image correlation

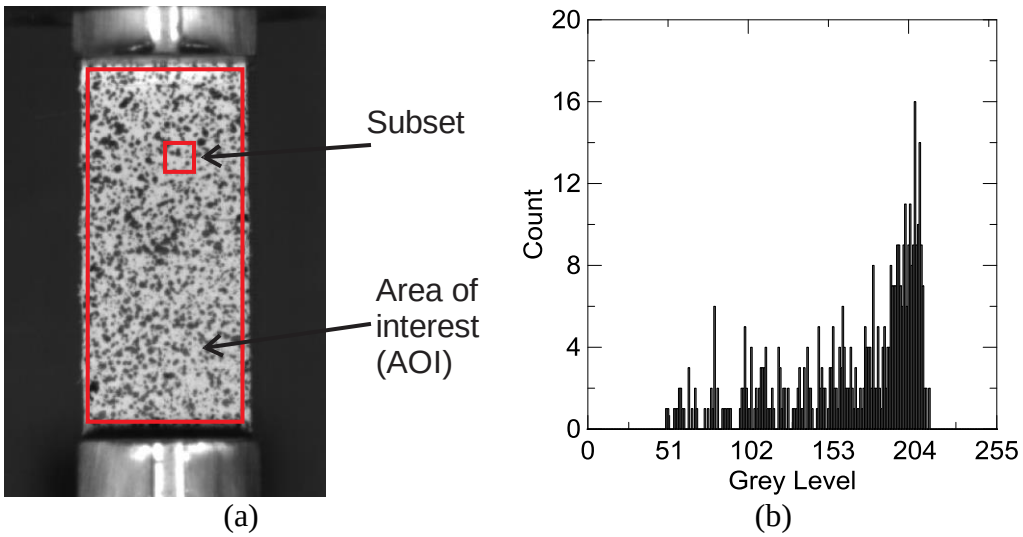

(a) (b)

Figure 1.14 Preferred speckle pattern; (b) Grey level distribution of the selected subset.

As shown in Figure 1.13, a reference image is taken before applying load and then a set of images are taken at sampling rate of 10,000 fps till the end of test. Deformation developed as the load increasing can be observed from the images taken after it starts, which is referred to as deformed images. As a result, the speckles at the surface of sample displace from their initial locations. These differences between speckle patterns can be calculated by correlating the pixels of the reference image and any deformed image. However, it is not possible to establish the correspondence of a single pixel in terms of grey scale level from one image to another. In order to address the correspondence problem uniquely, the object surface texture should be isotropic and non-periodic, i.e., it should not have a preferred orientation or repeating textures. These requirements naturally led to the use of random textures, such as the speckle patterns shown in Figure 1.15a. The pattern used in DIC adheres to the surface and deforms with it and therefore no loss of correlation occurs even under large deformations. One of the key features of

good speckle patterns is their high information content. Since the entire surface is textured, information for pattern matching is available everywhere on the surface, and not only on a relatively sparse grid. This permits the use of a comparatively small aperture for pattern matching, referred to as a subset, see Figure 1.15a. The principle to measuring the displacement of subset is to match the subset in reference image with that in deformed image by means of a mapping function (Figure 1.14), based on the detection of grey level distribution. Figure 1.14b shows an example of a gray level distribution for an artificial texture. Its histogram corresponds to a non-uniform distribution of gray levels. No significant saturation is observed and most of the dynamic range of the 8-bit camera is used. The grey level as a function of x and y of reference image F(x,y) and that of a deformed image G(x',y') are related by

$$G(x', y') = F(x, y + u(x, y))$$

Measurement of complex displacement fields is often an interest to engineering community; the specimen might experience elongation, compression, shear or rotation. An initially square reference subset might assume a distorted shape in a later image after deformation. This reduces the similarity between two subsets, which is often referred to as decorrelation. One of the significant advantages of DIC algorithm is that it is not only limited to determining pure translations but also can be easily extended to account for complex deformations. This is accomplished by introducing a subset shape function **ξ(x,p)** that transforms pixel coordinates in the reference subset in to coordinates in the image after

deformation. The squared sum of differences (SSD) cost function [26] can be written as

$$\chi^2(p) = \sum G\big(\xi(\mathrm{x},\mathrm{p})\big) - F(x))^2$$

Even under near ideal experimental conditions, there will be differences between the intensity of images recorded at different times, for reasons such as changes in lighting, specimen reflectivity due to the strain or changes in the orientation of the specimen. Thus it is significant to develop matching algorithms that can accurately measure the correct correspondence between subsets even if the intensity values undergo significant changes. The way to conduct template matching is to minimize the squared gray value differences between the reference subset and the subset after motion. The squared sum of differences (SSD) (Eq. (2)) is one of many optimization criteria that can be used for template matching, and indeed, gives the name of digital image correlation method.

$$\chi^2_{NCC} = \frac{\sum FG}{\sum F^2 \sum G^2}$$

The normalized cross-correlation criterion is bounded in the interval [0,1], and attains its maximum for perfectly matching patterns. Besides the basic principle discussed in this part, the solution to issues like changes in lightening was also addressed and integrated. Furthermore, optimization in computational efficiency of the algorithm and reduction of errors were conducted [26].

1.2.3 Testing setup and data flow

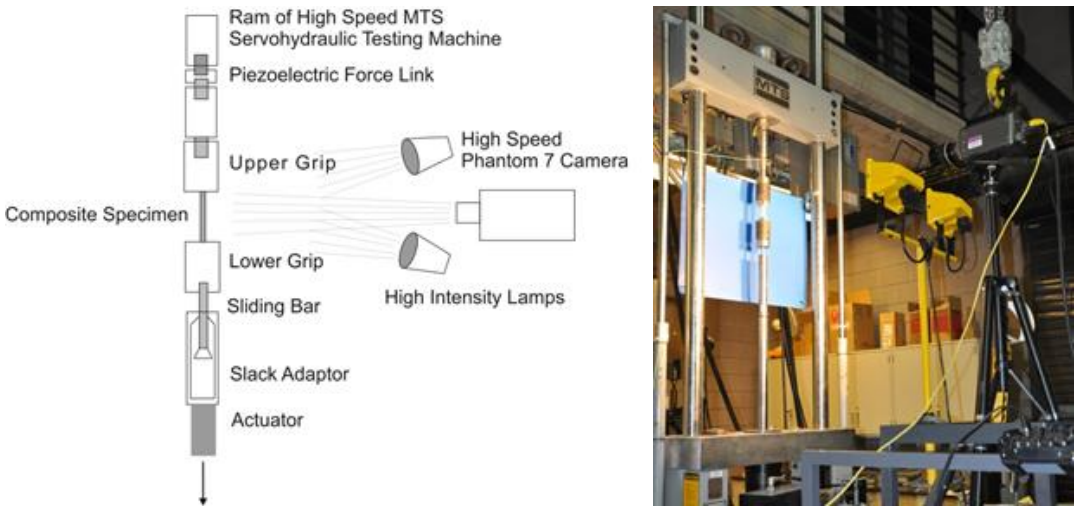

Figure 1.15 Schematic drawing and setup of the camera

A state-of-the-art phantom high speed camera was used to record the video at frame rate 10,000 fps, the setup is shown in Figure 1.11. The videos were converted to images using ImageJ with tagged image file format (TIFF). The images were analyzed using DIC method to obtain the results including full-field strain field, strain distribution over the length of specimen, strain versus time histories and stress-strain responses combining with the mechanical parameters. Figure 1.13 represents the flow chart of the procedure of testing and data processing.

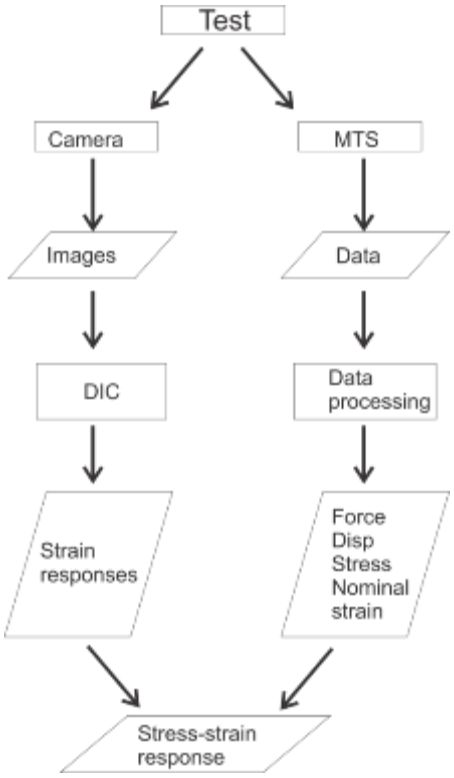

Figure 1.16 Flow chart of the testing and data analysis process

2. STRAIN RATE EFFECT ON THE TENSILE BEHAVIOR OF STRAIN-HARDENING CEMENT-BASED COMPOSITES (SHCC) UNDER DYNAMIC LOADING AND DEFORMATION MEASUREMENT BY DIGITAL IMAGE CORRELATION

2.1 Introduction

Strain-hardening cement-based composites (SHCC) reinforced by short PVA fibres constitute a relatively new class of building material, which exhibits pseudo-strain hardening behaviour with multiple cracking formation when tested under tension loads at quasi-static strain rates [27,28]. The high ductility and strain capacity of SHCC (also referred to as engineered cementitious composites (ECC) [29] are exceptional for cement-based materials. They give this material a marked potential for use in applications in which high non-elastic deformability is needed. Some examples of very promising applications are link-slabs for jointless bridge decks [30], structural repairs [31], and connecting beams for high-rise buildings in earthquake areas [32]. Specifically, RC beams repaired with SHCC showed no concrete crushing or spalling until final failure; improve moment strength and delay the time for reinforcement yielding; controlled the crack opening size [33].

Due to the ductility of SHCC, it might be expected that such material perform well when subjected to dynamic loading. On the other hand, the material's behaviour under high strain rates might be very different from that under quasi-static loading. Thus, the validity of stress-strain relations obtained in the quasi-static tests could be limited to low rate loading only. The use of such data in the analysis and design of dynamically loaded structures can lead either to overly cautious,

weighty designs or to premature structural failure. Examples of common dynamic loading in concrete structures are fast moving traffic ($\dot{\varepsilon}$ of 10^{-6} to $5{\cdot}10^{-4}s^{-1}$), gas explosions ($5{\cdot}10^{-5}$ to $5{\cdot}10^{-4}s^{-1}$), earthquakes ($5{\cdot}10^{-3}$ to $5{\cdot}10^{-1}s^{-1}$), pile driving (10^{-2} to $1s^{-1}$) and aircraft landing ($5{\cdot}10^{-2}$ to $2s^{-1}$) [34]. Blast loading, aircraft impact or impact by hard projectiles can produce strain rates much higher than the instances cited above. A proper understanding of the response of concrete-based materials to such loading is important to the correct design of structures against which industrial explosions, terrorist bombings, or military attacks may occur.

While there is still a lack of knowledge about the material behaviour of SHCC under strain rates above $1s^{-1}$, a few works have been published on its tensile behaviour at rates of up to $0.2s^{-1}$. Maalej et al. [35] tested hybrid-fibre SHCC containing a combination of high-modulus steel fibres and relatively low-modulus polyethylene fibres under tensile loading at strain rates ranging from $2{\cdot}10^{-6}$ to $0.2s^{-1}$. With increasing strain rate, the tensile strength increased almost by two times but no obvious changes in the strain at failure were observed. According to Yang and Li [36], similarly, with strain rate increasing from 10^{-5} to $10^{-1}s^{-1}$, the tensile strength of SHCC also increases by two times whereas the strain capacity decreased from 3% to 0.5%. Furthermore, Douglas and Billington [37] reported a 53% decrease in the strain capacity and a 12% increase in tensile strength of a SHCC tested at a strain rate of $0.2s^{-1}$ when compared to the results of quasi-static tests ($2x10^{-5}s^{-1}$). To explain these phenomena, discussion centred on a strengthening of the bond at the interface with increasing strain rate, which resulted in premature fibre failure. This suggests that no complete fibre delaminating from the matrix and subsequently

no fibre pullout occurred at high loading rates. Boshoff et al. [38] found additionally that the probability of fibre failure increased with increased loading rate. Furthermore, they showed by means of fibre pullout tests that an increase in the pullout rate could change the failure mechanism from gradual pullout to predominant fibre rupture.

There is limited publications with regard to very high loading rates Maalej et al. [35] studied the impact resistance of SHCC to projectiles. According to these results SHCC showed clearly beneficial behaviour in comparison to ordinary or high-strength concrete: increased shatter resistance with a nearly complete lack of scabbing, spalling, or fragmentation and much better energy absorption through distributed micro-cracking. Characterisation of the mechanical properties of SHCC was not the subject of that study. Due to the lack of studies, Mechtcherine et. al [39] investigated the tensile behaviour of SHCC both under static and dynamic loads, at strain rates ranging from $10^{-5}s^{-1}$ to $50s^{-1}$. An increase in tensile strength and a decrease in strain capacity was observed for tensile test performed at strain rates up to $10^{-2}s^{-1}$. In addition, the number of cracks at the composite failure decreased as the strain rate increased, and a predominance of fibre failure was observed at higher strain rates. When loaded at high strain rates ranging from 10 to $50s^{-1}$ in this study, SHCC showed an increase in both tensile strength and strain capacity with increasing loading rate. No pronounced multiple cracking was observed. However, the failure of the composite was accompanied by the pullout of most of the fibres crossing the macro-crack. In addition, the coupled strain rate and temperature effects on the tensile behavior of strain-hardening cement-based composites

(SHCC) with PVA fibers Mechtcherine et. al [40] after their previous work. It is observed that SHCC shows an increase in tensile strength and reduction in strain capacity as the strain rate is augmented from 10^{-5} s^{-1} to 10^{-2} s^{-1}, both at room temperature and 60 °C. However, the values of strain capacity at elevated temperature were much higher than those of room temperature.

The objective of the current work is to obtain more detailed knowledge of mechanical behaviour of SHCC under conditions of high-speed loading. With that in mind, uniaxial tensile tests on plate specimens were carried out at different strain rates 25^{-1}, 50^{-1}, and 100^{-1}. The full-field strain distribution was investigated by means of digital image correlation (DIC) method.

2.2 The experiment

2.2.1 Materials

The SHCC composition used in the present investigation is based on previous work by Mechtcherine et. al [28,40]. A combination of Portland cement 42.5 R and fly ash was utilized as binder. The aggregate was uniformly graded quartz sand with particle sizes ranging from 0.06mm to 0.20mm. PVA fibres in a volume fraction of 2.2%, measuring 12mm in length and 0.04mm in diameter (Kuraray Co., Ltd., Kuralon K-II REC15) were used as reinforcement. A super plasticizer on a polycarboxilate-ether basis (SP) and a viscosity agent (VA) were added to the mix in order to adjust its rheological properties.

Table 2-1 Mix proportions of SHCC under investigation.

Material	(kg/m^3)
Cement 42.5 R-HS (Heidelberger)	505.00
Fly Ash	613.54
Quartz sand (0.06-0.20 mm)	534.22
Viscosity Agent	3.20
Superplasticizer (Glenium ACE 30)	16.58
Water	324.01
SAP	2.02
PVA – 12 mm (2.2 %)	29.30

Table 2-1 gives the mix proportions of the material developed. In comparison to the reference mix presented in Mechtcherine and Schulze [28], the proportion of cement and fly ash was altered. Furthermore, a superabsorbent polymer (SAP) was used as a multi-tasking agent: (1) to reduce autogenous shrinkage, (2) to improve the frost resistance, and (3) above all, to introduce micro-defects, which are favourable with regard to inducing the formation of multiple cracks (see also Brüdern and Mechtcherine 2010).

The matrix was produced using a bench-mounted mixer of 20 litres capacity. The fines and sand were homogenized by dry mixing for 30s. Water mixed with one half of the super plasticizer was poured into the dry mix during 30s and mixed for an additional 60s. PVA fibres were added over a period of 30s and mixed for an additional 180s. The second half of the super plasticizer was added at this stage for

30s and mixed for another 180s. The mix was cast horizontally in steel moulds. The moulds were stored for 2 days in a room with controlled temperature (T = 25°C) and humidity (RH = 65%). After demoulding the specimens were sealed in plastic foil and stored at room temperature until testing.

2.2.2 Dynamic tensile testing of SHCC at different strain rates

The high-speed tensile tests were performed in a high-rate MTS testing machine. The setup and procedure of the dynamic tensile testing were addressed in Chapter 1[1.1]. The tension tests were performed at strain rates of 10, 25 and 50s^{-1}. Six specimens were tested for each strain rate.

Material parameters derived from the experimental data included tensile strength (peak stress), strain capacity (strain on reaching tensile strength) and work to fracture. Work to fracture was calculated using the total area under the stress-strain curve. Average value and standard deviation are given for each strain rate. Furthermore, tensile stress-strain curves of the specimens tested under static and dynamic conditions are compared.

2.3 Results and discussion

2.3.1 Strain rate effect on the tensile behaviour of SHCC

Figure 2.1 shows typical stress-strain curves obtained for the high strain rates (25s^{-1}, 50 s^{-1}, and 100 s^{-1}) on SHCC specimens. The strain-hardening effect was found to be very pronounced. The material parameters derived from the measured data are given in Table 2-2. An increase in both tensile strength and strain capacity (Figure 2.2b and c) was measured as the strain rate increased from 25 to

$100s^{-1}$ (see Table 2-2.). The tensile strength increases from 8.13MPa to 9.94MPa, while the strain capacity rises from 0.86% to 1.82%. As a result, work-to-fracture also shows an improvement with the increasing strain rate, from 1.15J to 4.12J (Figure 2.2d). This observation agrees with the results reported by Mechtcherine et. al [40], who investigated the tensile behaviour of dumbbell-shaped SHCC specimens under dynamic loads at strain rates ranging from 10 to $50s^{-1}$ and strain rate effect on pullout behaviour of PVA fibre. It is found that the increase in strain rate lead only to a moderate increase in fibre strength but at the same time to a considerable increase of the pullout resistance. What is more, fibre pullout dominates the failure mode at very high strain rates. These two phenomenon may together contribute to the increase in tensile strength as the strain rate increases. It is also reported that both pullout length and plastic deformation of PVA fibre increased at strain rats over $10s^{-1}$, which might result in the improvement in strain capacity and work-to-fracture of SHCC specimens tested at high strain rates.

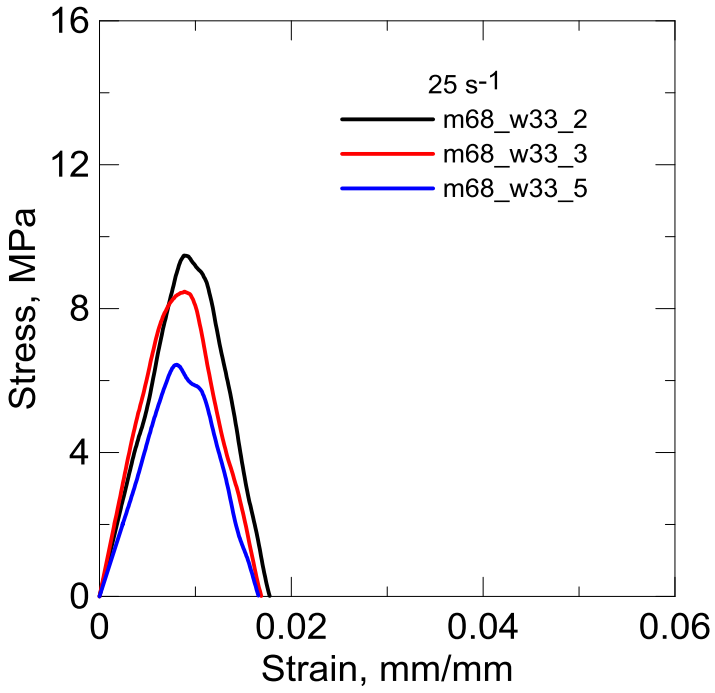
25 s-1
m68_w33_2
m68_w33_3
m68_w33_5
Stress, MPa
Strain, mm/mm
0
4
8
12
16
0
0.02
0.04
0.06

(a)

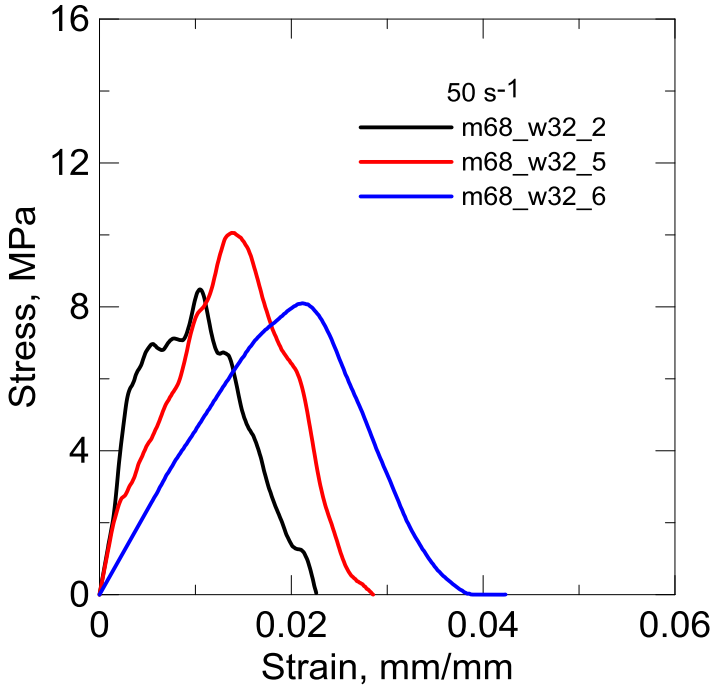
50 s-1
m68_w32_2
m68_w32_5
m68_w32_6
Stress, MPa
Strain, mm/mm
0
4
8
12
16
0
0.02
0.04
0.06

(b)

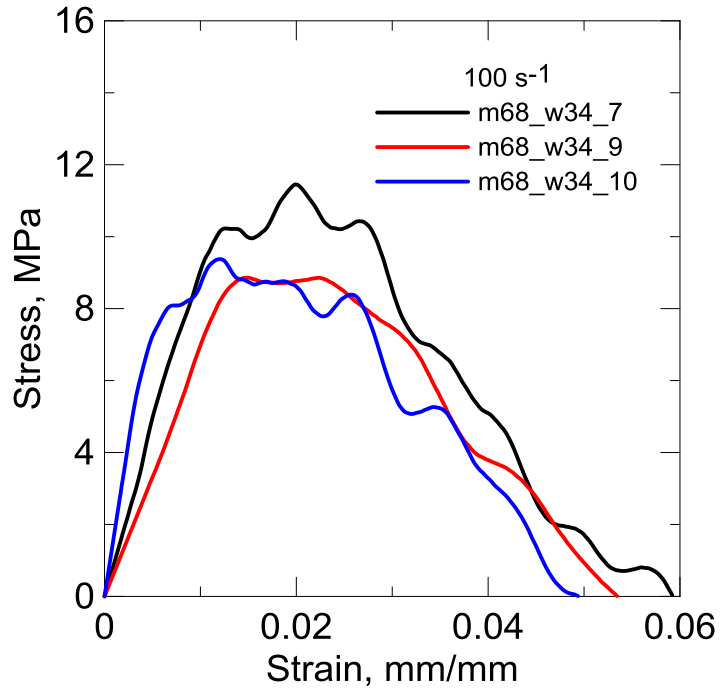

(c)

Figure 2.1 Representative stress-strain responses for SHCC specimens tested at (a) 25 s^{-1}, (b) 50 s^{-1}, and (c) 100 s^{-1}.

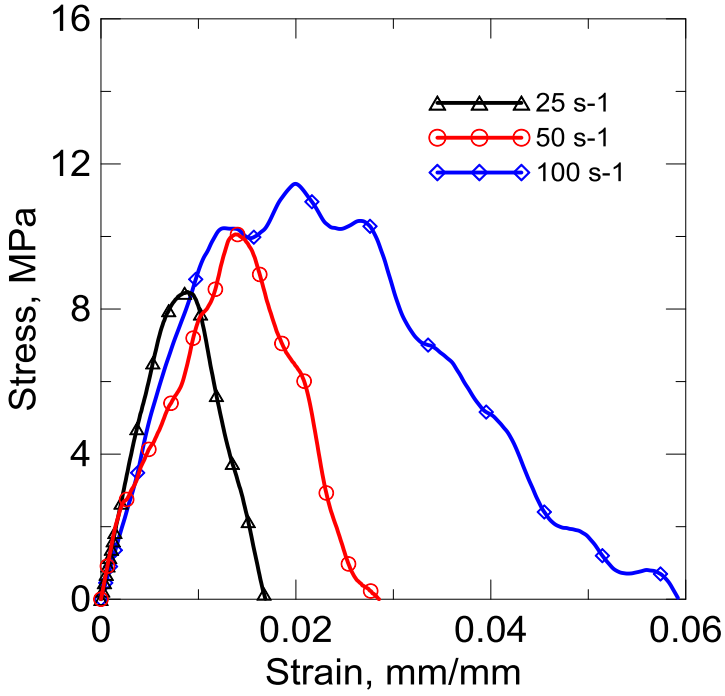

(a)

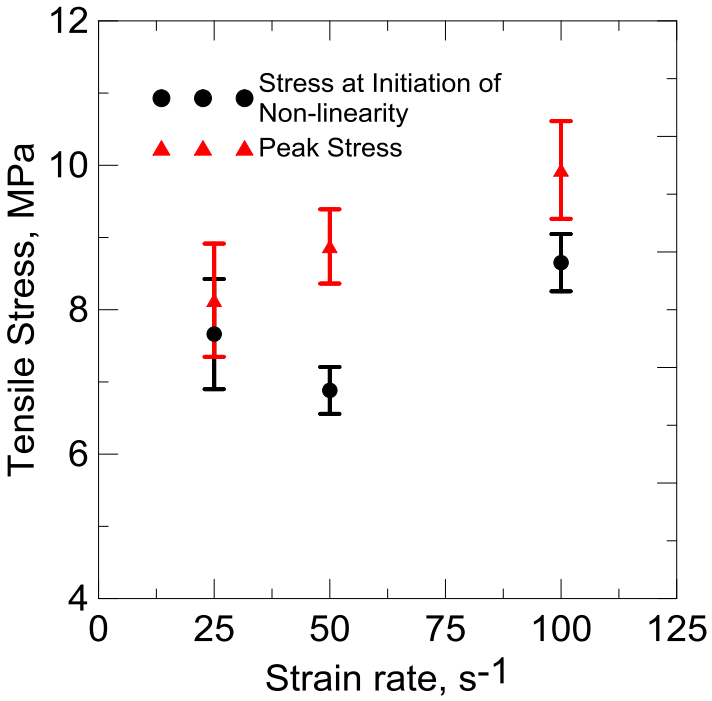
Stress at Initiation of Non-linearity
Peak Stress
Tensile Stress, MPa
Strain rate, s-1
12
10
8
6
4
0
25
50
75
100
125

(b)

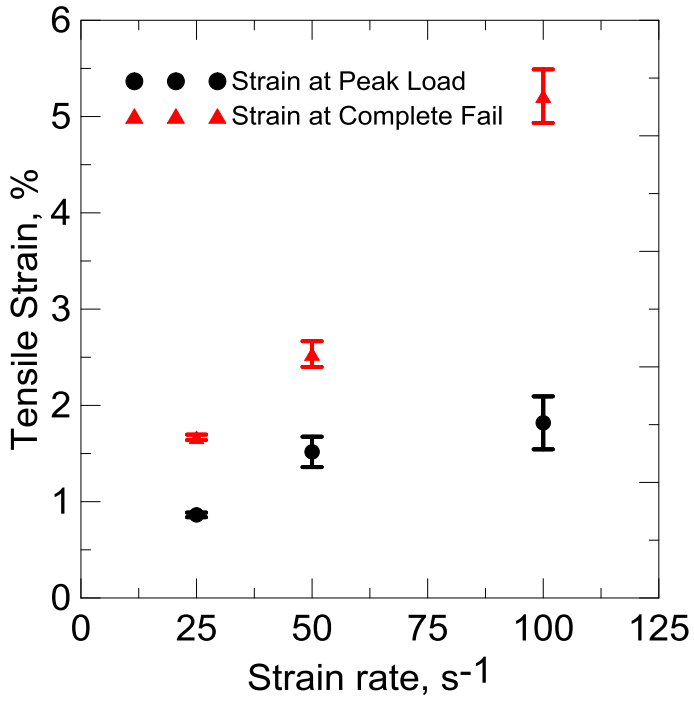
Strain at Peak Load
Strain at Complete Fail
Tensile Strain, %
Strain rate, s-1
6
5
4
3
2
1
0
0
25
50
75
100
125

(c)

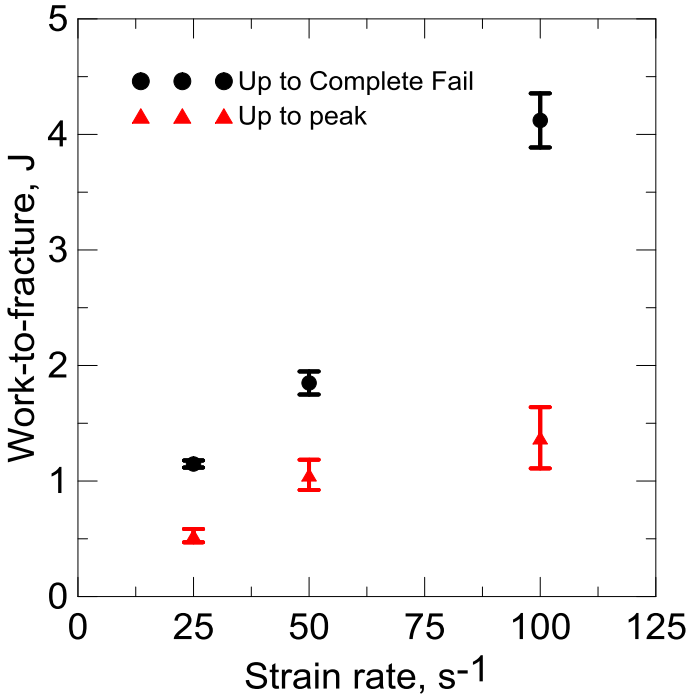

(d)

Figure 2.2 Effect of strain rate on the tensile behaviour of SHCC at high strain rates: (a) tensile stress-strain responses of SHCC, (b) effect of strain rate on the average tensile strength and tensile stress at initiation of non-linearity, (c) effect of strain rate on strain at peak load (strain capacity) and strain at complete fail (5% of maximum load in post peak), and (d) effect of strain rate on work-to-fracture up to complete and up to peak.

Table 2-2 Summary of high-speed tension test results; average results (standard deviations are given in parentheses).

Strain Rate	NO.	Tensile Strength (MPa)	Tensile Stress at initiation of non-linearity	Strain at peak (%)	Strain at 5% of maximum stress in post peak (%)	Work-to-fracture up to completion (J)	Work-to-fracture up to peak (J)
25	2	9.4907	9.2667	0.9010	1.7321	1.1901	0.5928
	3	8.4880	7.4907	0.8780	1.6475	1.0608	0.6235
	5	6.4160	6.2293	0.8090	1.6249	1.1909	0.3652
	AVG.	8.1316	7.6622	0.8627	1.6682	1.1473	0.5272
	STD. DEV	1.2803	1.2459	0.0391	0.0461	0.0611	0.1152
50	2	8.4747	5.6027	1.0510	2.2247	1.4571	0.8139
	5	10.0453	7.7120	1.3800	2.6808	1.9765	1.0142
	6	8.1093	7.3333	2.1200	2.6945	2.1122	1.3326
	AVG.	8.8764	6.8827	1.5170	2.5333	1.8486	1.0536
	STD. DEV	0.8399	0.9182	0.4470	0.2183	0.2823	0.2136
100	7	11.4693	9.5547	1.997	5.7884	4.6613	1.9858
	9	8.912	8.328	2.257	5.1694	3.8659	1.0581
	10	9.424	8.072	1.202	4.6774	3.836	1.0788
	AVG.	9.9351	8.6516	1.8187	5.2117	4.1211	1.3742
	STD. DEV	1.1048	0.6471	0.4488	0.4546	0.3822	0.4325

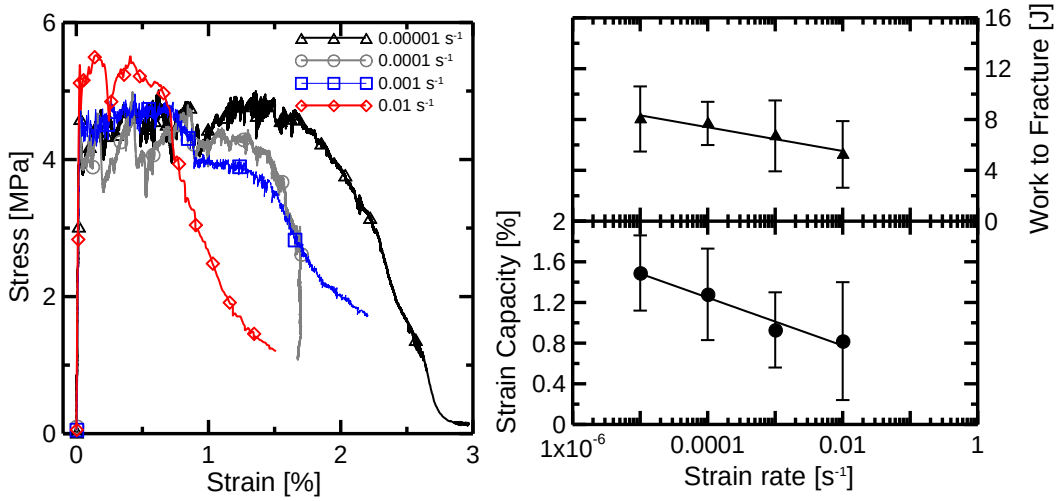

Figure 2.3 Effect of strain rate on the tensile behaviour of SHCC at low strain rates ($\leq 0.01 s^{-1}$): (a) tensile stress-strain responses of SHCC, (b) effect of strain rate on the strain capacity and work to fracture of SHCC [40].

To compare the high speed testing results with those of static tests, experiments conducted on dumbbell-shaped specimens at strain rates ranging from 10^{-5} to $10^{-2} s^{-1}$ [40] is referred, as shown in Figure 2.3. It can be seen that the shapes of the curves are significantly different from those obtained for high strain rates. However, the same trend of increasing in tensile strength was confirmed by each other. However, the strain capacity and work-to-fracture were found to be decreasing as the strain rates increased for static test. While the behaviour of SHCC under quasi-static tensile loading at the very low rate of $\dot{\varepsilon} = 10^{-5} s^{-1}$ was characterised by a rather pronounced strain-hardening response accompanied by multiple cracking, the SHCC response on higher, but still quasi-static rates (up to $10^{-2} s^{-1}$), revealed measurably less ductile behaviour and less multiple cracking. Similar rate dependence behaviour was also observed by Yang and Li [36] and Douglas and Billington [37]. Within this range of strain rates the increase in

strength and decrease in strain capacity is due to an increase in the bond strength between fibre and matrix according to reported pullout experiments performed at different strain rates [38]. As a result of the higher bond strength, fibre failure becomes more frequent, with a decrease in the frequency of fibre pullout, leading to a more brittle failure of the composite as a whole.

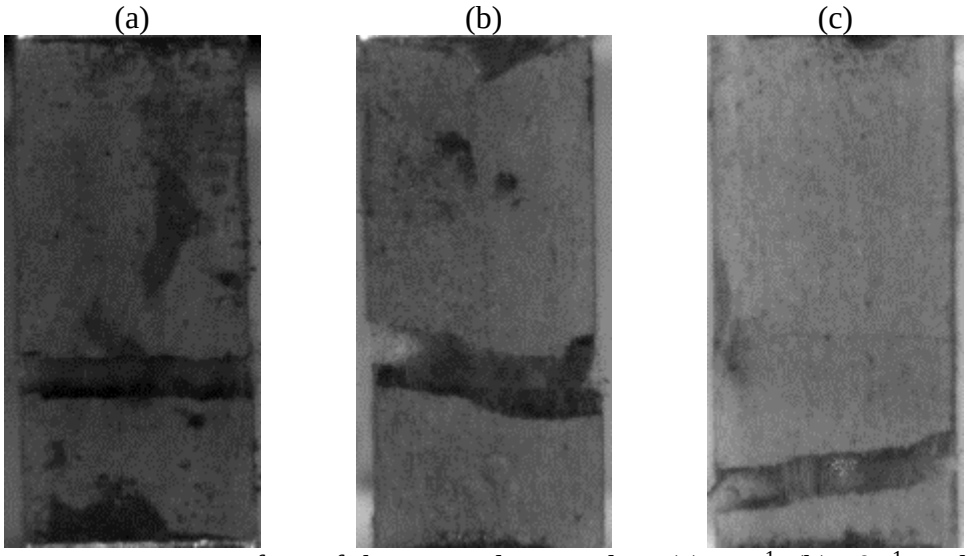

Figure 2.4 Fracture surface of three samples tested at: (a) $25s^{-1}$, (b) $50s^{-1}$, and (c) $100s^{-1}$, images taken by the high speed camera.

Figure 2.6 Illustrates the fracture surfaces of samples tested at high strain rates. One visible macro crack formed leading to the failure of the specimen. According to the microscopic investigation of the fracture surfaces using ESEM conducted by Mechtcherine et. al[40], the samples tested with strain rates of $10s^{-1}$ and higher showed a much more pronounced pullout length than with samples tested at strain rates of $10^{-2}s^{-1}$ or lower. The fibre pullout length measures several millimetres in specimens tested at the higher rate whereas the corresponding lengths observed for the specimens tested at $10^{-3}s^{-1}$ were considerably lower, less than

0.5mm in most cases. This can easily be traced back to the occurrence of pronounced fibre failure during the fast quasi-static tests.

2.3.2 Image Analysis

2.3.2.1 Strain field obtained from DIC

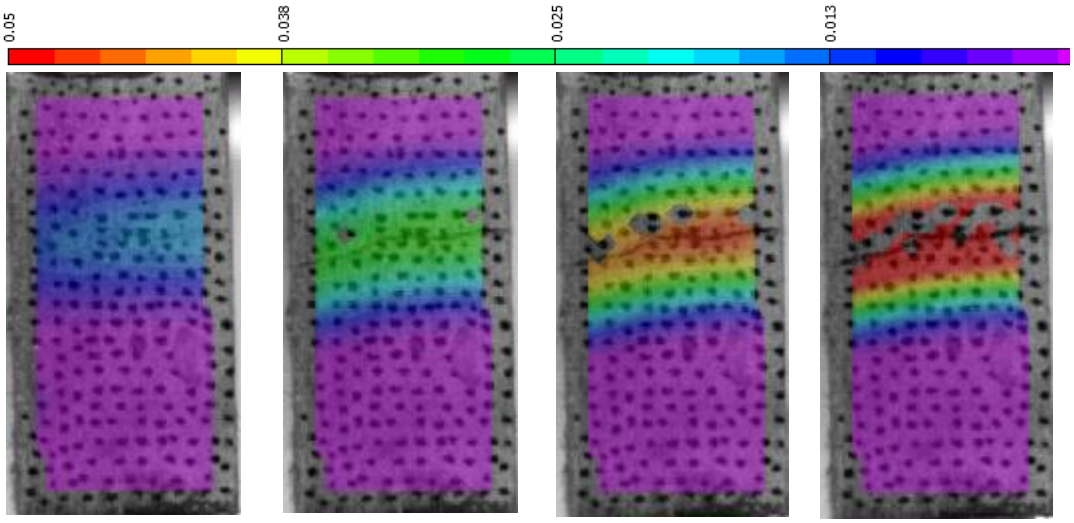

T = 0.2 ms T = 0.3 ms T = 0.4 ms T = 0.5 ms

(a)

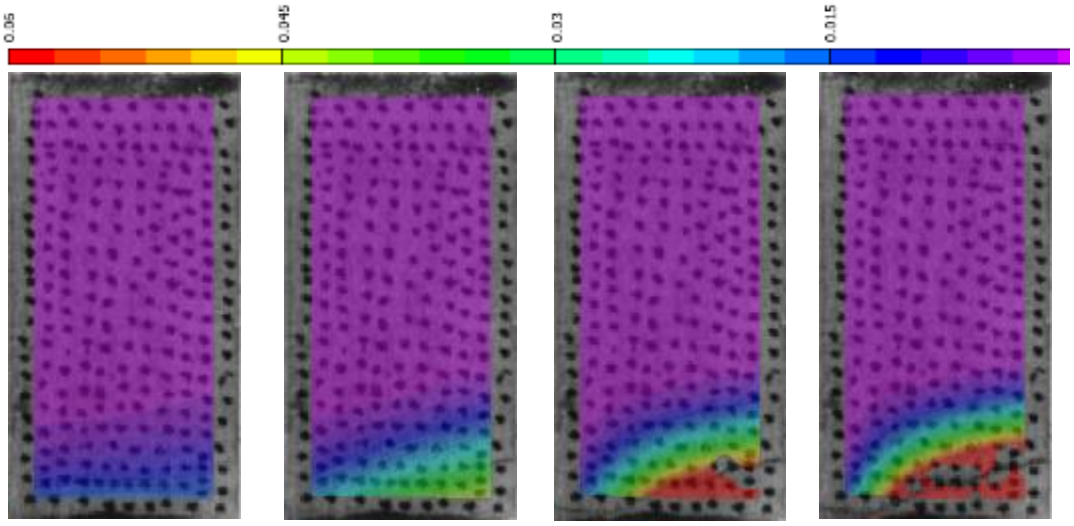

T = 0.3 ms T = 0.4 ms T = 0.5ms T = 0.6 ms

(b)

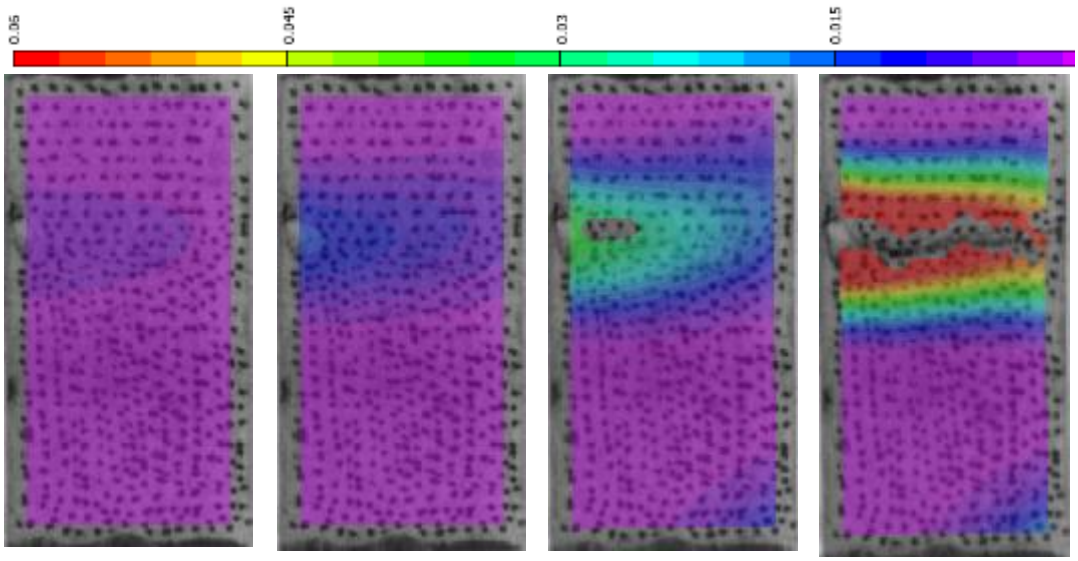

T = 0.1 ms T = 0.2 ms T = 0.3ms T = 0.4 ms

(d)

Figure 2.5 Strain field obtained from DIC method for SHCC specimens tested at (a) $25s^{-1}$, (b) $50s^{-1}$, and (c) $100s^{-1}$.

The strain field of SHCC specimens generated by the digital image correlation method is presented in Figure 2.7. It can be observed that a macro crack was formed either close to middle part (Figure 2.5a and c) or near the ends (Figure 2.5b), which leads to the failure of sample. The formation of macro crack is attributed to highly stress concentration, which is required to store enough energy to create new surfaces, from the perspective of fracture mechanics. And this phenomenon of concentration was detected by DIC method, see Figure 2.5. According to the legend of the contour map, red color stands for maximum strain value while purple is the minimum, in this case, given the value of 0. Two bands in red can be seen on the deformed images on each side of the crack, followed by a gradually changed color path from yellow to blue. While the deformation over rest area of the specimen appears to be extremely small that cannot be detected

effectively. Another phenomenon observed from these images is the initiation of cracks always start from one side of the specimen and propagates across the specimen all the way to the other end, with a small angle with the transvers direction. The location where crack starts initiating and propagating could be a "weak point" or "weak section" of the specimen where the internal or external flaws that are obvious might exist. For example, a big pore on the specimen tested under 100s-1 can be seen by eyes, which leads to the formation of a macro crack and failure of this sample, see Figure 2.5c. The difficulty in perfectly aligning specimen with testing machine could be another reason causing the crack initiation, which is attributed to the moment generated between the two ends. On the other hand, from the perspective of Hooke's Law, the strain distribution is directly related to stress distribution, with two material properties elastic modulus E and Poisson's ratio ν. However, it is difficult to generate the stress field from perspective of quantification, due to several reasons including the non-homogeneity of material, changing in material properties with formation of cracks, etc., which make it very complicated to determine the local E and ν. Even so, the overall strain field was clearly observed and from which the stress distribution can be roughly represented.

2.3.2.2 Shear lag based fiber/matrix bonding mechanism

The strain field obtained from DIC can be explained by the interfacial bonding mechanism between fiber and matrix. A fabric pullout model was developed based on earlier work by Naaman [41,42] with changes to account for the boundary effects, and then modified by Sueki et al. [43], to simulate the pullout

behavior for cement composites reinforced by four types of fabrics including alkali-resistant glass, polypropylene, polyethylene and polyvinyl alcohol. The model had demonstrated the ability to fit various representative curves of different fabrics, matrices, embedded length, and processing methods. A modified shear lag approach is used to simulate the response of a fabric pullout from the matrix. The criterion for growth of the debonded fiber/matrix interface is expressed in terms of the interfacial stress, and three conditions of debonding, failure, and frictional pullout are modeled as a stress based approach. Static equilibrium requires that, along the embedded length of yarn in matrix, the tensile forces in the yarn (F) be transferred to the matrix (M) through the interface and reacted against the restraint plate by normal compressive matrix stresses. This relationship expressed in the differential form is:

$$\frac{dF}{dx} = -\frac{dM}{dx} = \psi\tau \tag{1}$$

where ψ is the equivalent circumference of the yarn and τ is the shear stress at yarn-matrix interface. For small loads, the local shear stress behaves linear elastic as a function of slip with slope κ defined from the shear strength diagram (the inset in Figure 2.6) and the slip *S* defined by the difference of the elongation of the yarn δ_y and shortening of the matrix δ_m:

$$\tau = \kappa S = \kappa\left(\delta_y - \delta_m\right) = \kappa\int_0^x \left[\varepsilon_y(x) - \varepsilon_m(x)\right]dx \tag{2}$$

where $\varepsilon_y = \frac{F}{A_y E_y}$, $\varepsilon_m = -\frac{F}{A_m E_m}$, A is cross section area, E is Young modulus and subscripts *'y'* and *'m'* refer to yarn and matrix respectively. Substituting (2) in (1) and take the derivative with respect to x yields the differential equation for the yarn pullout force:

$$\frac{d^2F}{dx^2} - \beta^2 F = 0 \tag{3}$$

where $\beta^2 = \psi\kappa Q$ and $Q = \frac{1}{A_y E_y} + \frac{1}{A_m E_m}$. The general solution of the second differential equation has the following form.

$$F(x) = C_1 e^{\beta x} + C_2 e^{-\beta x} \tag{4}$$

The axial force distribution is obtained by applying the force boundary conditions $F(0) = 0$ and $F(L) = P$ in (4) and by taking a derivative with respect to x, shear stress distribution is obtained.

$$F(x) = P\frac{\sinh(\beta x)}{\sinh(\beta L)} \tag{5}$$

$$\tau(x) = \frac{P\beta}{\psi}\frac{\cosh(\beta x)}{\sinh(\beta L)} \tag{6}$$

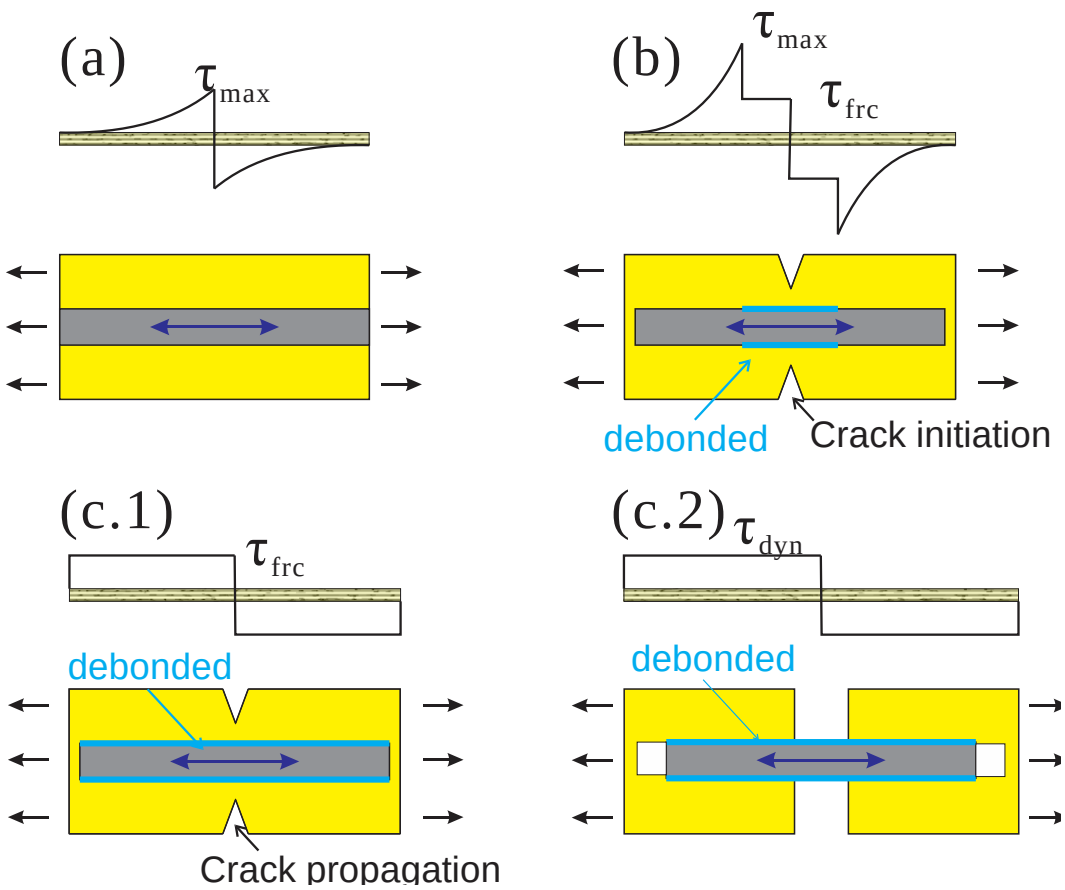

Figure 2.6 Shear Stress Distribution along the Yarn: Shear Stress and Force Distribution along the Yarn: (a) Stage I (Elastic Response); (b) Stage II (Nonlinear Response); (c) Stage III (Dynamic Response); (c.1) The first dynamic responses (no sliding, Δ_d =0); (c.2) Subsequent dynamic responses (when sliding occurs, Δ_d>0).

Elastic Stage (I):

As long as the shear stress at interface is less than the maximum shear strength τ_{max}, yarn and matrix are fully bonded as shown by dashed line in Figure 2.6a and the applied load is less than the maximum bonded load ($P_1 < P_{1b,max}$). When the shear stress at some location (where crack is about to initiate) reaches the maximum strength τ_{max}, the elastic reponse is terminated.

Nonlinear Stage (II)

Loading beyond the elastic limit is initiated when the shear stress exceeds the maximum shear strength $\tau_{max.}$ This leads to debonding for a length of *d* on the right of Figure 2.6b while the two materials are still perfectly bonded on the left portion *(L-d)*. The shear stress distribution is governed by a constant frictional stress τ_{frc} along the debonded zone in addition to a shear lag model terminating with the maximum bond strength value τ_{max} at the debonding junction.

Dynamic Stage (III)

Stage III is defined as dynamic response (Figure 2.6c), which consists of two sub stages: initial and rigid body motion. It is assumed that at the time the yarn is completely debonded $(\Delta_d = 0)$, the shear resistance still remains a uniform value τ_{frc} throughout the yarn length. Sliding $(\Delta_d > 0)$ begins right after the completion of debonding. The resisting shear stress is assumed to drop to dynamic shear strength τ_{dyn} leading to a simplified rigid body motion. It can be shown that during the rigid body motion stage ($\Delta_d > 0$), the shear resistance drops to τ_{dyn}, the embedded length reduces to $(L-\Delta_d)$.

The fabric pullout model based on shear lag theory confirmed well with the development of the strain field as shown in Figure 2.5. Generally for each set of time lapsed images, the first one or two frame is corresponding to the Elastic Stage (I). Shear stress reached its maximum τ_{max} in the zone of strain concentration where a macro crack formed, followed by the debonding between fiber and matrix. Nonlinear Stage (II) was observed as the color within this zone turned into green or orange (second or third frame), when the crack initiated. At the same time, a

gradient of strain, represented by the changing in color from orange/yellow to blue, was detected, which is traced back to the shear lag effect. The decreasing in shear stresss from crack to far field leads to a decrease in axial deformation of matrix along the same direction. The third or third and fourth frame of each image set is associated with the crack propagation and the sliding of yarn from matrix occurred, which took place during Dynamic Stage (III).

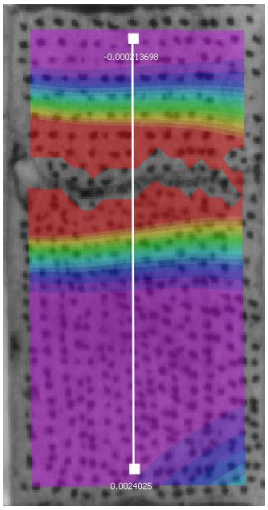

Figure 2.7 Selected line across the entire specimen for study of strain distribution

To digitize the distribution of strain, a line across the entire specimen tested under different strain rate was selected (see Figure 2.7) and the strain value at each point out of the line was extracted and plotted, as shown in Figure 2.8. The curves show a similar trend with the distribution of shear stress between fiber and matrix based on the fabric pull out model. When the shear stress between fiber and matrix exceeded shear strength τ_{max}, the peaks corresponding to strain concentration were observed (at 0.1 ms). As load kept increasing, peak value rose dramatically up to about 6% (25 s^{-1}), 9% (50 s^{-1}), and 7% (100 s^{-1}) while the failure occurred, respectively. On the contrary, uniform regions where the strain values were close

to zero can be seen, which are the regions in purple of time lapsed images (see Figure 2.5).

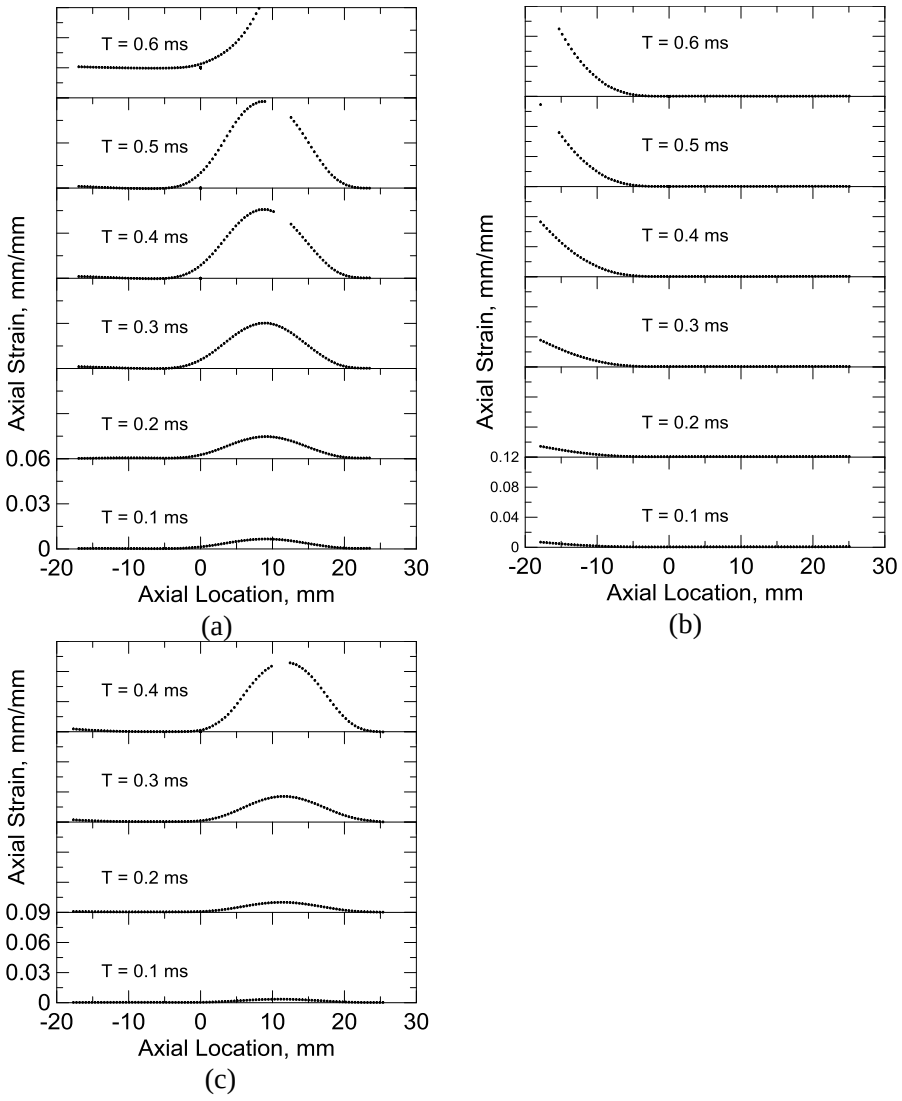

Figure 2.8 Distribution of longitudinal strain over the length of specimen tested at (a) 25 s^{-1}, (b) 50 s^{-1}, and (c) 100 s^{-1}

The fiber and matrix were perfectly bonded within this region and the shear stress is very small. As a transition from concentration to uniform, the strain decreased from peak towards both two directions of the top and bottom ends. This

gradient not only confirms with the gradually changing in color of strain field images, but also demonstrates the effect of shear lag perfectly. The discontinuous part of the curves can be traced back to the formation of crack which broke the speck pattern into segments.

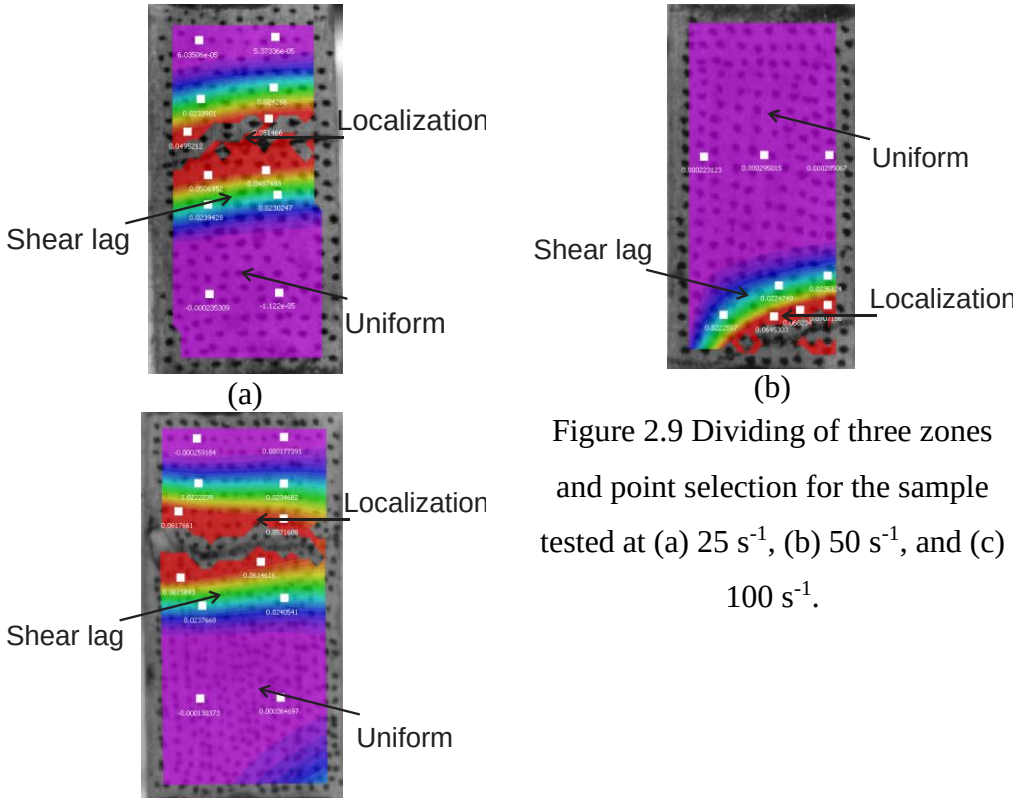

Figure 2.9 Dividing of three zones and point selection for the sample tested at (a) 25 s^{-1}, (b) 50 s^{-1}, and (c) 100 s^{-1}.

Based on the pullout model and observations from DIC, three zones were defined as Localization, Shear lag and Uniform as Figure 2.9 shows. To investigate the strain versus time histories within different zones, 9 or 12 locations for each specimen were selected shown as the small white points. Strain versus time responses at these points of interest zone were extracted and plotted, see Figure 2.10 and summarized in Table 2-3, value in parenthesis refers to standard deviation. The difference of axial strain among different zones can be easily observed. For

example, Figure 2.10a shows the 12 strain-time curves for the specimen tested at $25s^{-1}$. The axial strain in zone of localization reached 5.5% as its peak value, while within the zone of shear lag, peak strain was found to be 2.3%, less than half of that in localized strain. The curve of strain within uniform zone is subjected to very slight oscillations around 0 with maximum value of 0.6%, which is not obvious in the coordinate system with ordinate ranging from 1% to 8%. Similar trends can be found on the sample tested under $50s^{-1}$ and $100s^{-1}$.

For the overall strain versus time responses, three distinct stages are identified using Arabic numerals, with two stages prior to and one after peak. Stage 1 corresponds to a comprehensive process including the acceleration, some level of slippage existing in the gripping system to strengthen the frictional connection between specimen and fixture. More importantly, this stage may also be associated with the Elastic Stage as defined in the fabric pullout model from perspective of fiber and matrix bonding mechanism. That is, the shear stress is increasing up to the maximum shear strength τ_{max} during this time, when the fiber and matrix are perfectly bonded. When it turns into stage 2, a steeply inclined and linear portion can be observed, and the axial strain quickly rose from 1% to peaks (5% to 7%) in 0.1 to 0.4 ms, as the curves identified. This stage can be related to the Nonlinear and Dynamic stages, when the fiber and matrix were completed debonded followed by a rapid slippage or simplified rigid body motion as modeled, with shear stress dropping to a dynamic shear strength τ_{dyn}. This explanation is also supported by the study of Mechtcherine et al. [40], who pointed out the mode of failure for SHCC reinforced by PVA fiber subjected to tensile loads at strain rates above $1s^{-1}$ is

characterized by fiber-matrix pullout failure. As a result of debonding and fiber pullout, the concentration of strain was initiated and well developed, confirming with time elapsing images, see Figure 2.5. Stage 2 is terminated by the failure of the specimen, when strain reaches the peak. Thus, the slope in stage 1 is generally much smaller than that of stage 2. With the fracture of matrix and the rupture or completely pullout of fibers, a recovery of deformation in matrix was observed in stage 3, where the axial strain drops dramatically back to 0, sometimes followed by vibrations. This is attributed to the closing of invisible micro cracks bridging by fibers and elastic recovery of matrix itself. On the other hand, the whole strain response can also be divided as “pre-crack”, “crack” and “post-crack” behavior according to the effect on strain by the formation of crack. However, compared to the DIC, the post-crack behavior cannot be detected by traditional data analysis approach, where the nominal strain is defined as the displacement of actuator divided by the gage length of specimen. The traditional approach is based on two assumptions: (1) Elongation of the sample is equal to the movement of actuator; (2) strain distribution is uniform over the entire specimen. However, in fact, the existing of slippage in the gripping system makes the displacement in a way larger than the real elongation; and the actuator travels all the way down to a designated end level since the experiment was conducted using a servo-hydraulic machine under open loop. Thus the nominal strain will always increase with the moving actuator so that the recovery of deformation cannot be observed. Moreover, on the contrary with assumption (2), the distribution of strain is quite non-uniform with

concentration near the crack and uniform zone at far field as identified by the time elapsed images.

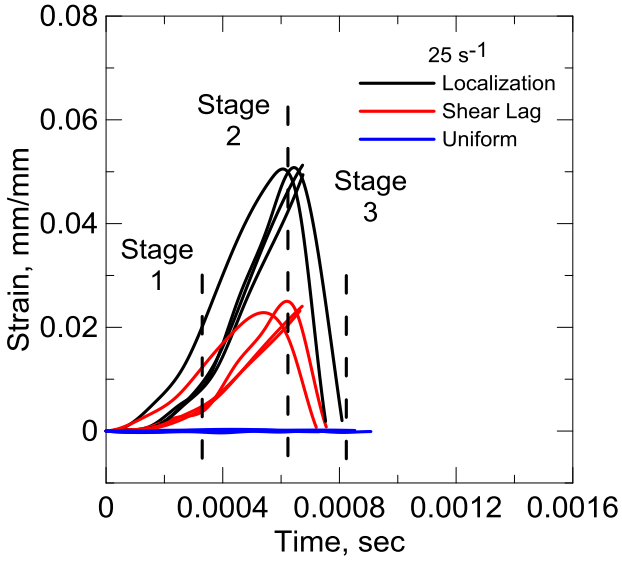

(a)

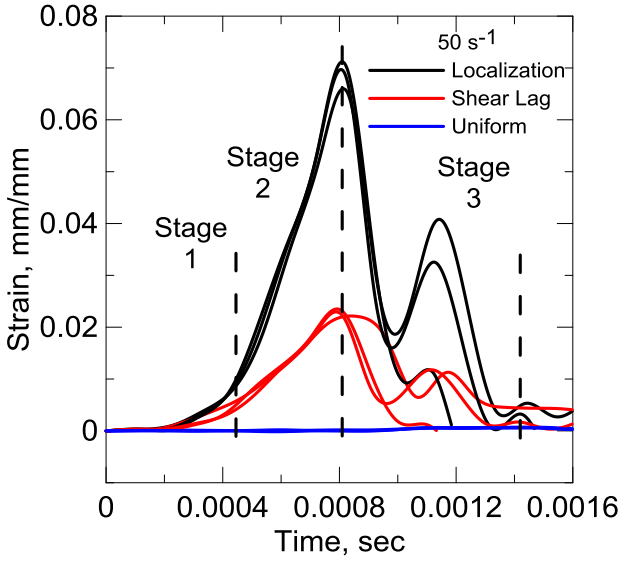

(b)

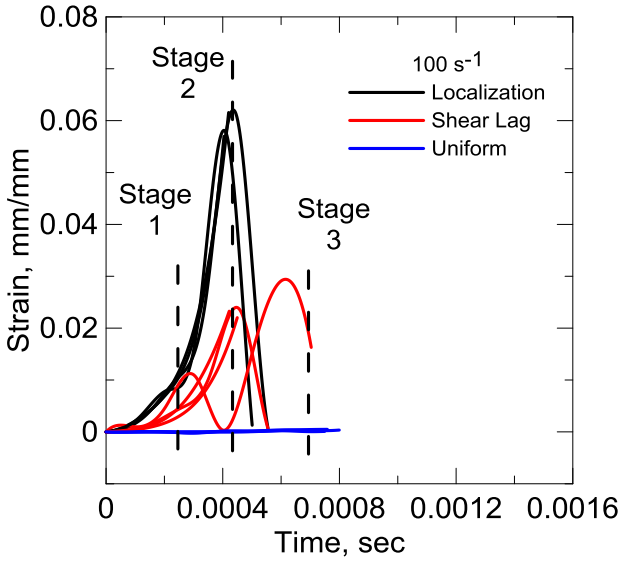

(c)

Figure 2.10 Strain versus time histories obtained from DIC method selected from three defined regions for the sample tested at different strain rates: (a) $25s^{-1}$, (b) $50s^{-1}$, and (c) $100s^{-1}$.

Table 2-3 Summary of peak strains within different zones; average results (standard deviations are given in parentheses).

Peak Strain (%)	25 s^{-1}	50 s^{-1}	100 s^{-1}
Localization	5.5078 (0.0887)	6.9030 (0.2819)	5.9705 (0.2162)
Shear lag	2.3117 (0.0748)	2.3000 (0.0654)	2.3130 (0.0794)
Uniform	0.0588 (0.0254)	0.0644 (0.0069)	0.0557 (0.0278)

2.3.2.3 Stress-strain

The correlation between stress responses and strain responses obtained from DIC was also done for four individual speckled samples tested at different strain rate, as shown in Figure 2.11 and summarized in Table 2-4. Due to the non-uniform distribution of strain, the average value of strain along the selected lines (see Figure

2.9) was calculated and plotted with the stress. Since the images (source of strains) and loads (source of stress) were collected using two different systems, high speed camera and data acquisition system connected to testing machine, time was used to link the two sets of signals as the sampling rate of each system is known. Figure 2.11a shows the DIC based stress-strain curves of the four speckled samples and Figure 2.11b compares the stress-strain responses obtained from DIC with the original ones. It can be seen both from the plots and table that the initial slope of the four original curves, 1.15 GPa, 1.27 GPa, 7.70 GPa and 0.67 GPa, are quite low and showing large variation. While the initial linear portion is associated with the pre-crack stage of the test, when the fibre and matrix are perfectly bonded. During this stage, the tensile load is mostly taken by the matrix rather than the fibre. Thus the initial slope should be close to the elastic modulus of matrix. However, at the very beginning of test, slippage in the gripping system, demonstrated by the high speed video, takes place which leads to the error in measurement of deformation. In addition, testing condition like the frictional gripping force for each specimen differs from one to another, resulting in different amount of slippage. This effect of slippage enlarges the measured deformation in varying degrees thereby the low and varying initial slopes were observed. Nevertheless, strain measurement using DIC method can resolve this issue as it directly addresses the changing from reference and deformed images, which exclude the effect of gripping system. The initial slope were corrected to 29.40 GPa, 32.80 GPa, 29.80 GPa and 29.72 GPa, respectively as shown in Table 2-4, which are much closer to the general elastic modulus of concrete which ranges from 23 to 26 GPa. The variation was decreased as well that

can be easily observed in Figure 2.11a, initial linear portions following the same path on top of each other. Another apparent difference detected is the evident decrease in strain at peak, which can be traced back to the slippage between fibre and matrix. The slippage is an internal displacement that cannot be tracked by DIC, as it is addressing the deformation on the surface. While the total elongation measured by means of acquiring the displacement of stroke is able to record this internal slippage. In that both the traditional and DIC methods should be employed for a better understanding of the mechanical behaviour of SHCC specimens under dynamic tensile testing.

Table 2-4 Summary of strains at peak and initial slope of stress-strain curves

Specimen ID	Strain Rate (s^{-1})	Strain at Peak (%)		Stiffness (Gpa)	
		Original	DIC	Original	DIC
m68_w33_2	25	0.92	0.07	1.15	29.40
m68_w33_3	25	0.87	0.11	1.27	32.80
m68_w32_3	50	0.70	0.27	7.70	29.80
m68_w34_9	100	2.25	0.10	0.67	29.72

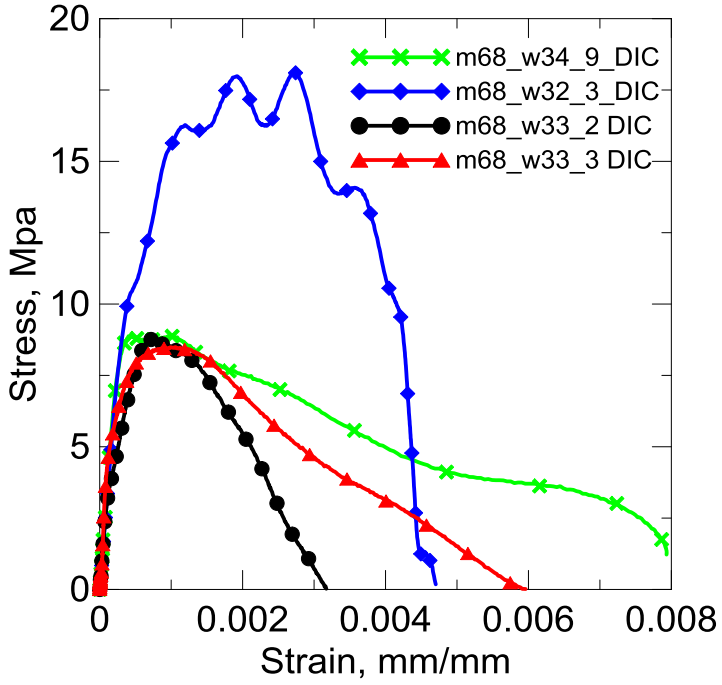

(a)

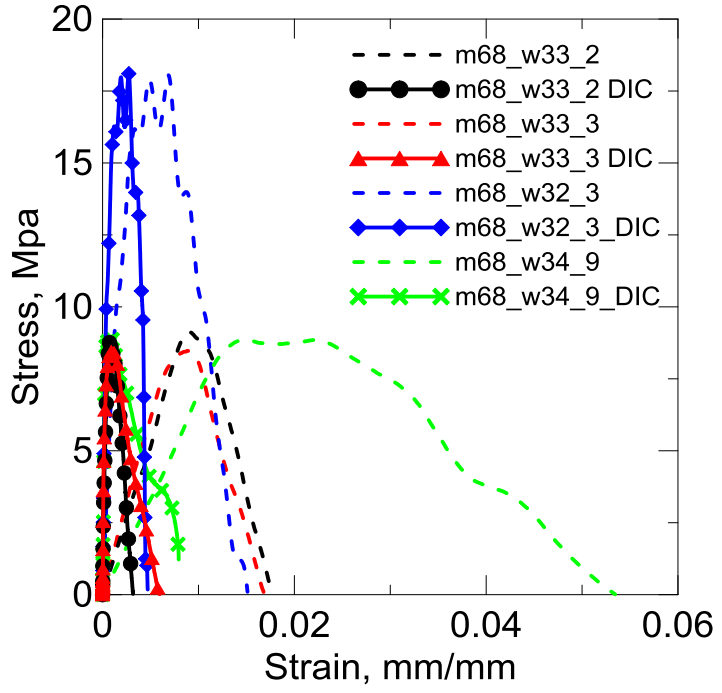

(b)

Figure 2.11 (a) Stress-strain responses based on DIC method and (b) comparison between original and DIC analysis results.

2.4 Conclusions

The following conclusions can be drawn from the present work on the behaviour of SHCC under high tensile strain rate loading:

- For tensile tests performed at rates $25s^{-1}$, $50s^{-1}$, and $100s^{-1}$ in this study, SHCC showed an increase in tensile strength, strain capacity and work-to-fracture with increasing loading rate. No pronounced multiple cracking was observed. And the failure of the composite was accompanied by the pullout of most of the fibres crossing the macro-crack. The increase in tensile strength is attributed to the considerable increase in bond strength between PVA fibre and matrix and the moderate increase in fiber strength at high strain rates. The observation of increase in the strain capacity of SHCC at high strain rates can be explained by the increase in fibre pullout length and the plastic deformation of the fibres.
- DIC was a powerful tool to determine the non-uniform full-field strain field and pre-crack, crack, and post-crack behaviour for cement composites that cannot be obtained using the traditional deformation measurement and data processing approach. Three zones were observed and defined as localization, shear lag and uniform based on the strain fields. These observations are well associated with the fabric pullout model proposed by Sueki et al. [43], which explained the development of strain field obtained by DIC from perspective of fiber/matrix bonding mechanism. DIC method also successfully corrected the elastic modulus to a reasonable range as identified by the stress-strain responses based on DIC. However, due to the

basic theory, DIC method cannot detect the internal slippage between fiber and matrix, as it addresses the surface deformation. Thus, for the cement composite materials, the combination of traditional processing and DIC approach gives rise to a better and more comprehensive understanding of the mechanical behaviour.

3. EFFECT OF TEMPERATURE ON THE HIGH STRAIN TENSILE RESPONSE OF TEXTILE-REINFORCED CEMENT COMPOSITES

3.1 Introduction

Cement-based materials may be subjected to dynamic loading due to explosions, projectiles, earthquakes, wind gusts, or moving objects. Due to the inherent brittleness and low tensile strength of most cement-based elements, dynamic loading can cause severe cracking and damage [44, 45]. In order to properly analyze and design structures that are subjected to dynamic loading, it is necessary to utilize the mechanical properties associated with the strain rates the structural components are subjected to.

Characterization of dynamic tensile properties of materials is challenging as the failure process is affected by the mode and method of testing. Problems may appear at high-rate loading due to inertial effect, non-uniform loading, and difficulties in measuring reliable mechanical characteristics of the materials. There is a lack of general agreement about the standards and methodology used to conduct dynamic tensile tests [46]. This creates a challenge as correlation of the dynamic properties with published literature depends on several factors including the loading rate, method of testing, and the geometry of the tested element [47, 48, 49]. A number of experimental techniques exist to investigate high-strain rate material properties: split Hopkinson pressure bar (SHPB), falling weight devices, flywheel facilities and hydraulic machine [50, 51, 52, 53]. The use of servo-hydraulic machines in medium-strain rate for tensile testing has been reported for steel [54,55], plastics [46,56] and composite materials [57], however, test results for

cement-based composites are limited. The importance of specimen geometry and size in dynamic material testing has been recognized by the Society of Automotive Engineers (SAE) which coordinated the standardization of "High Strain Rate Tensile Test Techniques for Automotive Plastics" in order to develop guidelines for dynamic tensile testing at medium strain rates [58, 59]. The International Iron and Steel Institute (IISI) also formed a consortium to develop a high strain rate tensile test standard for sheet steel [60], while European researchers have been working on an ISO standard [61].

Textile reinforcement for cement-based materials has become popular as an effective way of enhancing the tensile capacity and energy absorption of the brittle material [62, 63]. Textile-reinforced composites demonstrate a significant improvement in the energy absorption capacity under static loading as compared to plain concrete materials and other fibrous cement composites [64, 65, 66]. Recent work on impact behavior, has shown the potential of such components under high speed loading [67, 68, 69]. Research on dynamic tensile strength under high-strain rates of fibers and fabrics such as Aramid, Twaron, and Zylon has been reported by several authors [70, 71, 72, 73, 74]. Strain-rate effects on the mechanical properties of the Kevlar® 49 fibers was studied by Xia and Wang [73] who addressed rate dependence of Young's modulus, failure stress, and failure strain over a strain rate range of 10-4 s-1 to 1350 s-1 [75]. Differences in the behavior of fabrics under high speed loading directly affect the behavior of composites made with the fabrics.

This paper presents the results of high-speed tensile testing for laminated cement composites reinforced with various types of textiles. Three types of textiles were used: laminated Alkali Resistant (AR) glass, warp-knitted Alkali Resistant (AR) glass, and warp-knitted polypropylene. The two warp-knitted textiles produced by Institut für Textiltechnik (ITA). The cement-based composites reinforced with these textiles were made and also tested to obtain the dynamic material properties, including tensile strength, toughness, and maximum strain. Mechanical response of textiles and composites were obtained at temperatures of -30 °C, 25 °C, and 80 °C.

3.2 High Speed Tensile Test Methodology

3.2.1 Dynamic Tensile Test Procedure

The high-speed tensile tests were performed in a high-rate MTS testing machine. The setup and procedure of the dynamic tensile testing were addressed in Chapter 1[1.1]. The tension tests were performed at strain rate of $100s^{-1}$. An environmental chamber (see figure 3.1) was used for controlling the temperature for each test. The chamber uses heating elements for elevated and liquid nitrogen for low temperatures. The temperature data were recorded using a recording signal conditioner. Once the desired temperature was reached, the specimen was conditioned for 5 minutes before the high-speed test.

Material parameters derived from the experimental data included tensile strength (peak stress), strain capacity (strain on reaching tensile strength) and work to fracture. Work to fracture was calculated using the total area under the stress-

strain curve. Average value and standard deviation are given for each strain rate. Furthermore, tensile stress-strain curves of the specimens tested under static and dynamic conditions are compared.

Figure 3.1 High speed testing machine with environmental chamber at Arizona State University

3.2.2 Data Processing

The approach of data processing for dynamic response was discussed in Chapter 1 [1.1.8].

3.2.3 Image analysis – digital image correlation (DIC) method

High speed videos were taken using a phantom camera, to be analyzed using DIC method. The setup of high speed camera, testing procedure, and discipline of DIC method were discussed in the first chapter [1.2].

3.3 Experimental Program

3.3.1 Textiles

Three types of textiles were used in this study: 1) laminated alkali-resistant (AR) glass referred to as AR in this paper, 2) warp-knitted AR-glass referred to as GL in this paper, and 3) warp-knitted polypropylene-glass hybrid referred to as PP in this paper. Sample pictures are shown in Figure 3.2. It is noted that for the warp-knitted textiles, weft is in the horizontal direction and warp is in the vertical direction. The GL and PP textiles have identical geometries and Table 3-1 includes the properties and dimensions for the various textiles used in this study. The knitted textiles were made with glass and polypropylene yarns, produced using a commingling setup at Institut für Textiltechnik der RWTH Aachen. More details about the textile production can be found elsewhere [76].

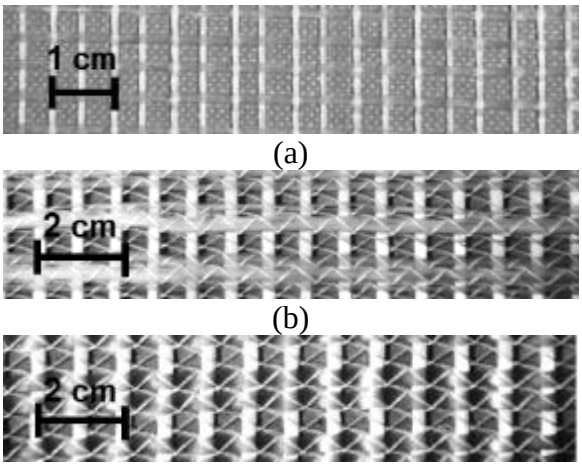

Figure 3.2 Close up pictures of a) AR-glass textile (laminated), b) AR-glass textile (warp-knitted), and c) polypropylene textile (warp-knitted). Note: weft: horizontal and warp: vertical.

Table 3-1 Geometrical characteristics of textiles

Material	Weft (90 deg)	Warp (0 deg)	Knitting Yarn	Yarn Count (Weft or Warp)	Density
				[tex]	[g/cm^3]
AR-Glass (AR)	AR-Glass	AR-Glass	Laminated	---	---
AR-Glass (GL)	AR-Glass	AR-Glass	PES (167 tex)	1200	2.68
Polypropylene (PP)	AR-Glass	PP	PES (167 tex)	400	0.9

3.3.2 Composite Materials

Textile-reinforced cement composites were prepared with 4 layers of textiles using the pultrusion process as shown in Figure 3.4. The mixture proportions used for the cement paste are presented in Table 3-1. The textile passes through a slurry infiltration chamber to get coated, and then pulled through a set of rollers to squeeze the paste in between the fabric openings while removing excessive paste. The textile cement composites were then formed on a plate shaped mandrel resulting in layered sheets with 250 × 300 mm. After forming the samples, constant pressure was applied on the surface of the composite sheets to improve penetration of the matrix in between the yarn and fabric openings.

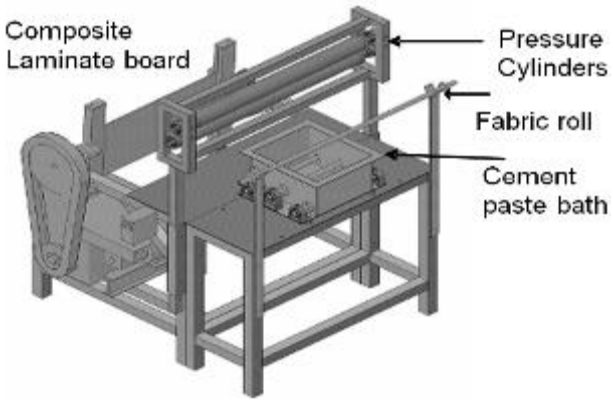

(a)

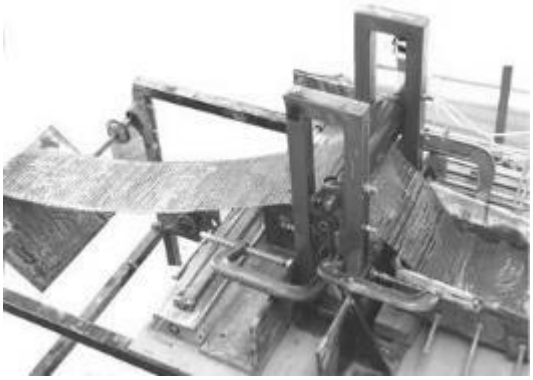

(b)

Figure 3.3 Pultrusion process for making TRC: a) schematics and b) actual system

Table 3-2 Mixture proportions for the cementitious matrix

Cement [gr.]	Fly Ash [% of Cement]	Water/CM	Water [ml]	Superplasticizer [% of CM]	Superplasticizer [ml]
800	160	0.3	290	0.25	2.5

Panels were demolded after 12 hours and cured under water at room temperature for 28 days. Specimens of 25 mm wide and 150 mm long were prepared. A typical composite is shown in Figure 3.4. The average thickness of the composites was 11 mm. Three replicate specimens were used for each composite type. Additionally, plain textile samples with dimensions of 25 mm in width and 150 mm in length were cut and used for high-speed testing. Aluminum plates were glued onto the gripping edges of the specimen to minimize localized damage and

provide load transfer to the grips during the high speed tensile test. The gauge length of all specimens was 50 mm. Typical textiles samples are shown in Figure 3.5.

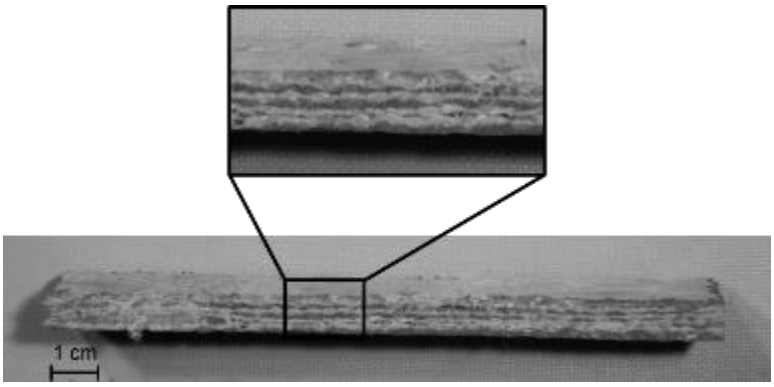

Figure 3.4 Typical textile reinforced cement composite sample with 4 payers of textiles

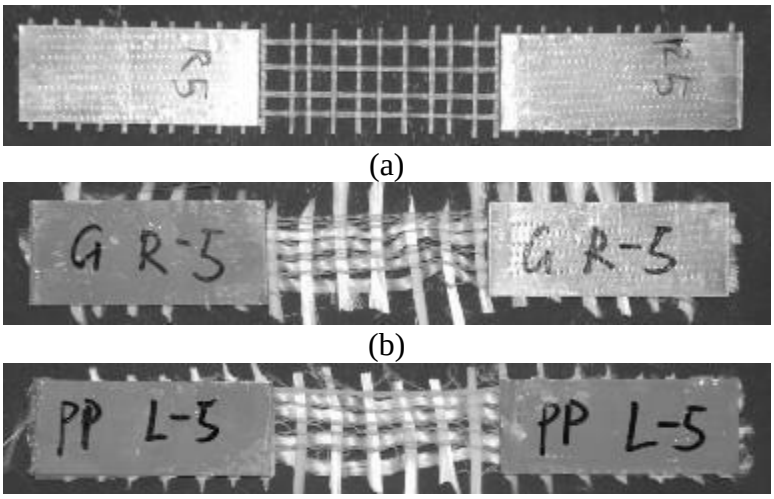

Figure 3.5 Typical textile samples prepared for testing: a) laminated AR-glass textile, b) knitted AR-glass textile, and c) knitted polypropylene textile

3.4 Results and Discussion

High-strain tensile tests were performed on the prepared textile and TRC specimens under three different temperatures: -30 ○C, +25 ○C, and +80 ○C. state

the conditioning duration. The test results for laminated AR-glass textile and TRC are shown in Figure 3.6. The force applied to individually-tested textiles was scaled by 4 for comparison purposes. A V.7 Phantom high-speed camera was used for capturing high-speed videos during the test (under room temperature only). These images are shown in Figure 3.7 for laminated AR-glass textiles with time difference (Δt) between images of about 10-4 sec. Figure 3.8 shows the time-lapse images for AR composites with time difference (Δt) of about 3x10-4 sec. Multiple cracking and textile pull-out mechanism can be observed for this type of composite. Table 3-3 and Table 3-4 summarize the experimental parameters calculated for each test. These include the force and strain at the first peak (the end of linear region), maximum force, maximum strain, toughness at peak and maximum toughness. The stress values for composites were calculated based on their cross-sectional dimensions; however stress calculation is not applicable for textile samples. In most cases, the maximum force is observed at the peak point, however, in some cases for composites the maximum force is obtained after the linear region in the strain hardening or strain softening regions.

The maximum load for AR textiles tested under room temperature was 3367±704 N. These values were 3044±828 N and 2561±425 N under low and high temperatures, respectively. The nominal cross-section of one roving of knitted textiles has approximately 0.445 mm2 area and since four roving were used in each sample, the nominal cross-sectional area is approximately 1.78 mm2. This value is used for calculating the nominal maximum stress values for textile samples. The average maximum strain values for all temperatures was in the range of 0.04 and

0.052 mm/mm and the average maximum toughness was in the range of 2.6 and 4.2 N.mm. The maximum force almost doubled in AR composites (up to 5995 N). Much lower standard deviation in the composites implying an enhanced bond between textile and cement matrix as compared to other systems. The maximum toughness values for AR composites was in the range of 12.7 and 27.3 N.mm which is approximately 6 times higher than textiles. The effect of temperature was not significant for AR textiles or AR composites.

The test results for knitted AR-glass textile and TRC are shown in Figure 3.9. The high-speed images are shown in Figure 3.10 for GL textiles with Δt of about 10-4 sec and in Figure 3.11 for GL composites with time difference of about 3x10-4 sec. Multiple cracking and textile pull-out mechanism can be also observed for this type of composite. Table 3-5 and Table 3-6 summarize the experimental parameters calculated for each test. The maximum load for GL textiles tested under room temperature was 1541±215 N. These values were 2767±213 N and 2425±118 N under low and high temperatures, respectively. The average maximum strain values for all temperatures was in the range of 0.097 and 0.125 mm/mm and the average maximum toughness was in the range of 5.2 and 7.5 N.mm. The maximum force almost tripled in GL composites (up to 7615 N) due to the bond between textile and cement matrix. The maximum toughness values for AR composites was in the range of 27.6 and 32.3 N.mm which is approximately 6 times higher than textiles. The effect of temperature was not significant for GL textiles either, however, lower temperatures resulted in higher force values in GL composites.

The test results for knitted polypropylene textile and TRC are shown in Figure 3.12. The time-lapse images are shown in Figure 3.13 for PP textiles with Δt of about 10-4 sec and in Figure 3.14 for PP composites with time difference of about 3x10-4 sec. Unlike the AR-glass composites, multiple cracking and textile pull-out mechanism is non-existing for this type of composite. Table 3-7 and Table 3-8 summarize the experimental parameters calculated for each test. Typical failed composite samples are shown in Figure 3.15. The maximum load for PP textiles tested under room temperature was 2578±220 N. These values were 2360±203 N and 2350±380 N under low and high temperatures, respectively. The average maximum strain values for all temperatures was in the range of 0.110 and 0.127 mm/mm and the average maximum toughness was in the range of 7.7 and 9.3 N.mm. The maximum force remained almost the same in PP composites (up to 2856 N) due to the weak bond between textile and cement matrix. The maximum toughness values for PP composites was in the range of 10.5 and 16.8 N.mm which is approximately 1.5 times higher than textiles. The effect of temperature was not significant for PP textiles or PP composites.

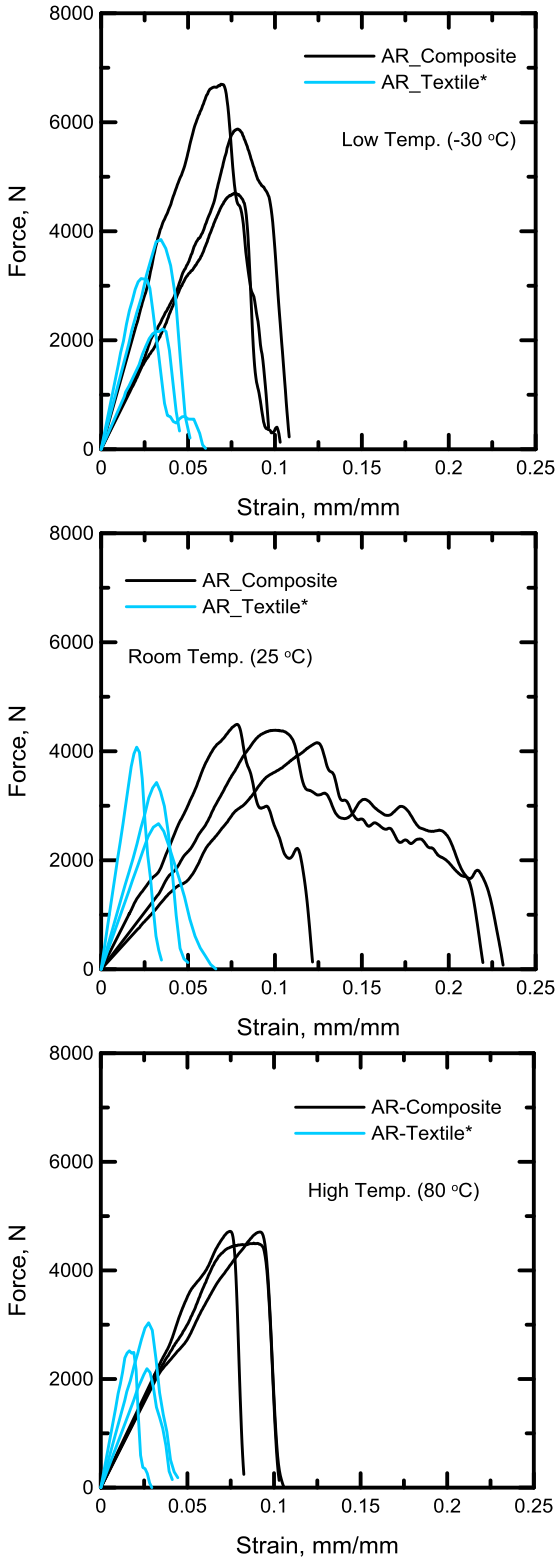

Figure 3.6 High-strain test results for laminated AR-glass textile and TRC

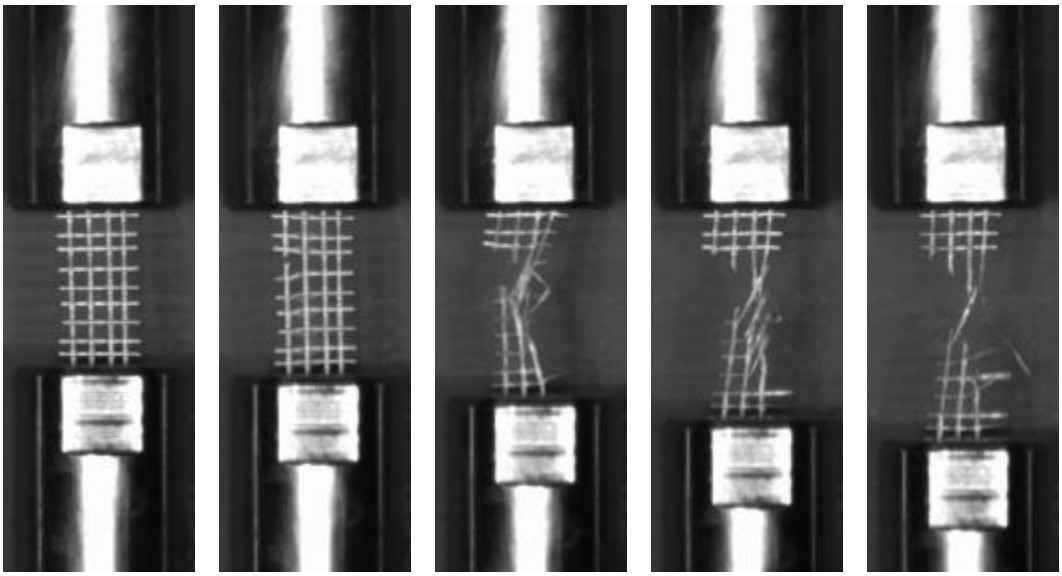

Figure 3.7 Time lapse images for laminated AR-glass textile (Δt between images ≈ 10-4 sec)

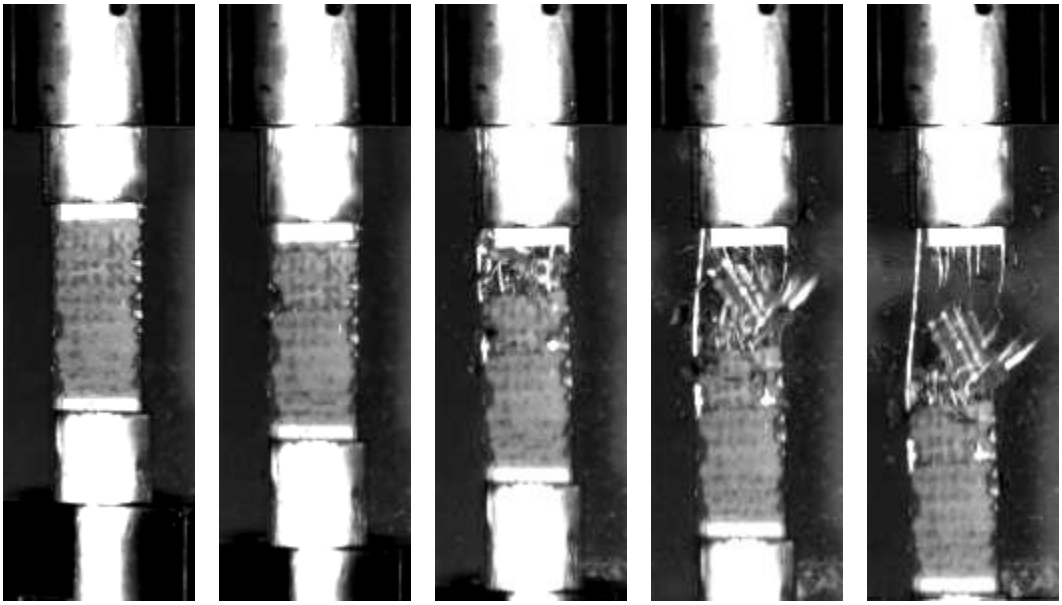

Figure 3.8 Time lapse images for laminated AR-glass TRC (Δt between images ≈ 3x10-4 sec)

Table 3-3 Experimental parameters for high-strain test for laminated AR-glass textiles

Temp.	Code	Peak Force *	Nominal Peak Stress **	Strain (at Peak)	Toughness (at Pea	Max. Force*	Nominal Max. Stress**	Max. Strain	Max. Toughness
	Units	N	MPa	mm/mm	N.m	N	MPa	mm/mm	N.m
LT	No.1	3108	437	0.025	2.3	3108	437	0.059	4.2
	No.2	2186	307	0.035	2.0	2186	307	0.046	2.9
	No.3	3838	539	0.034	3.0	3838	539	0.051	5.5
	AVG	3044	428	0.031	2.4	3044	428	0.052	4.2
	SD	828	116	0.006	0.5	828	116	0.007	1.3
RT	No.1	3413	479	0.031	2.5	3413	479	0.049	4.4
	No.2	2641	371	0.032	2.0	2641	371	0.063	4.4
	No.3	4046	568	0.019	1.9	4046	568	0.034	3.7
	AVG	3367	473	0.027	2.1	3367	473	0.049	4.2
	SD	704	99	0.007	0.3	704	99	0.015	0.4
HT	No.1	2529	355	0.018	1.3	2529	355	0.029	1.9
	No.2	2153	302	0.027	1.5	2153	302	0.042	2.4
	No.3	3002	422	0.027	1.9	3002	422	0.043	3.4
	AVG	2561	360	0.024	1.6	2561	360	0.038	2.6
	SD	425	60	0.005	0.3	425	60	0.008	0.8

* Force for 4 layers of textiles ** Nominal stress for 1 layer of textile

Table 3-4 Experimental parameters for high-strain test for laminated AR-glass TRC

Temp.	Code	Peak Force	Peak Stress	Strain (at Peak)	Toughness (at Peak)	Max. Force	Max. Stress	Max. Str	Max. Toughness
	Units	N	MPa	mm/mm	N.m	N	MPa	m	N.m
LT	No.1	4672	23.4	0.078	9.6	N/A	N/A	0.1	12.0
	No.2	6676	33.4	0.067	12.3	6076	30.4	0.0	18.3
	No.3	5914	29.6	0.079	11.0	5914	29.6	0.1	17.1
	AVG	5754	28.8	0.075	10.9	5995	30.0	0.1	15.8
	SD	1012	5.1	0.007	1.4	115	0.6	0.0	3.3
RT	No.1	4493	22.5	N/A	9.1	4493	22.5	0.1	N/A
	No.2	4340	21.7	0.100	11.3	4340	21.7	0.2	28.3
	No.3	4154	20.8	0.124	13.7	4154	20.8	0.0	26.4
	AVG	4329	21.6	0.112	11.4	4329	21.6	0.1	27.3
	SD	170	0.8	0.017	2.3	170	0.8	0.0	1.4
HT	No.1	4718	23.6	0.091	11.6	4718	23.6	0.1	13.5
	No.2	4441	22.2	0.074	8.4	4441	22.2	0.1	14.1
	No.3	4702	23.5	0.075	9.4	4702	23.5	0.0	10.6
	AVG	4620	23.1	0.080	9.8	4620	23.1	0.0	12.7
	SD	156	0.8	0.010	1.6	156	0.8	0.0	1.9

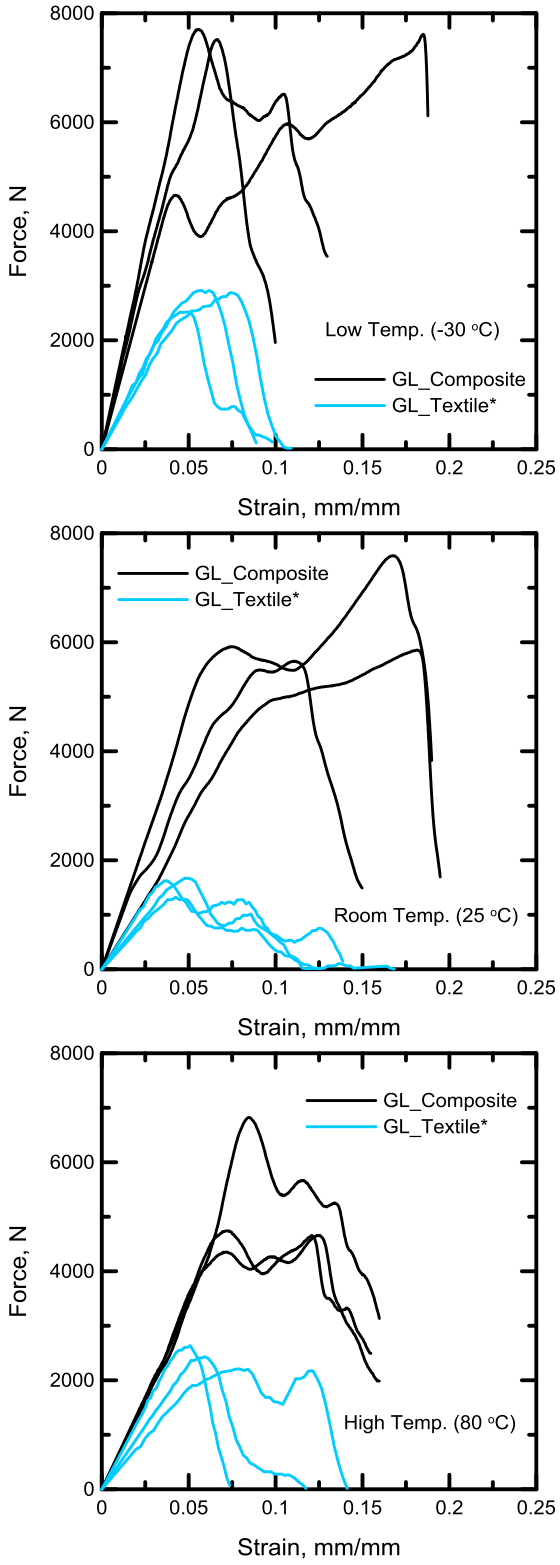

Figure 3.9 High-strain test results for knitted AR-glass textile and TRC

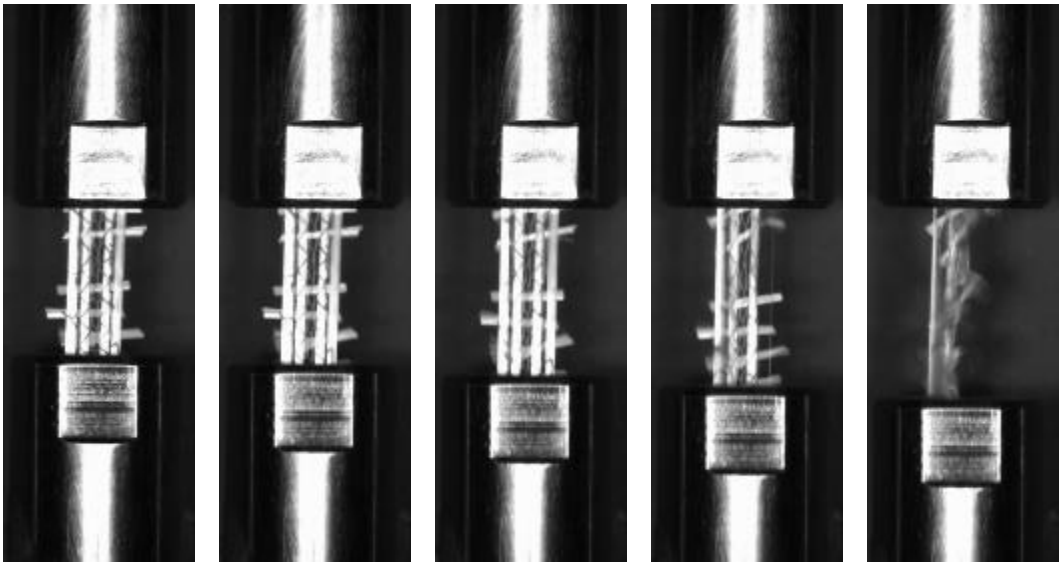

Figure 3.10 Time lapse images for knitted AR-glass textile (Δt between images ≈ 10-4 sec)

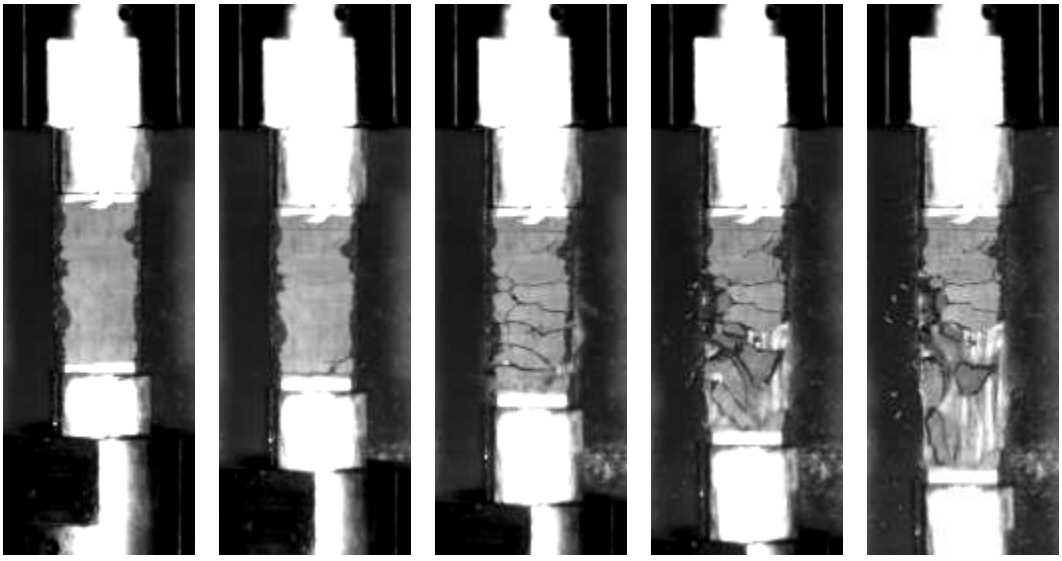

Figure 3.11 Time lapse images for knitted AR-glass TRC (Δt between images ≈ 3x10-4 sec)

Table 3-5 Experimental parameters for high-strain test for knitted AR-glass textiles

Temp.	Code	Peak Force *	Nominal Peak Stress**	Strain (at Peak)	Toughness (at Peak)	Max. Force *	Nominal Max. Stress**	Max. Strain	Max. Toughness
	Units	N	MPa	mm/m	N.m	N	MPa	mm/	N.m
LT	No.1	2524	354	0.049	3.4	2524	354	0.098	6.0
	No.2	2918	410	0.060	5.2	2918	410	0.089	7.6
	No.3	2860	402	0.076	6.9	2860	402	0.104	9.0
	AVG	2767	389	0.062	5.2	2767	389	0.097	7.5
	SD	213	30	0.014	1.7	213	30	0.008	1.5
RT	No.1	1293	182	0.043	3.0	1293	182	0.123	4.1
	No.2	1649	232	0.037	1.6	1649	232	0.139	6.4
	No.3	1680	236	0.050	2.3	1680	236	0.114	5.2
	AVG	1541	216	0.043	2.3	1541	216	0.125	5.2
	SD	215	30	0.007	0.7	215	30	0.013	1.1
HT	No.1	2230	313	0.082	5.6	2230	313	0.140	10.5
	No.2	2625	369	0.051	3.8	2625	369	0.075	5.4
	No.3	2421	340	0.059	3.8	2421	340	0.114	6.4
	AVG	2425	341	0.064	4.4	2425	341	0.110	7.4
	SD	198	28	0.016	1.1	198	28	0.033	2.7

* Force for 4 layers of textiles ** Nominal stress for 1 layer of textile

Table 3-6 Experimental parameters for high-strain test for knitted AR-glass TRC

Temperature	Code	Peak Force	Peak Stress	Strain (at Peak)	Toughness (at Peak)	Max. Force	Max. Stress	Max. Strain	Max. Toughness
	Units	N	MPa	mm/mm	N.m	N	MPa	mm/m	N.m
LT	No.1	7538	37.7	0.066	13.2	7538	37.7	0.100	21.3
	No.2	N/A	N/A	0.042	N/A	7610	38.1	0.189	N/A
	No.3	7698	38.5	0.056	11.5	7698	38.5	0.130	33.5
	AVG	7618	38.1	0.055	12.4	7615	38.1	0.140	27.4
	SD	113	0.6	0.012	1.2	80	0.4	0.045	8.6
RT	No.1	4950	24.8	0.096	12.4	5861	29.3	0.195	37.9
	No.2	5492	27.5	0.088	13.2	5661	28.3	0.146	26.7
	No.3	5892	29.5	0.068	10.8	N/A	N/A	0.190	N/A
	AVG	5445	27.2	0.084	12.1	5761	28.8	0.177	32.3
	SD	473	2.4	0.014	1.3	141	0.7	0.027	8.0
HT	No.1	4321	21.6	0.069	8.1	4642	23.2	0.160	25.4
	No.2	N/A	N/A	0.084	12.7	N/A	N/A	0.159	32.3
	No.3	4716	23.6	0.069	8.1	4716	23.6	0.157	25.2
	AVG	4519	22.6	0.074	9.6	4679	23.4	0.159	27.6
	SD	279	1.4	0.009	2.7	52	0.3	0.002	4.1

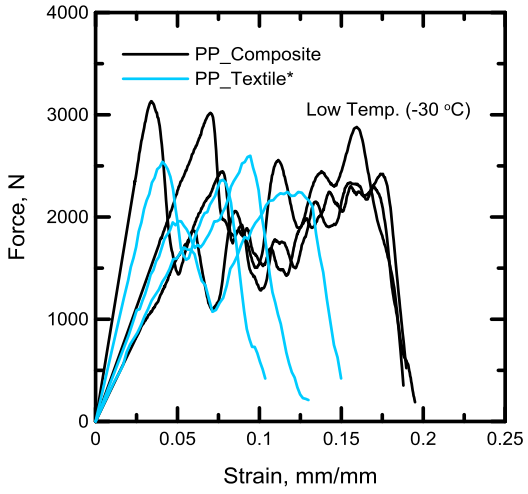

(a)

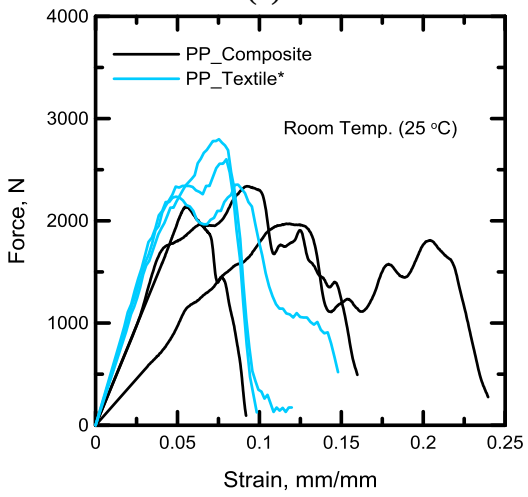

(b)

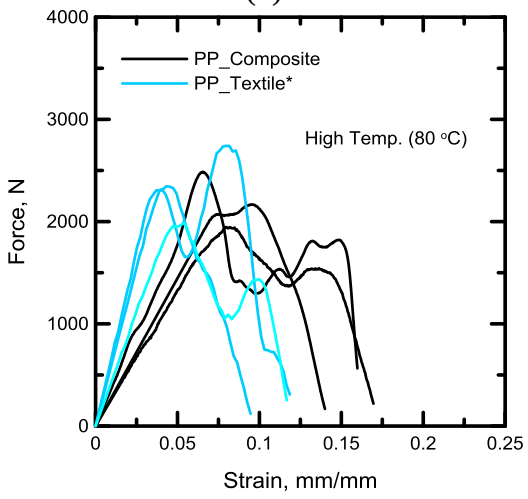

(c)

Figure 3.12 High-strain test results for knitted PP textile and TRC

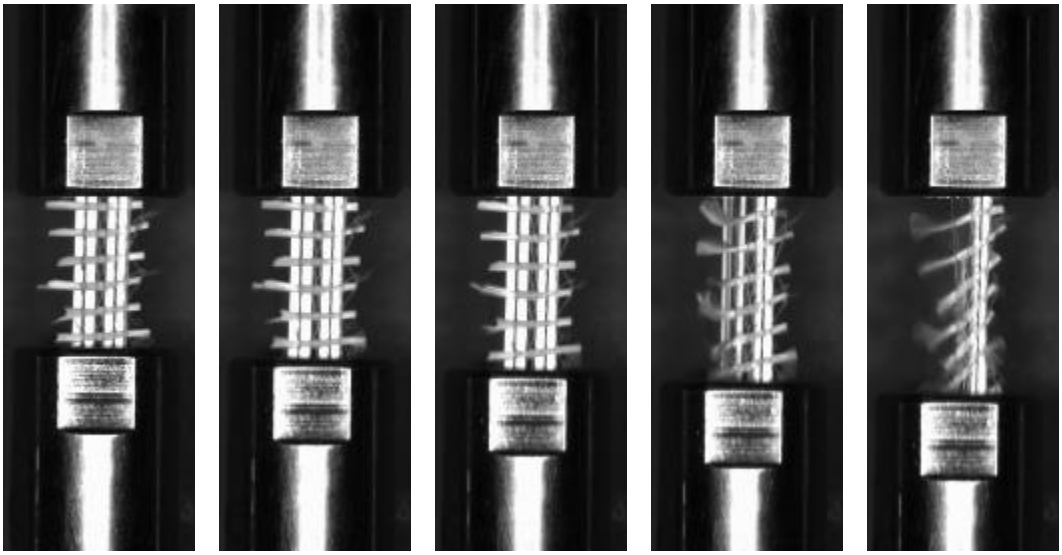

Figure 3.13 Time lapse images for knitted PP textile (Δt between images ≈ 10-4 sec)

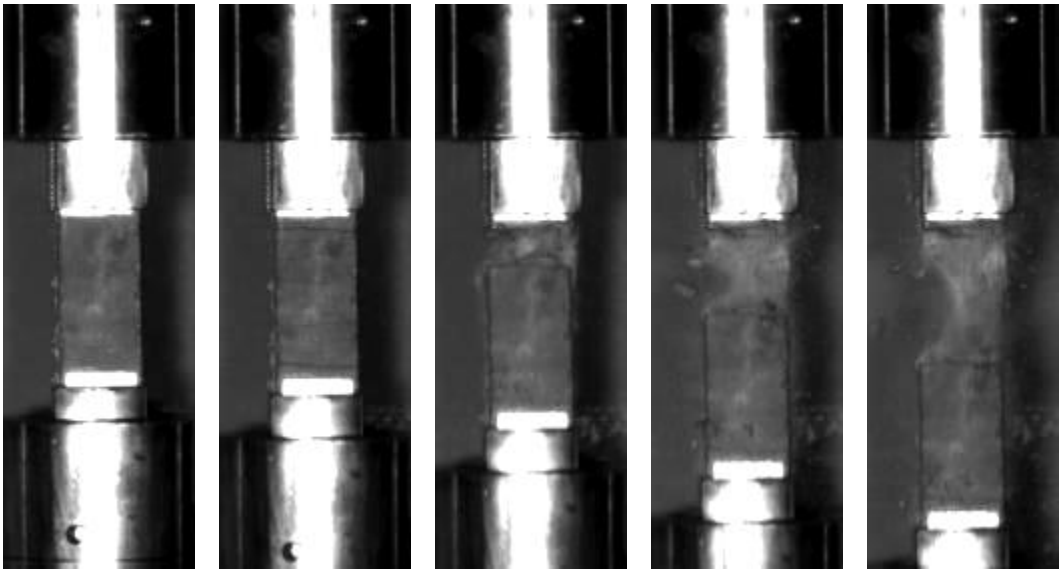

Figure 3.14 Time lapse images for knitted PP TRC (Δt between images ≈ 3x10-4 sec)

Table 3-7 Experimental parameters for high-strain test for knitted PP textiles

* Force for 4 layers of textiles ** Nominal stress for 1 layer of textile

Temp.	Code	Peak Force*	Nominal Peak Stress**	Strain (at Peak)	Toughness (at Peak)	Max. Force*	Nominal Max. Stress**	Max. Strain	Max. Toughness
	Units	N	MPa	mm/mm	N.m	N	MPa	mm/mm	N.m
LT	No.1	1691	238	0.053	2.3	2231	313	0.149	10.6
	No.2	2540	357	0.040	2.6	2254	317	0.104	8.3
	No.3	1946	273	0.048	2.3	2594	364	0.129	9.2
	AVG	2059	289	0.047	2.4	2360	331	0.127	9.3
	S.D.	436	61	0.007	0.2	203	29	0.023	1.1
RT	No.1	2324	326	0.047	2.8	2587	363	0.098	8.0
	No.2	2794	392	0.074	6.0	2794	392	0.105	8.5
	No.3	2216	311	0.045	2.7	2354	331	0.149	11.2
	AVG	2445	343	0.055	3.8	2578	362	0.117	9.3
	S.D.	307	43	0.016	1.8	220	31	0.028	1.7
HT	No.1	1967	276	0.050	2.7	1967	276	0.118	7.1
	No.2	2310	324	0.038	2.3	2727	383	0.119	9.7
	No.3	2351	330	0.043	2.6	2357	331	0.094	6.4
	AVG	2209	310	0.044	2.5	2350	330	0.110	7.7
	S.D.	211	30	0.006	0.2	380	53	0.014	1.8

Table 3-8 Experimental parameters for high-strain test for knitted PP TRC

Temp.	Code	Peak Force	Peak Stress	Strain (at Peak)	Toughness (at Peak)	Max. Force	Max. Stress	Max. Strain	Max. Toughness
	Uni	N	MPa	mm/mm	N.m	N	MPa	mm/m	N.m
LT	No.	3018	15.1	0.070	5.4	3018	15.1	0.189	16.8
	No.	3118	15.6	0.033	2.7	3118	15.6	0.187	18.3
	No.	2432	12.2	0.078	4.9	2432	12.2	0.196	15.3
	AV	2856	14.3	0.060	4.3	2856	14.3	0.191	16.8
	S.D	371	1.9	0.024	1.4	371	1.9	0.005	1.5
RT	No.	1760	8.8	0.044	2.0	2330	11.7	0.161	12.3
	No.	1976	9.9	N/A	N/A	1976	9.9	0.240	14.9
	No.	2146	10.7	0.055	2.1	2146	10.7	0.091	N/A
	AV	1961	9.8	0.050	2.0	2151	10.8	0.164	13.6
	S.D	193	1.0	0.008	0.1	177	0.9	0.075	1.9
HT	No.	2073	10.4	0.073	3.8	2171	10.9	0.138	9.3
	No.	1942	9.7	0.080	4.1	1942	9.7	0.168	10.5
	No.	2482	12.4	0.066	4.0	2482	12.4	0.158	11.7
	AV	2166	10.8	0.073	4.0	2198	11.0	0.155	10.5
	S.D	282	1.4	0.007	0.2	271	1.4	0.015	1.2

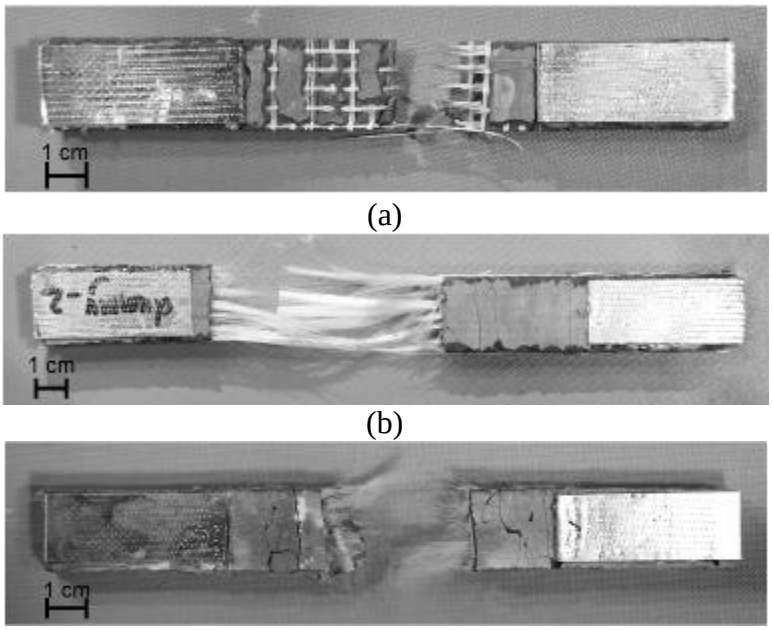

Figure 3.15 Typical composite samples after testing: a) laminated AR-glass TRC, b) knitted AR-glass TRC, and c) knitted polypropylene TRC

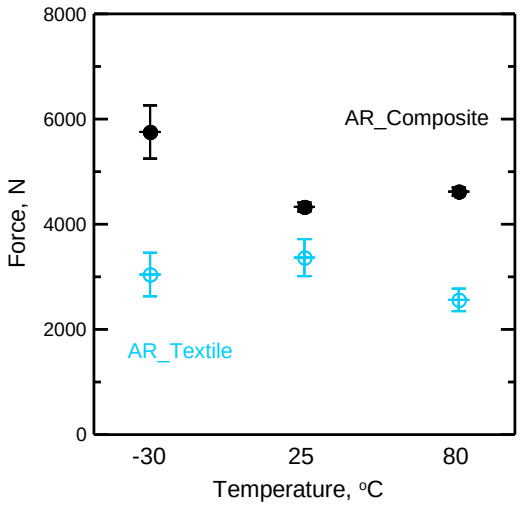

(a)

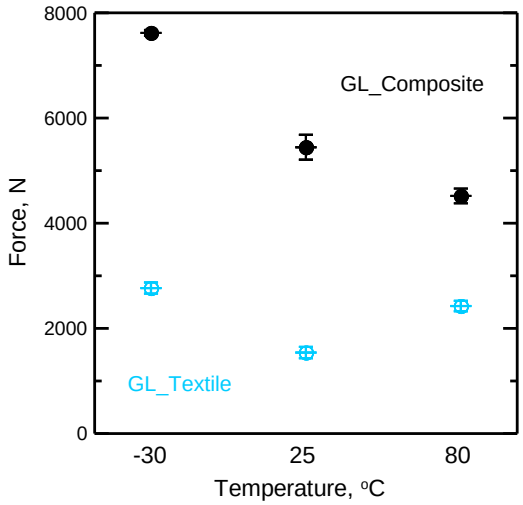

(b)

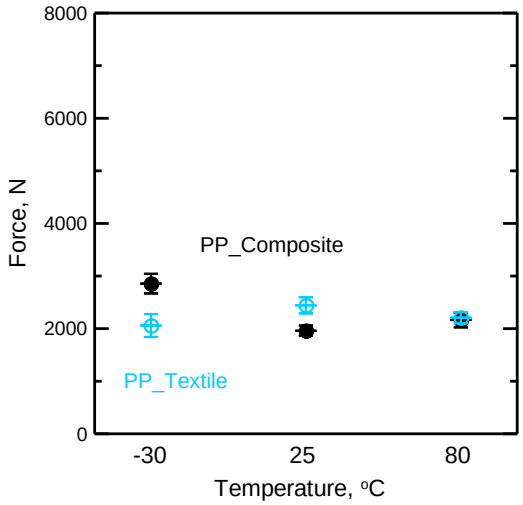

(c)

Figure 3.16 Effect of temperature on the maximum force capacity of various textiles and composites

3.5 Image Analysis

Figure 3.17 shows the sample with a contrasting speckle pattern on the surface, which is required by DIC technique. Flat paints of black and white color were used to generate these speckle patterns as black and white show a high contrast.

For the high quality images, high speed camera was only used to take images of samples testing under room temperature without the environmental chamber.

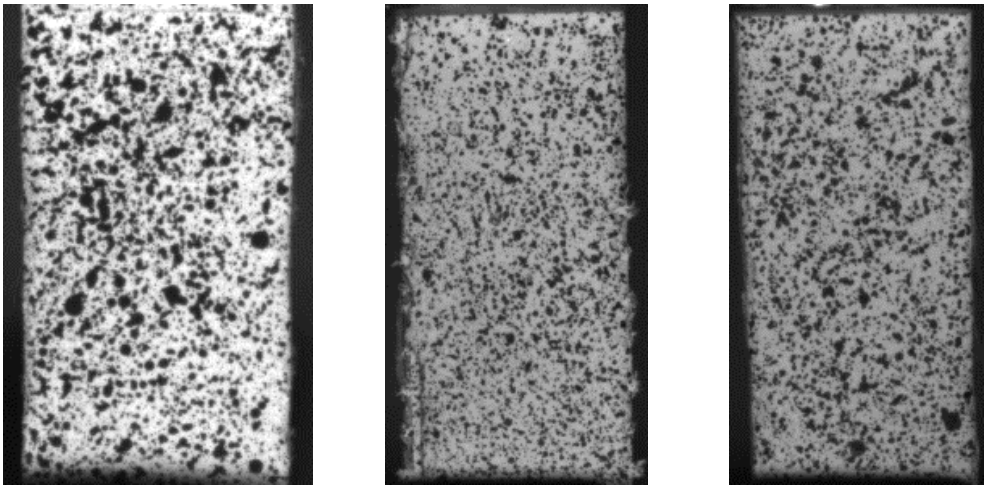

(a) (b) (c)

Figure 3.17 Speckle images of three different types of specimens: (a) PP, (b) SG, (c) GL

For the tension test, longitudinal strain ε_{yy} is of authors' interest and has been investigated using DIC method. Strain field development with time is shown in Figure 3.18. According to the legend on the right, color of purple stands for zero strain while the red is 5%, while for glass red stands for 3%. Figure 3.18a shows the time lapsed images of polypropylene. A main crack in the middle portion of the sample can be observed, where the strain concentration around this area has also been detected by DIC. However, in fact a lot more extremely fine cracks were formed during the test, which can be seen in Figure 3.38a taken by a DSLR camera with much higher resolution. But for the phantom camera to record with a high frame rate, which is 10,000 fps, the resolution has to be decreased, 256 x 512 in this project. For image analysis, acquiring more effective images turns out to be more important than a higher resolution. Thus a compromise of reducing the

resolution was made. Additionally, another region with strain concentration is the bottom part near the end grips. The edge effect is attributed to the gripping force provided by the fixture since the frictional gripping systems are usually employed for the tensile tests. As a result, large compressive force is applied on both ends of the specimen to generate friction when the test starts. Similar phenomenon can be observed on AR and GL composites: strain concentration around the main crack in the middle and the region close to end grips.

Based on the time lapsed images and the whole process of the test, three regions regarding different locations and level of deformation can be defined as follows:

Region I -- Strain concentration near the end grips;

Region II -- Strain concentration in the middle part;

Region III – Lower level of deformation indicating uncracked concrete or fine cracks.

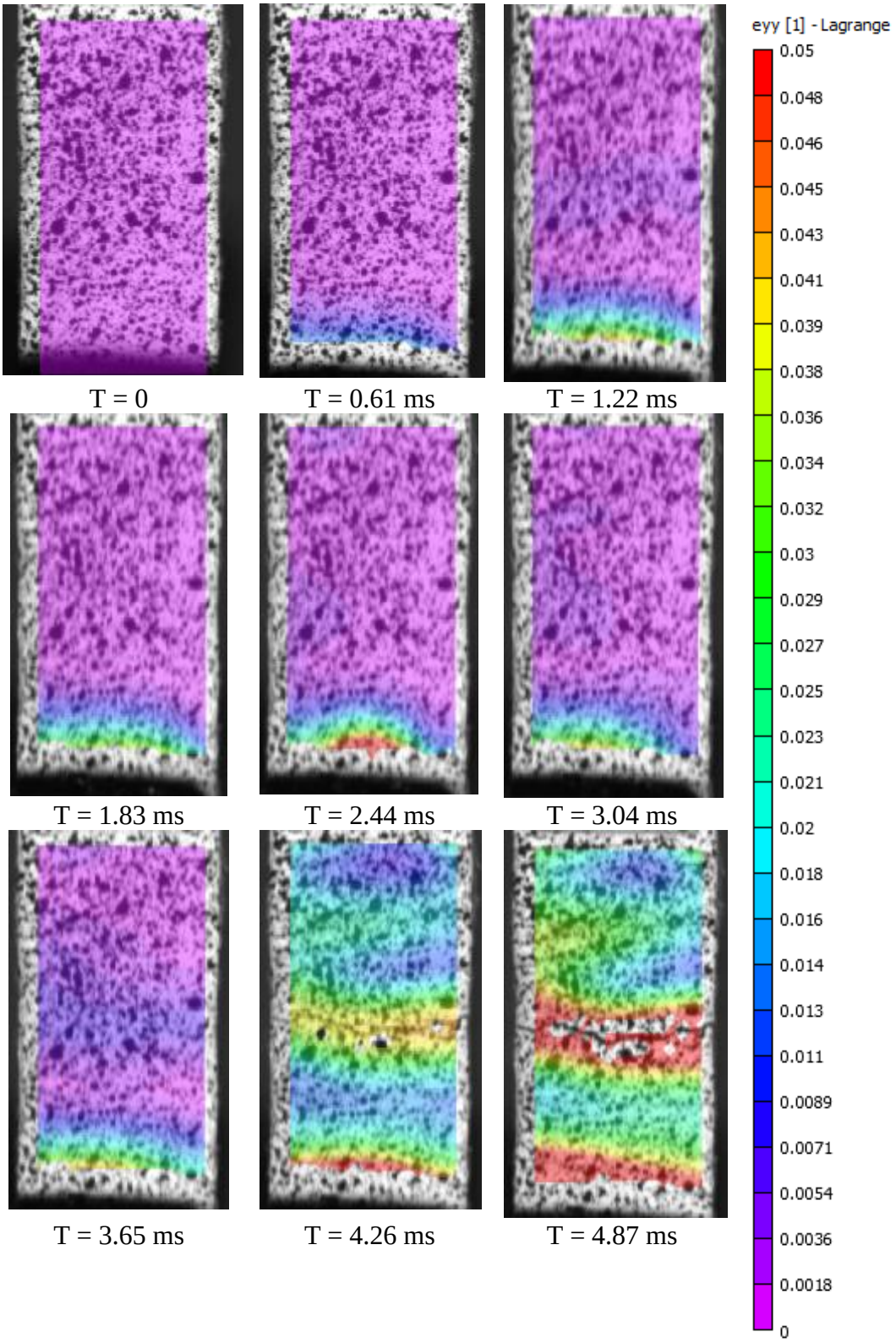
eyy [1] - Lagrange
0.05
0.048
0.046
0.045
0.043
0.041
0.039
0.038
0.036
0.034
0.032
0.03
0.029
0.027
0.025
0.023
0.021
0.02
0.018
0.016
0.014
0.013
0.011
0.0089
0.0071
0.0054
0.0036
0.0018
0
T = 0
T = 0.61 ms
T = 1.22 ms
T = 1.83 ms
T = 2.44 ms
T = 3.04 ms
T = 3.65 ms
T = 4.26 ms
T = 4.87 ms

(a)

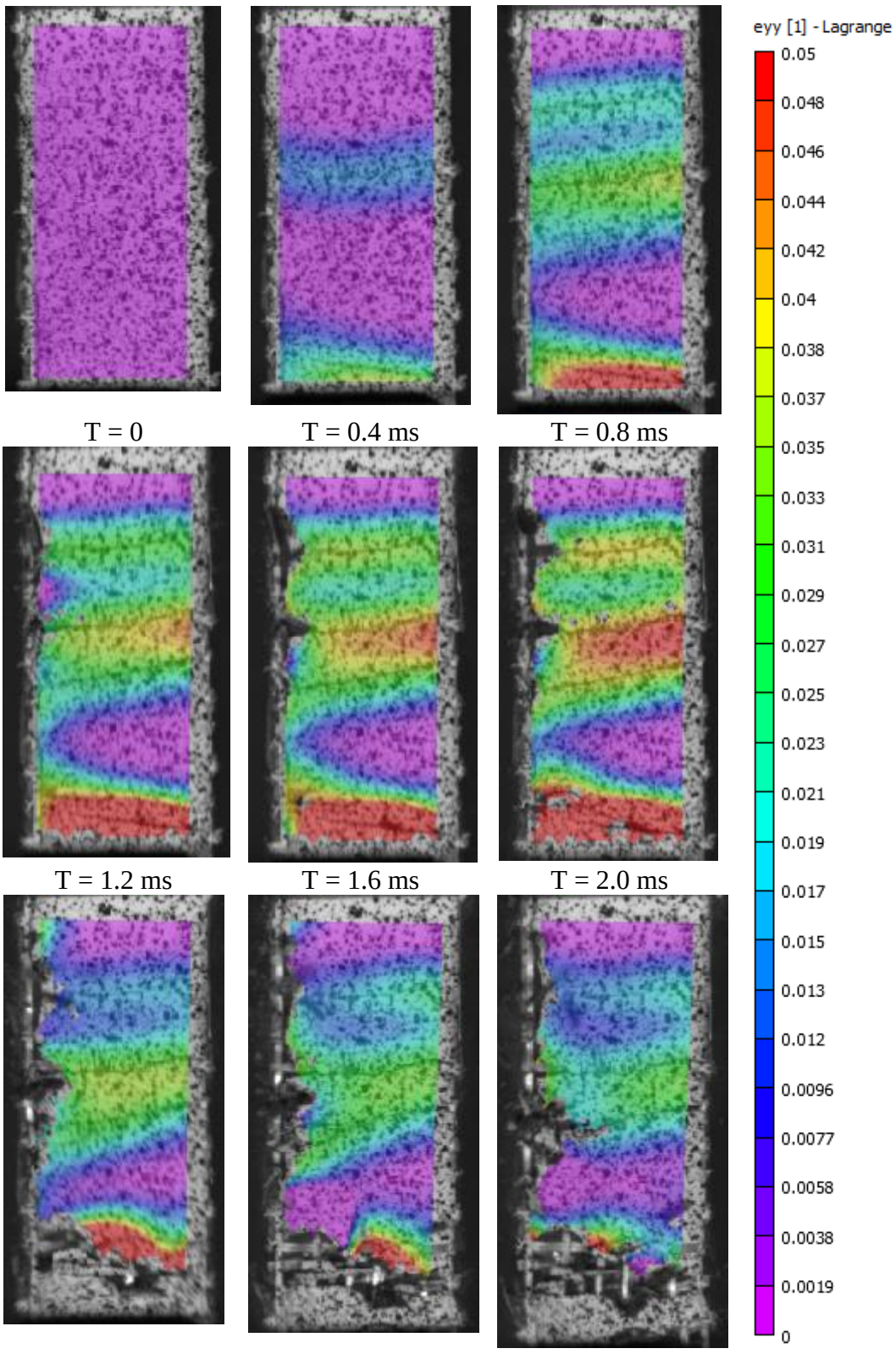
eyy [1] - Lagrange
0.05
0.048
0.046
0.044
0.042
0.04
0.038
0.037
0.035
0.033
0.031
0.029
0.027
0.025
0.023
0.021
0.019
0.017
0.015
0.013
0.012
0.0096
0.0077
0.0058
0.0038
0.0019
0
T = 0
T = 0.4 ms
T = 0.8 ms
T = 1.2 ms
T = 1.6 ms
T = 2.0 ms
T = 2.4 ms
T = 2.8 ms
T = 3.2 ms

(b)

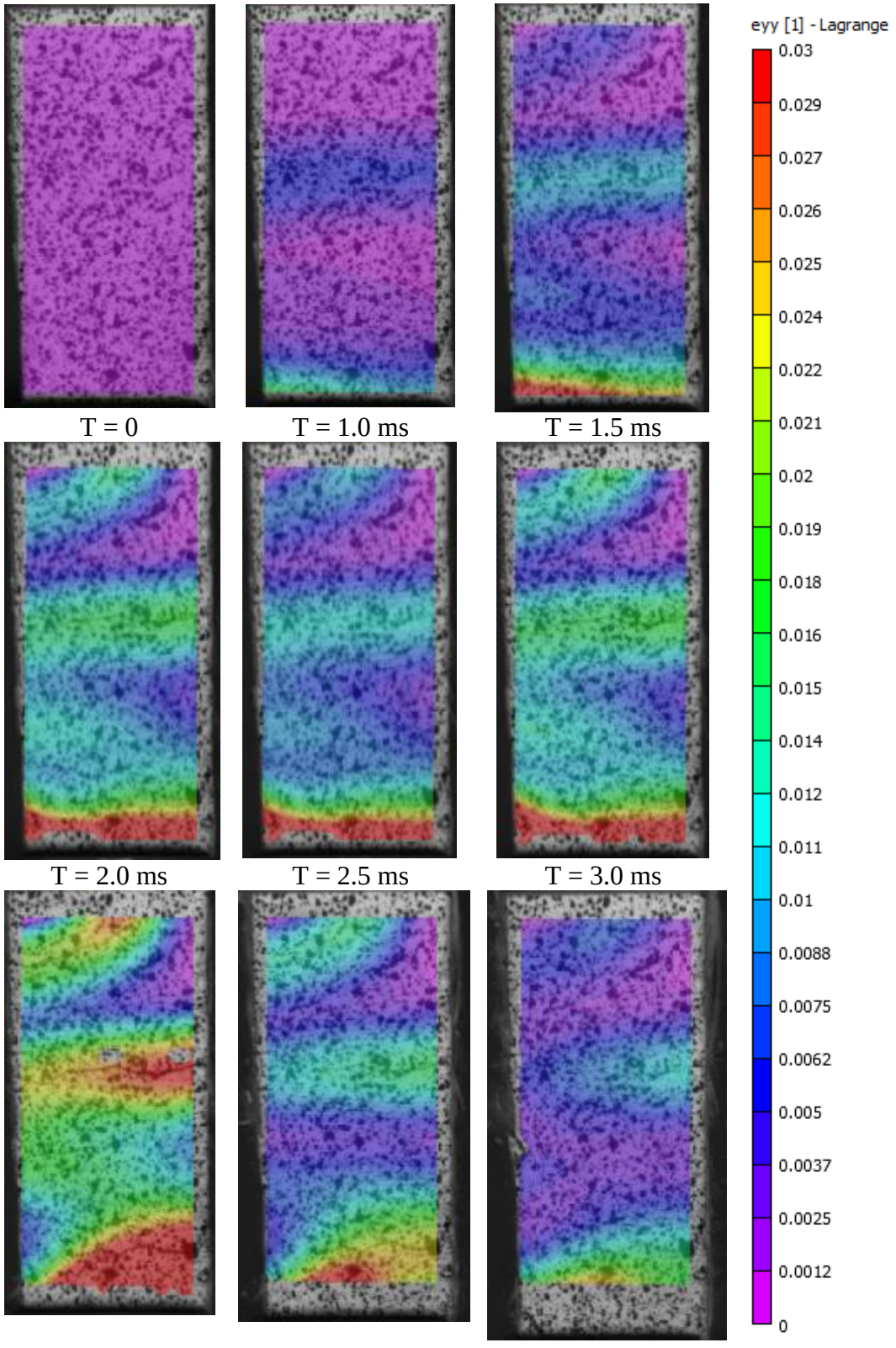
eyy [1] - Lagrange
0.03
0.029
0.027
0.026
0.025
0.024
0.022
0.021
0.02
0.019
0.018
0.016
0.015
0.014
0.012
0.011
0.01
0.0088
0.0075
0.0062
0.005
0.0037
0.0025
0.0012
0
T = 0
T = 1.0 ms
T = 1.5 ms
T = 2.0 ms
T = 2.5 ms
T = 3.0 ms
T = 3.5 ms
T = 4.0 ms
T = 4.5 ms

(c)

Figure 3.18 Time lapsed images showing the development of strain field for (a)PP, (b)SG, (c)GL composites

Traditional analysis of strains deals with a globalized deformation behavior, as the strain is calculated using the division of actuator displacement into the gauge length. However, the displacement of actuator is not the real elongation of the sample for the several reasons. First of all, slippage between sample and fixture or among the components does exist in frictional gripping system, see Figure 3.19. In that the nominal strain can be larger than the real deformation. In addition, the concept of nominal strain is based on the assumption that the strain is uniform distributed along the entire volume or length of the specimen. Nevertheless, strain filed distribution is quite non-uniform due to many effects, such as non-homogeneity of materials, defects, formation of cracks, stress concentration, etc. It can also be seen from the time elapsed images discussed before (see Figure 3.18). As a result, it is important to investigate the localized deformation of the materials. Strain responses at specific spots and average strain along lines were exported, processed and presented below.

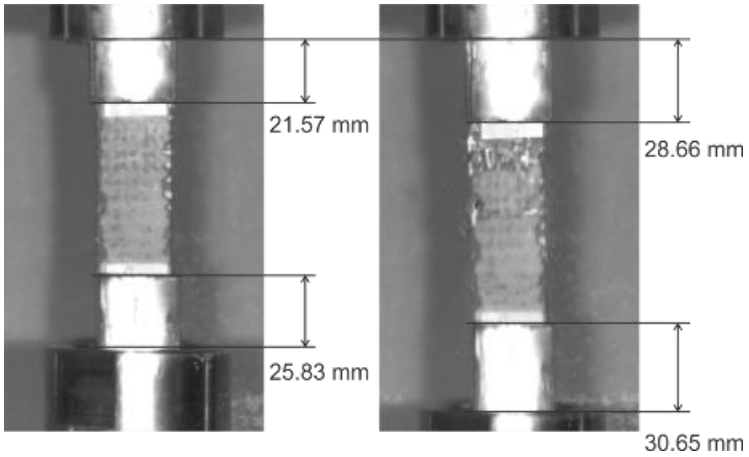

Figure 3.19 Slippage between the wedges and fixture occurred in the test measured as 11.19 mm

Five points on the surface of PP composite located in the different regions were selected (see Figure 3.20): 1 and 2 are located in region III, 3 and 4 are in region 2 while 5 from region I. Matlab programs have been developed to process the data including interpolation, smoothing, and correlating with the data recorded from MTS high speed machine.

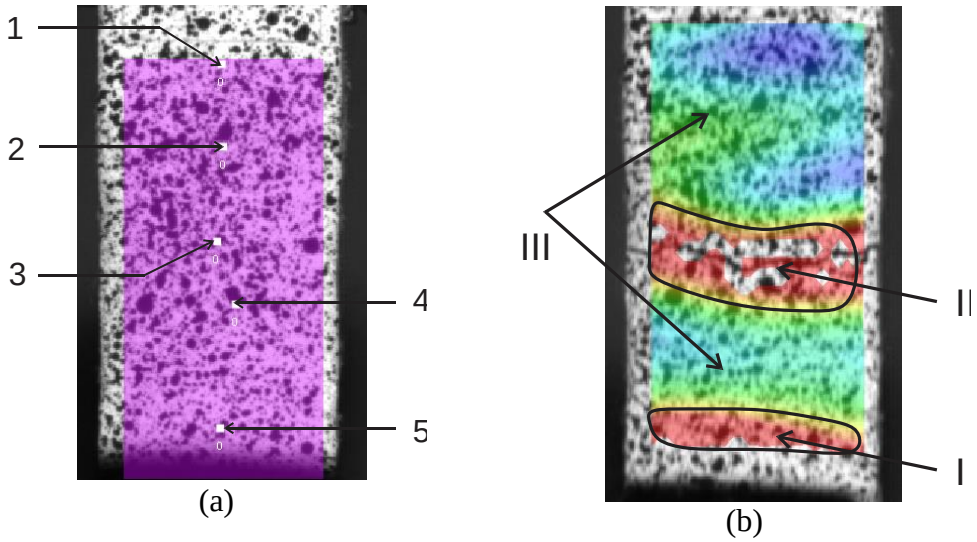

Figure 3.20 (a) Point selection, and (b) region dividing of polypropylene TRC

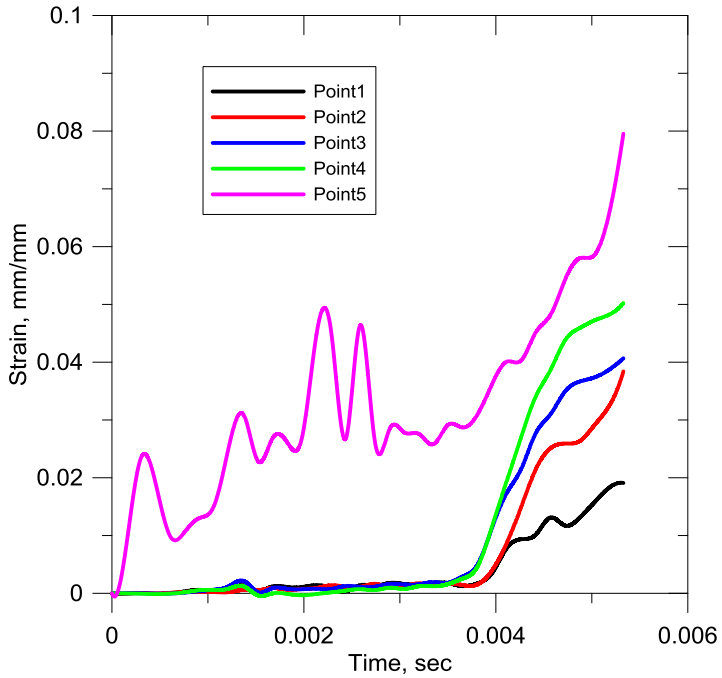

(a)

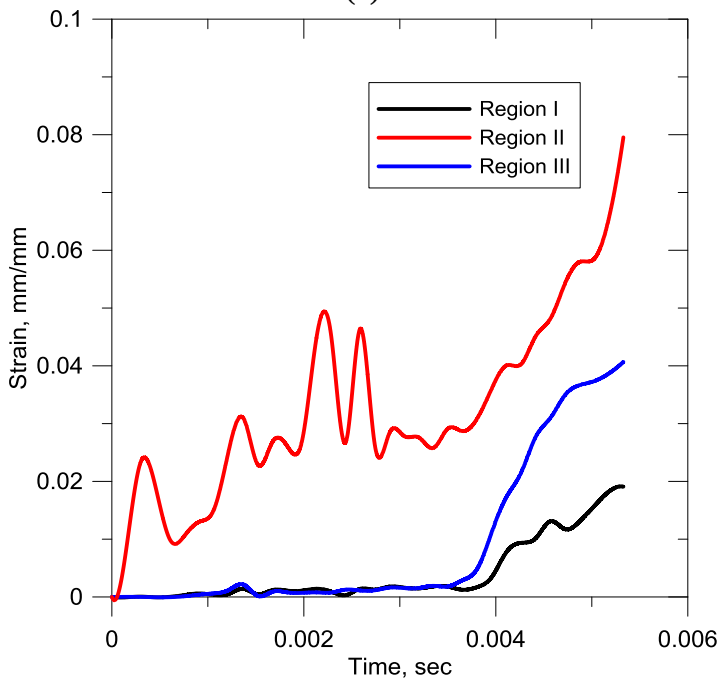

(b)

Figure 3.21 Strains responses at (a) selected points, and (b) representative responses at different regions.

Figure 3.21a represents the strain versus time responses at the 5 selected locations. As discussed above, strains points 1, 2 (region I) are smaller than those

of points 3 and 4 (region II), due to the effect of strain concentration along the main crack. However, longitudinal strain at point 5 increases much faster and ends up with a higher ultimate strain than all the other responses, due to the fact that failure happened near the bottom edge. In addition, as a feature of dynamic test, vibrations of the strain can be observed, specifically for point 5. One representative curve in each region has been selected to describe the whole process of deformation. Similar phenomenon can also be seen from the results of SG and GL composites, as shown in Figure 3.24-3.34.

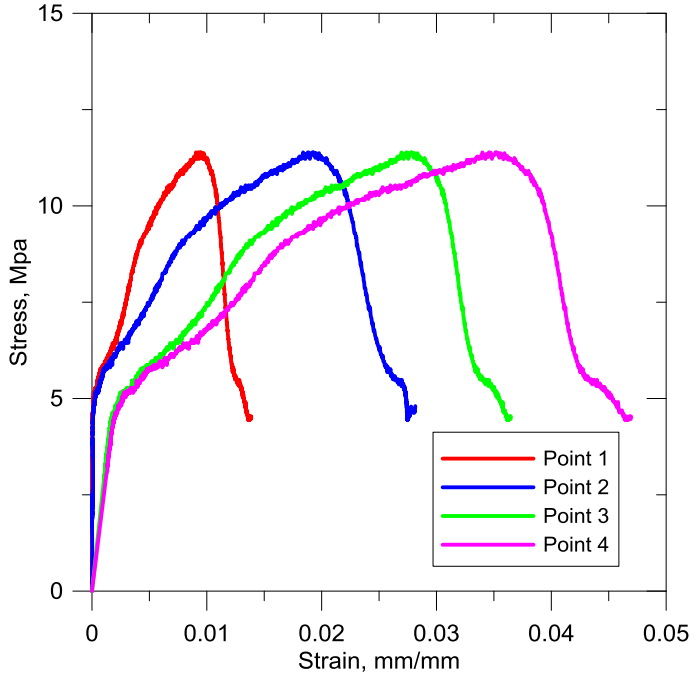

Figure 3.22 Stress-strain responses at selected points

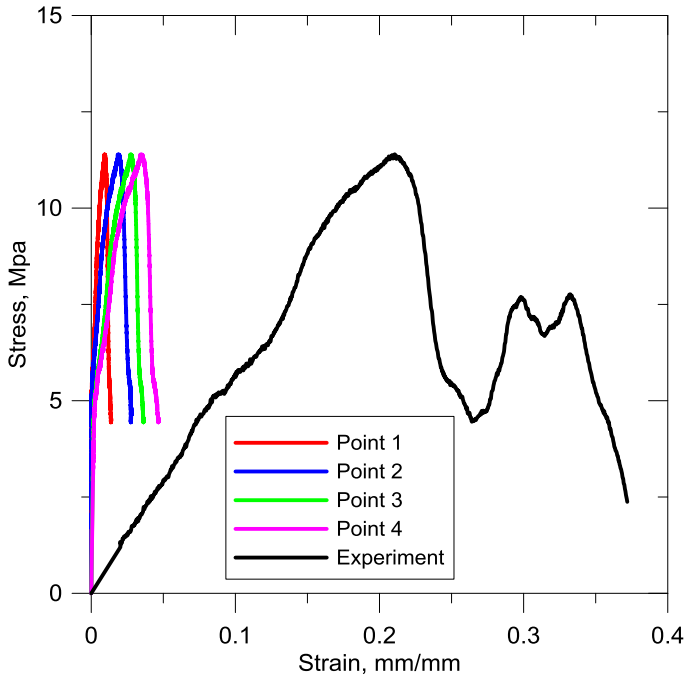

Figure 3.23 Comparison between image analysis and traditional analysis

Data acquired from high speed machine including time, force and displacement have been correlated to the strain data obtained from DIC using a MATLAB code. Stress strain responses are shown in Figure 3.22. Due to the large vibration of strain at point 5 during pre-peak stage, stress strain response cannot show an initial linear portion. So it is not presented in the figure. Figure 3.23 compares the stress-strain curves between DIC method and traditional method of data processing. Stress-strain curves of SG and GL composites are shown in Figure 3.24-3.34.

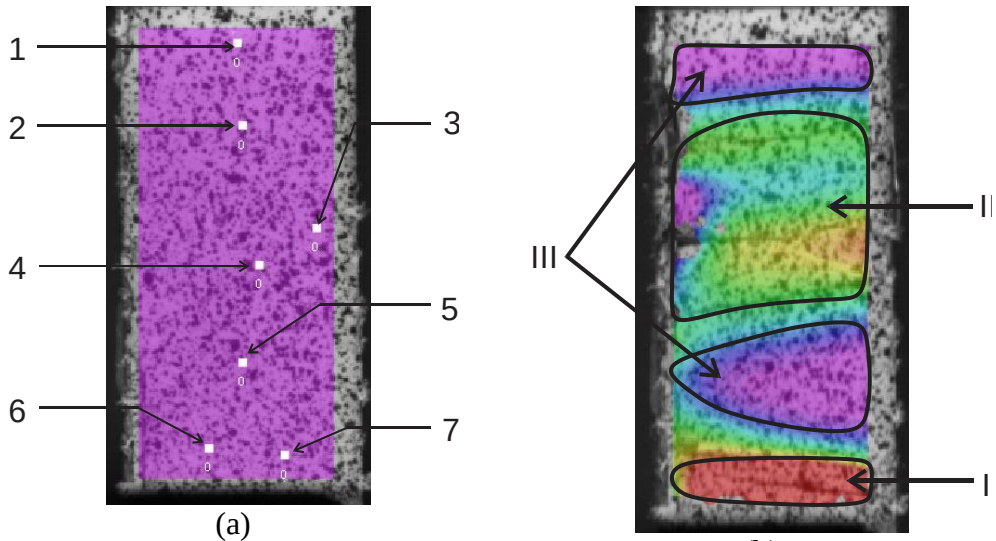

(a) (b)

Figure 3.24 (a) Point selection, and (b) region dividing of standard glass

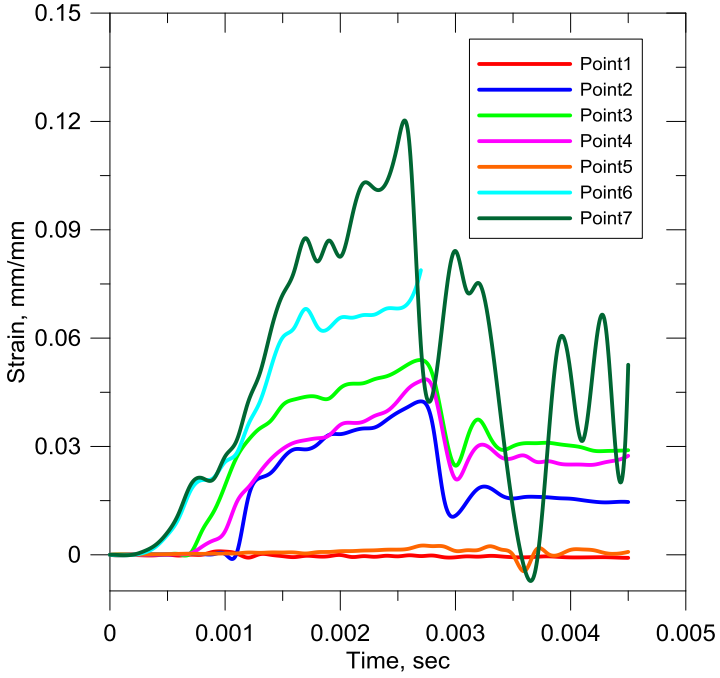

(a)

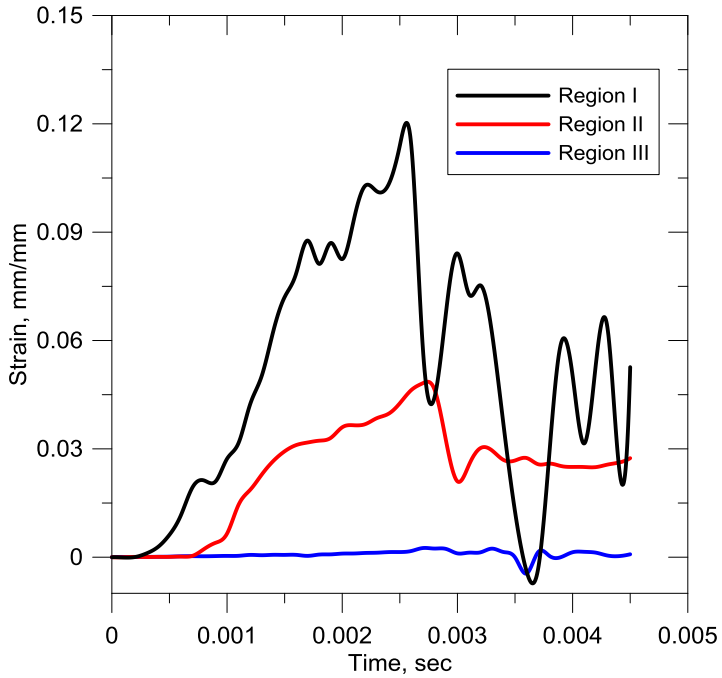

(b)

Figure 3.25 Strains responses at (a) selected points, and (b) representative responses at different regions.

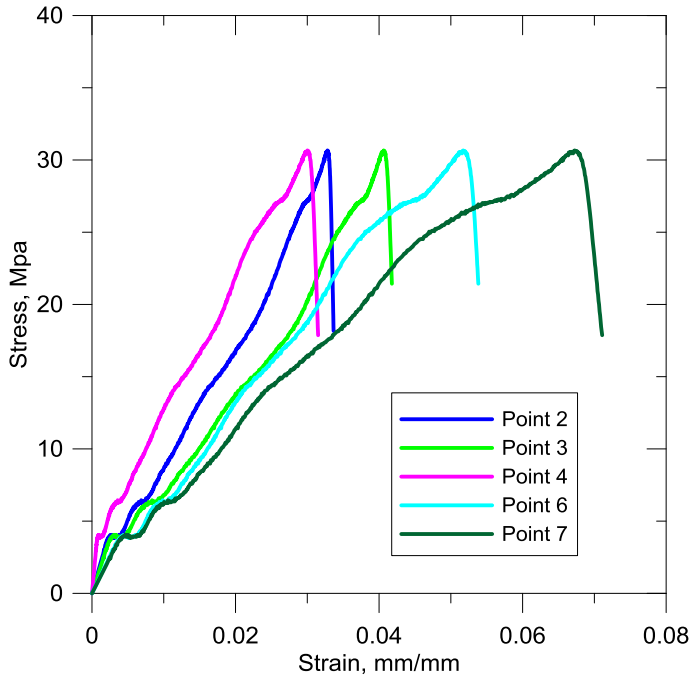

Figure 3.26 Stress-strain responses at selected points

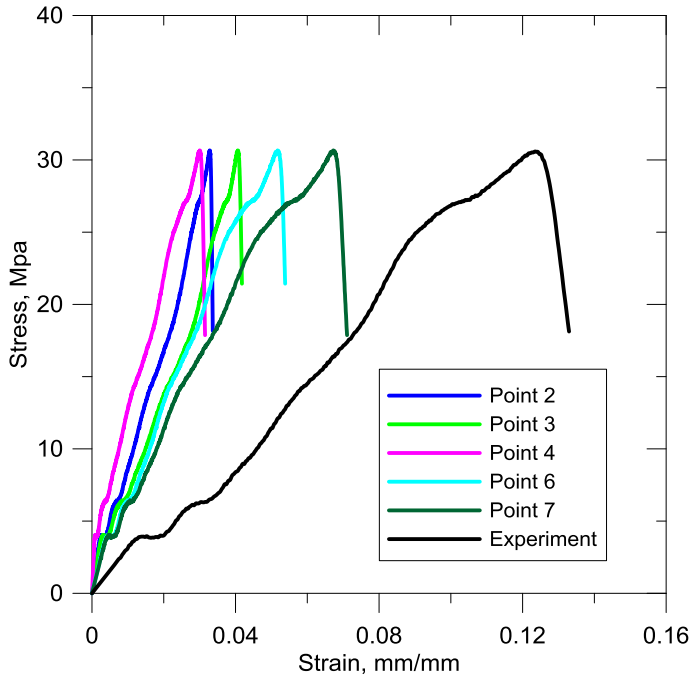

Figure 3.27 Comparison between image analysis and traditional analysis

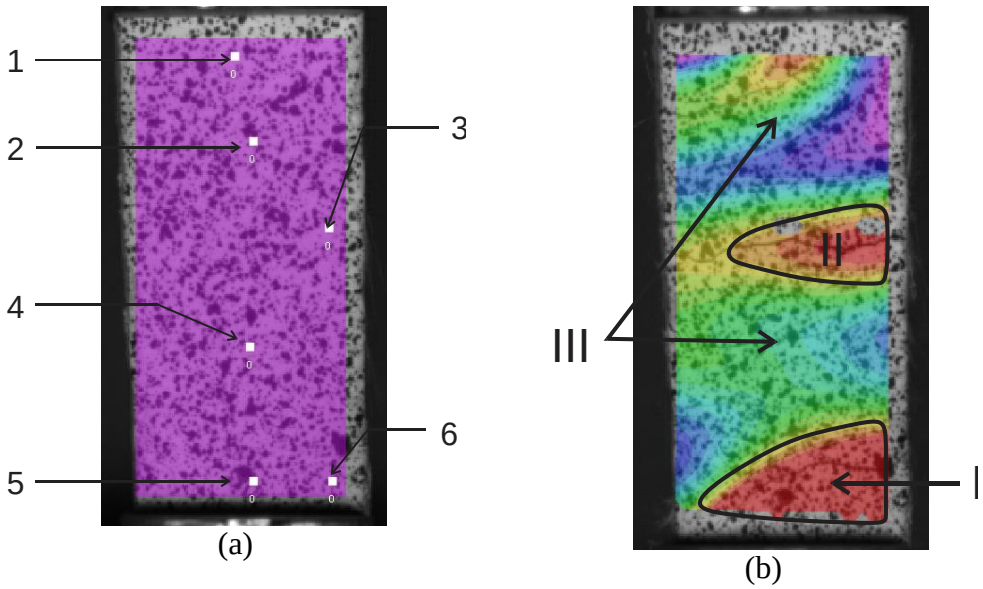

Figure 3.28 (a) Point selection, and (b) region definitions of standard glass

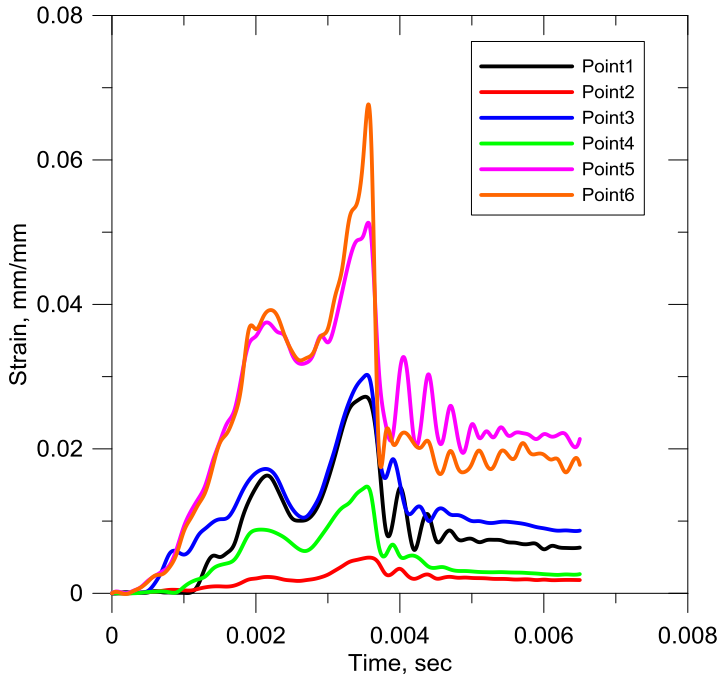

(a)

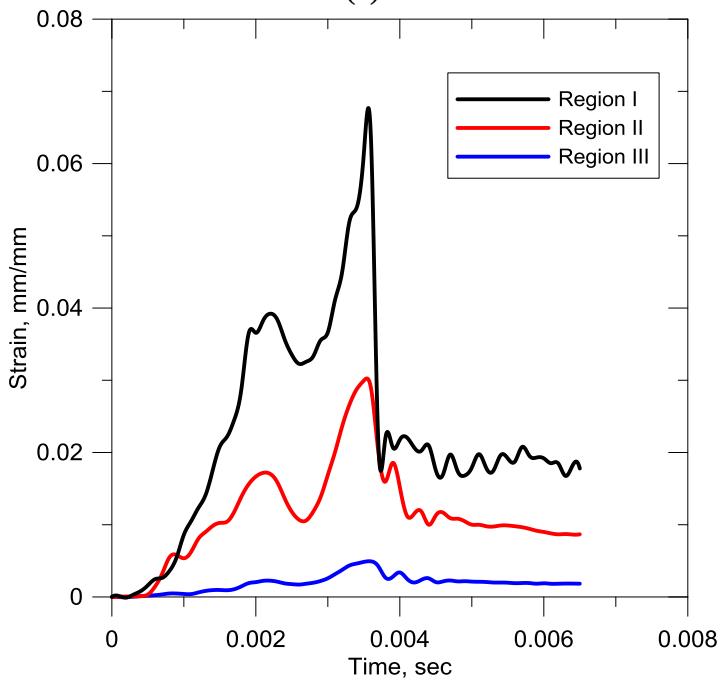

(b)

Figure 3.29 Strains responses at (a) selected points, and (b) representative responses at different regions.

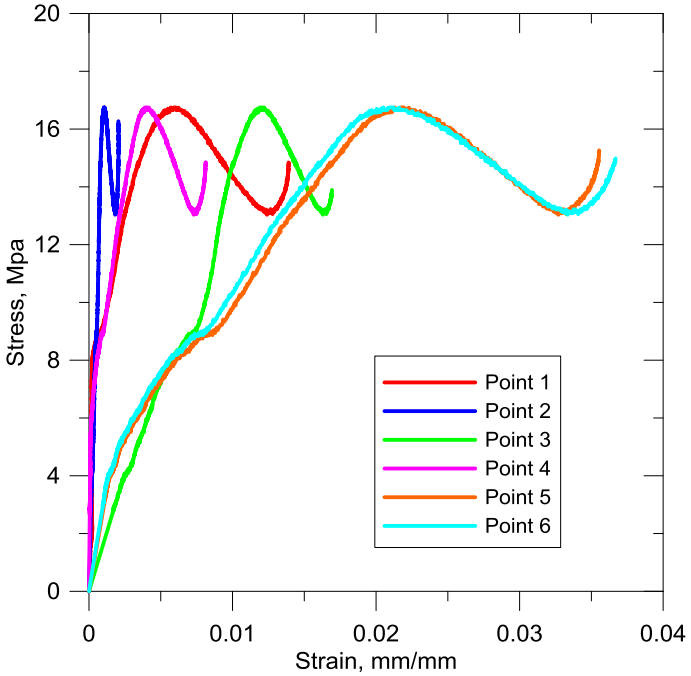

Figure 3.30 Stress-strain responses at selected points

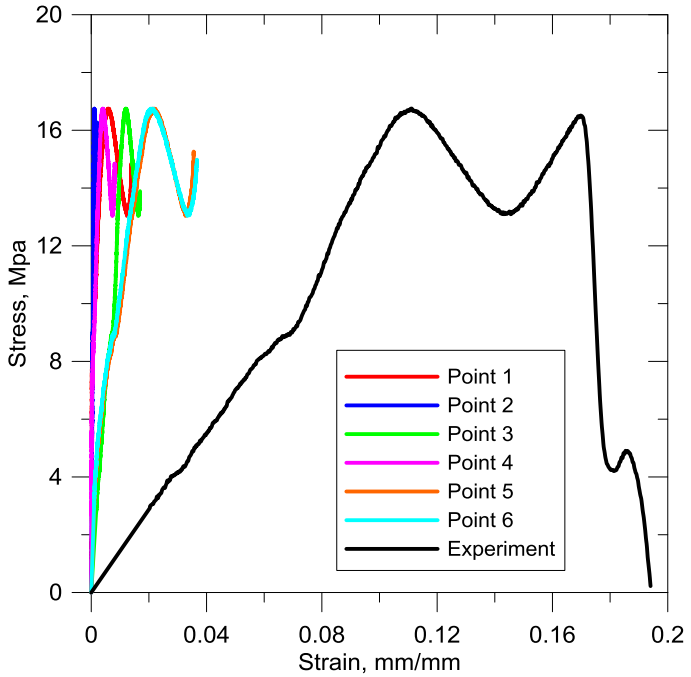

Figure 3.31 Comparison between image analysis and traditional analysis

To study the localized mechanical behavior of a material, the results will be more reliable if more locations are selected for analysis. However, it is cumbersome to investigate hundreds of spots one by one. So besides the study of deformation at points, analysis of average strain along some selected lines has also been conducted.

Seven lines on the surface of PP composite were selected to investigate the average longitudinal strain and strain distribution, see Figure 3.35a. Corresponding to the dividing of three regions, rules of line selection include:

- Lines located in region III (1 and 5);
- Lines located in region I and II (2, 3, 4 and 6), these lines are usually selected adjacent to the cracks;
- Vertical lines across the entire length of the area of interest (AOI).

Average strain of all the points on the line was calculated and processed. Strains versus time responses are shown in Figure 3.35b. All the responses show the similar trend and range of strain values with the data of specific points. Due to the fact that lines 1 and 5 are located in region III where the deformation is less compared to other areas, ultimate strains of lines 1 and 5 are obviously lower than others. Similar to strain response at point 7 which is close to the bottom grips (Figure 3.21a), strain response of line 6 along the bottom edge also shows a faster increasing and larger range of vibration from beginning. Again, its ultimate strain is dramatically larger than that of other lines. Specifically, since line 7 is across all three regions, so the strain response is supposed to be an average level out of all the data as can be seen in the figure.

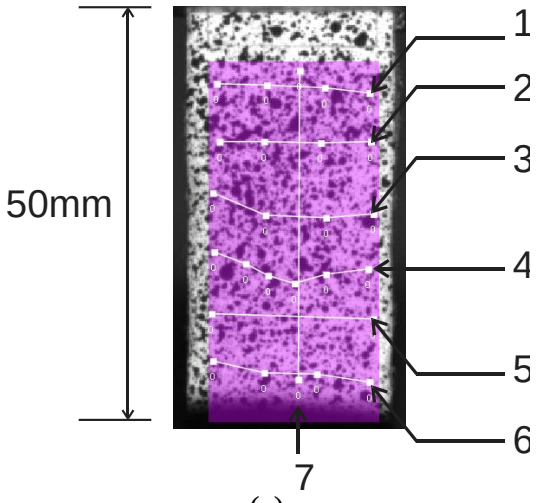
50mm
1
2
3
4
5
6
7

(a)

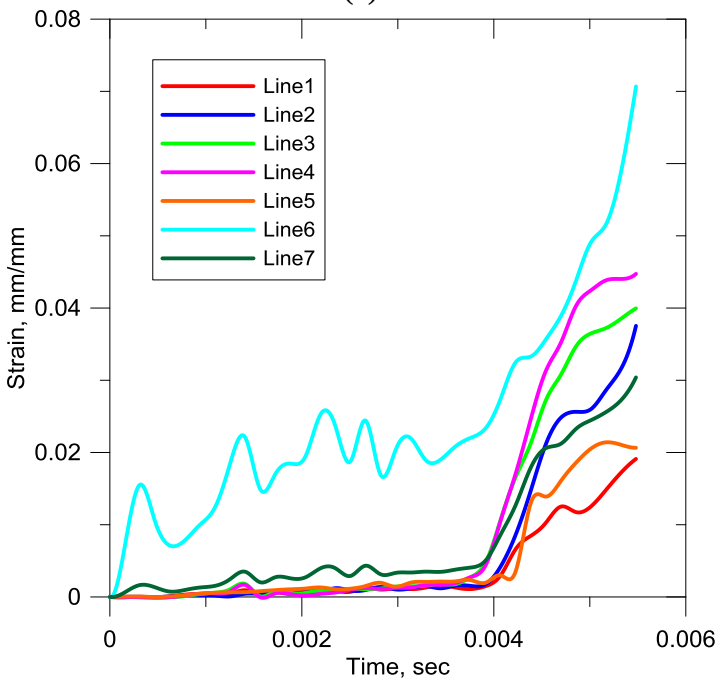
Line1
Line2
Line3
Line4
Line5
Line6
Line7
Strain, mm/mm
Time, sec
0.08
0.06
0.04
0.02
0
0.002
0.004
0.006

(b)

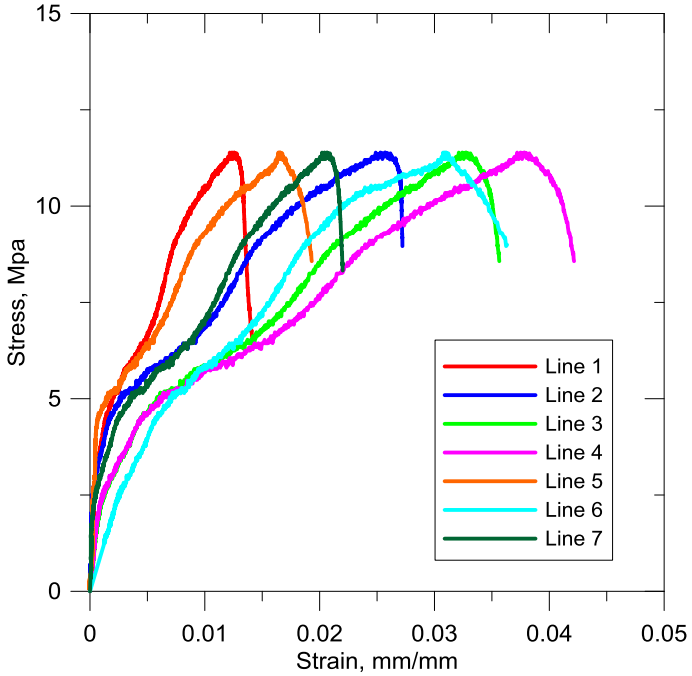

(c)

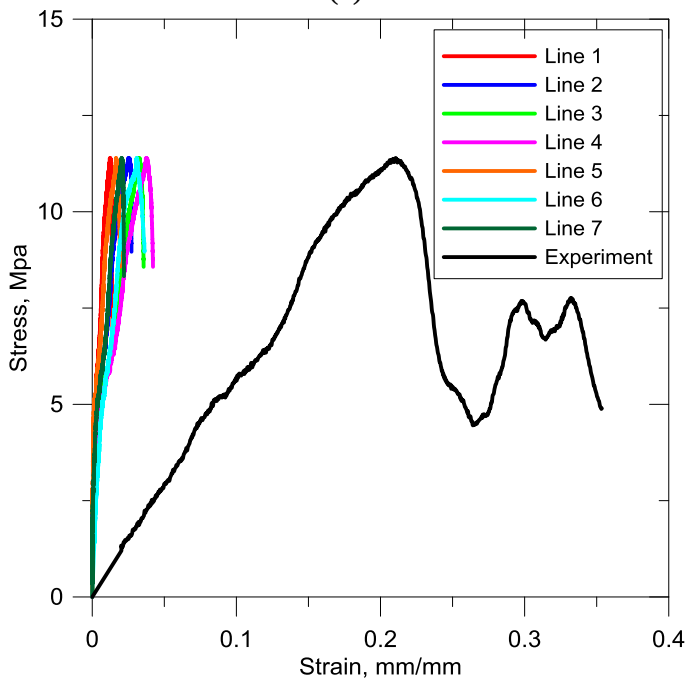

(d)

Figure 3.32 (a) Line Selection, (b) Strain responses of selected lines, (c) Stress-strain responses of selected lines, (d) Comparison between image analysis and traditional analysis

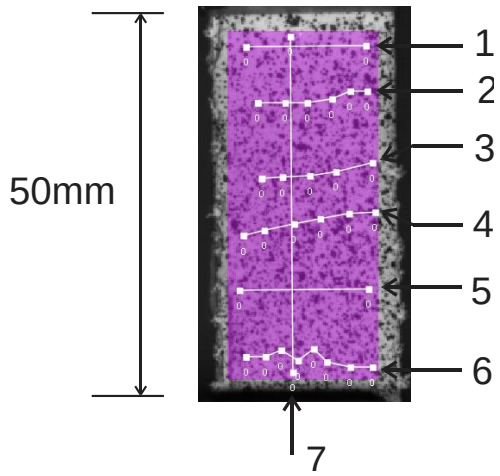
50mm
1
2
3
4
5
6
7

(a)

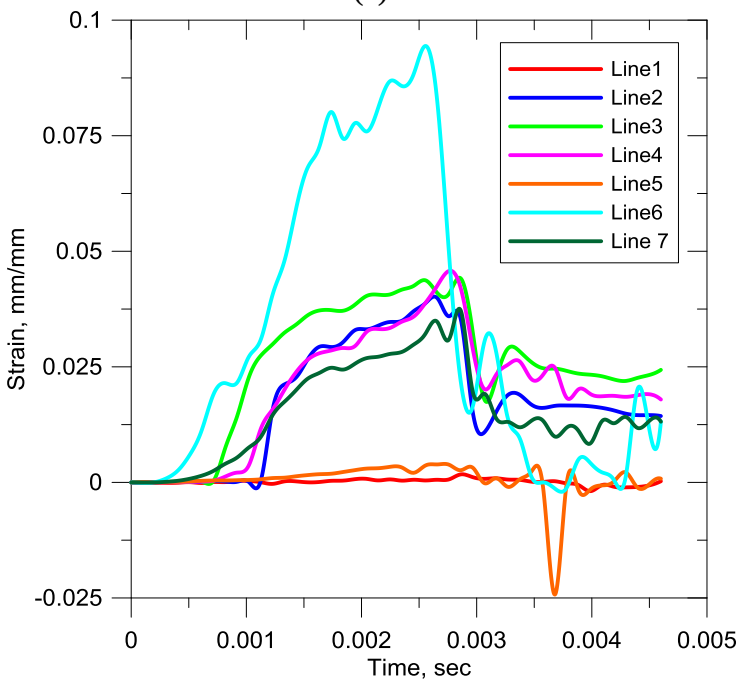
Strain, mm/mm
Time, sec
Line1
Line2
Line3
Line4
Line5
Line6
Line 7
0.1
0.075
0.05
0.025
0
-0.025
0
0.001
0.002
0.003
0.004
0.005

(b)

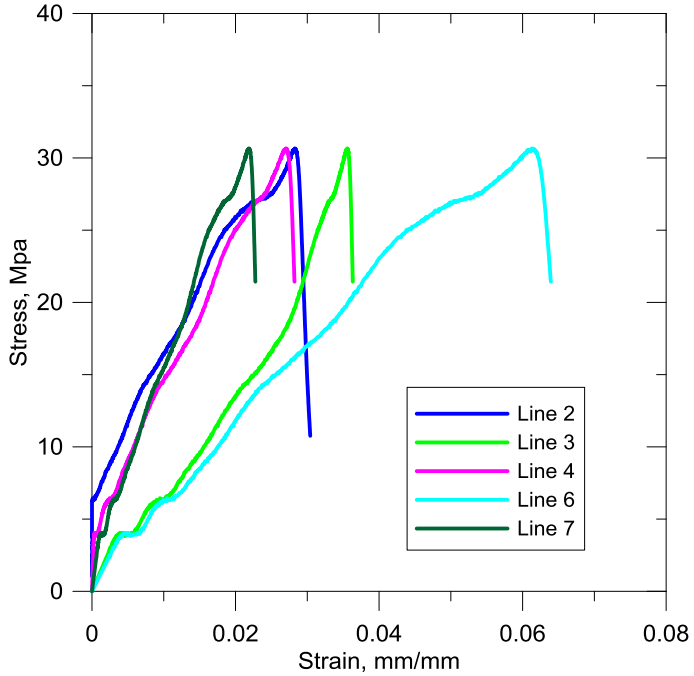

(c)

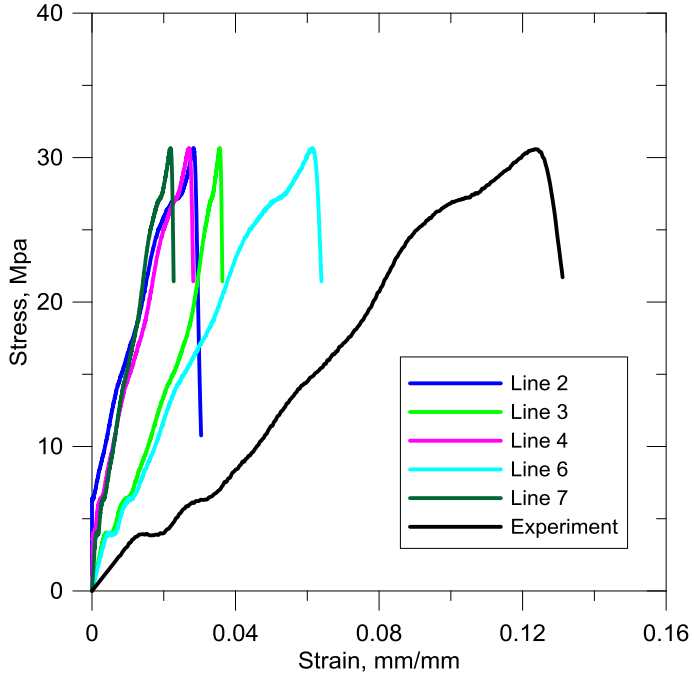

(d)

Figure 3.33(a) Line Selection, (b) Strain responses of selected lines, (c) Stress-strain responses of selected lines, (d) Comparison between image analysis and traditional analysis

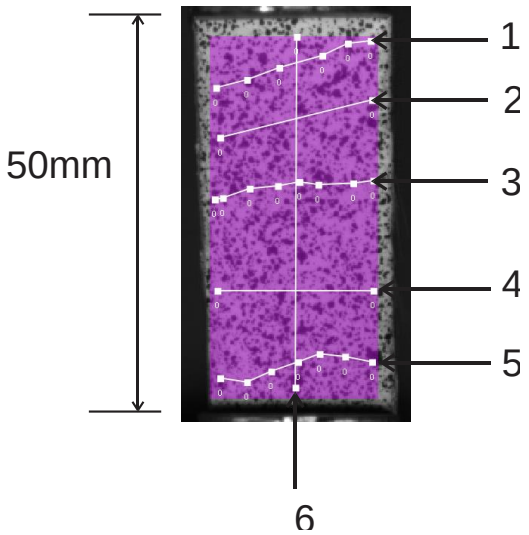
50mm
1
2
3
4
5
6

(a)

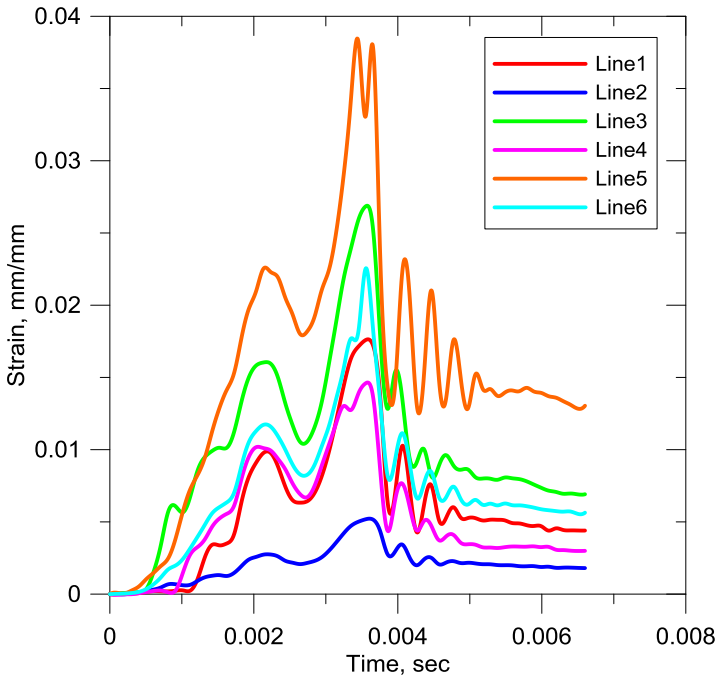
0.04
0.03
0.02
0.01
0
Strain, mm/mm
0
0.002
0.004
0.006
0.008
Time, sec
Line1
Line2
Line3
Line4
Line5
Line6

(b)

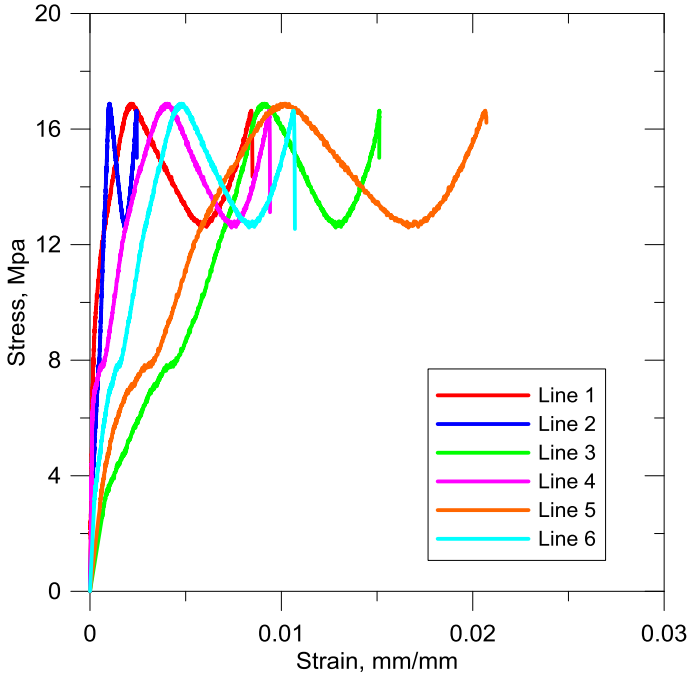

(c)

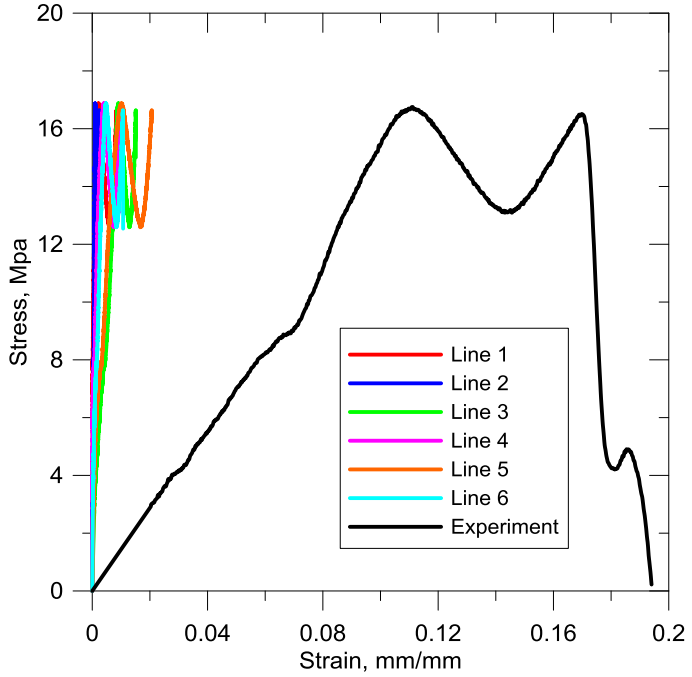

(d)

Figure 3.34 (a) Line Selection, (b) Strain responses of selected lines, (c) Stress-strain responses of selected lines, (d) Comparison between image analysis and traditional analysis

Figure 3.35 represents the longitudinal strain distribution along the axial direction of the composites. Abscissa stands for the axial location of the sample, where the origin corresponds to the bottom end. Similar phenomenon with previous discussion can also be seen and quantified. First of all, highest strain values are found to be at left end of the curves, which is the bottom end held by grips. Also, the vibration is detected again as the strains go back and forward. Additionally, strain values in the middle portion of the curves are higher than the other parts between main region of main cracks and edges, which is attributed to the strain concentration caused by the formation of cracks. The discontinuity refers to the location of main cracks, where the speckle pattern is separated. Thus the correlation across the cracks is interrupted and the data near these regions are lost.

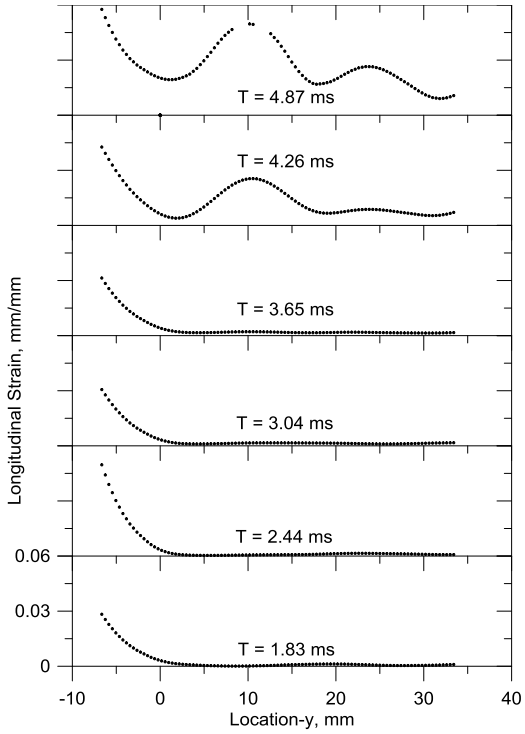

(a)

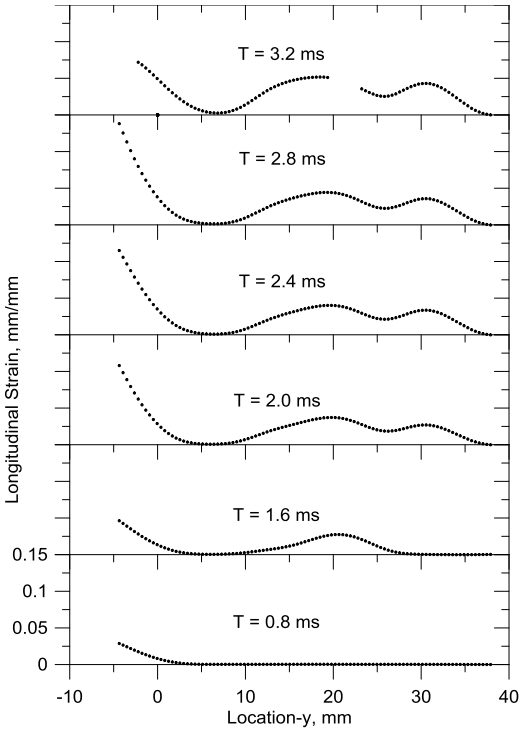

(b)

c

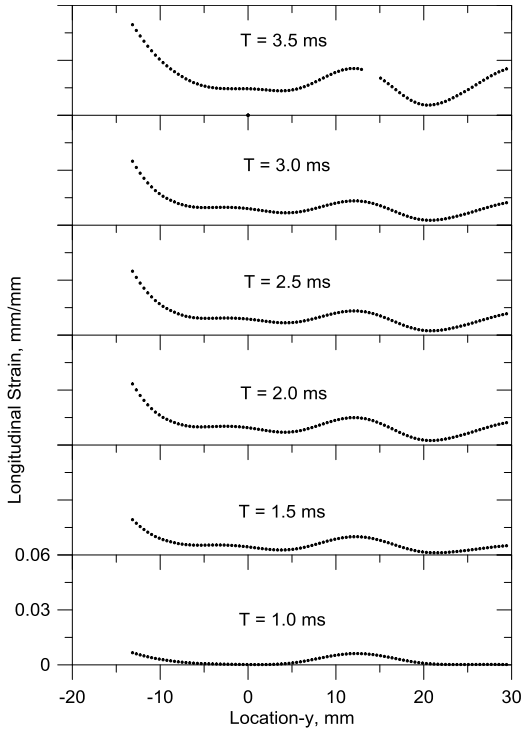

(c)

Figure 3.35 Strain distribution along the axial direction of the samples (a) PP, (b) SG and (c) GL

The last but not the least, the rest of the curves shows a relatively lower level of deformation. Strain distributions and the dividing of three regions discussed before confirm with each other very well.

3.6 Tension stiffening model

The finite difference tension stiffening model developed by Soranakom [77] was used to simulate the crack spacing and stress - strain response of the textile fiber reinforced composites under dynamic loads. In this model a cracked tension specimen is idealized as a series of 1-D segments consisting of fiber, matrix, and interface elements. The matrix is treated as brittle with no strain-softening response. As the load on the composite is increased such that the cracking stress of the matrix is reached, the matrix phase cracks, and the load is solely carried by the longitudinal yarns through the interface elements. The individual pullout segments are allowed to continue carrying the load at crack locations. In nonlinear analysis, an iterative solution algorithm is used to enforce load-deformations to follow the material constitutive laws. Once the slip distributions are solved and corresponding stress and strain responses are identified, results are added to represent the overall tensile response. The static model has a high bond strength and low slip range while the dynamic presents elastic plastic frictional shear with a longer slip range [**Error! ookmark not defined.**]. The material parameters were held constant for all the simulations and are described in Table 3-9.

Table 3-9 Input parameters for finite difference simulation

Fiber type	Fiber modulus (Gpa)	Fiber UTS (MPa)	Matrix modulus (Mpa)	Young's Modulus efficiency factor
PP	6.9	500	35000	1.0
Glass	78	1360	35000	1.0

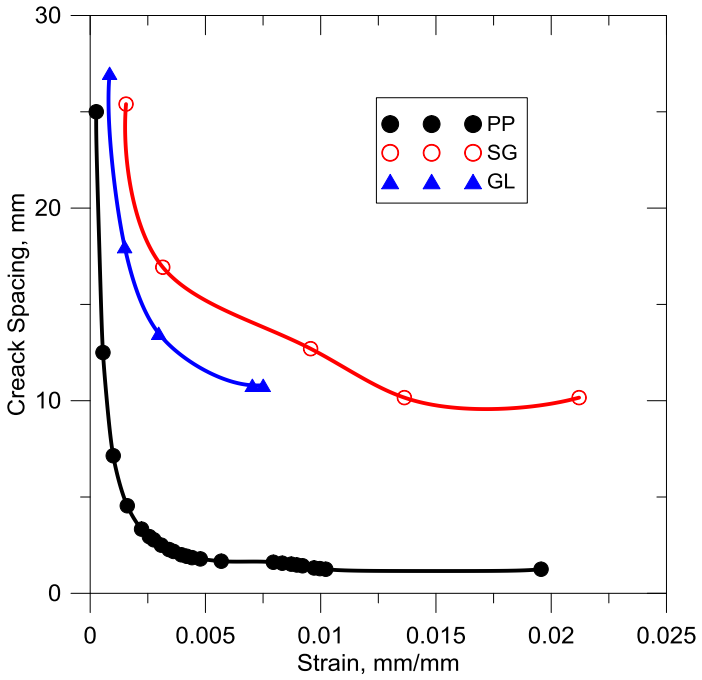

Figure 3.36 Numerical simulation of the strain and crack spacing

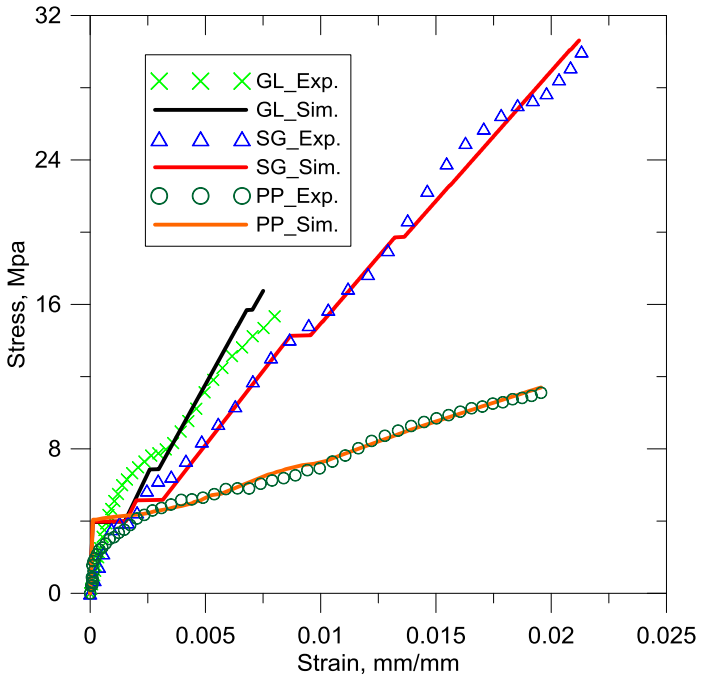

Figure 3.37 Comparison of numerical simulation and experimental data on tensile stress-strain response of TRC composites

A simulation of the dynamic test for three different types of composites was performed and the results are presented in Figure 3.36 and 3.37. It can be seen that the PP composites has the largest number of cracks and smallest average crack spacing, while SG composites has the largest crack spacing but much less cracks than PP (see Figure 3.38). It indicates that the bond strength between polypropylene and concrete is higher than that of glass fiber, which is not enough to transfer load from matrix to the fiber. Thus for SG and GL composites, the mechanism of failure of is then converted to significant fiber pullout resulting in high energy absorption. This phenomenon is confirmed by the pictures taken after testing (see Figure 3.38), which has been discussed at the beginning of this part.

(a)

(b)

(c)

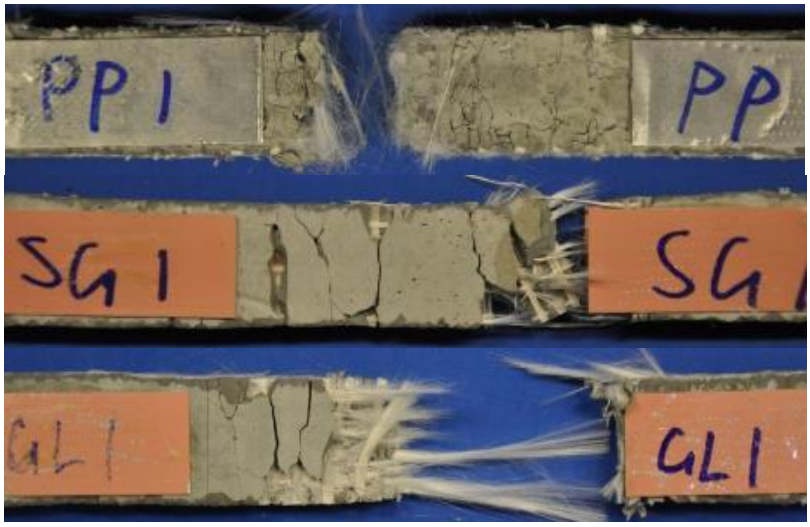

Figure 3.38 Distribution of cracks on the tested samples: (a) PP, (b) SG, (c) GL

3.7 Summary and Conclusions

High-strain tensile tests (100 s-1) were performed for three types of textiles and textile-reinforced cement composites. A fairly uniform tensile behavior was observed for various replicate composite samples, demonstrating the reliability of this high speed test method. The highest load capacity and toughness values were

related to the knitted glass textile composites, implying excellent bond between textile and cement matrix. Maximum tensile force of 5761±141 N (equivalent to 28.8±0.7 MPa) was obtained for this composite at room temperature. The load capacity for this composite was about three time higher than bundled textiles (4 textiles). Multiple cracking behavior was observed for these composites, indicating good stress transfer within these systems. The maximum load capacity and toughness increased with the reduction in temperature and decreased with the raise in temperature.

The lowest force capacity was related to the knitted polypropylene textile composite, implying weak bond between textile and cement matrix. Maximum tensile force of 2151±177 N (equivalent to 10.8±0.9 MPa) was obtained for this composite at room temperature. The load capacity for this composite was almost the same as the bundled textiles (4 textiles). Multiple cracking behavior was absent for these composites. Except for knitted glass textile composite, no specific trend was observed for the effect of temperature for other textile or textile cement composites.

The digital image correlation method was a powerful tool to determine the strain field in cement composites. A non-uniform distribution of longitudinal strain was observed in contrast with the assumption of traditional data analysis method. Strain concentration was detected around the main cracks and edges, indicating the concentrated stresses. Quantified study of strain responses confirms well with the strain field presented. Stress-strain curves combining mechanical parameters and

strain responses obtained from DIC method addresses the issue of slippage in the gripping system, showing more reasonable results.

The tension stiffening model used was able to accurately predict the crack spacing and stress – strain behavior of the textile reinforced cement composites under dynamic and loading condition. The model has shown that under dynamic load, a reduced frictional bond results in a lower capacity of fiber-matrix stress transfer leading to wider crack spacing and promoting a fiber pullout failure mechanism which increases the energy absorption capacity of the composite system.

4. STRAIN RATE EFFECT ON THE TENSILE BEHAVIOR OF TEXTILE-REINFORCED CONCRETE UNDER DYNAMIC LOADING

ABSTRACT

4.1 Introduction

Textile reinforced concrete is a relatively new class of cement composite system that presents a strain hardening behavior with enhanced strength and ductility. This material is strong enough to be used as load bearing structural members in applications such as structural panels, impact & blast resistance, repair and retrofit, earthquake remediation, strengthening of unreinforced masonry walls, and beam-column connections. Thus, the response to impulse loading, for applications in extreme loading conditions, becomes of great importance.

The dynamic tensile response of cement based material is a difficult experiment to perform with a few published results. Most of the available literature on the dynamic tensile behavior of concrete is based on investigations of plain concrete which exhibits an increase in tensile strength for increasing strain rates [78, 79, 80,81,82, 83]. For example, Xiao et al. [78] reported that the dynamic tensile strengths of concrete tested at strain rates of 10-4, 10-3 and 10-2 s-1 increase by 6%, 10% and 18%, respectively, when compared to that of quasi-static. Birkimer and Lindemann [79] reported that the concrete tensile strength tested at a strain rate of 20 s-1 ranged between 17.2 MPa and 22.1 MPa, while the static tensile strength was 3.4 MPa.

Dynamic tensile data on fiber reinforced concrete is even more limited. Zhu et al. [84] conducted tensile testing on three types of fabric-cement composites, PE,

AR Glass and carbon, under dynamic loads, using a servo-hydraulic testing machine. The strength of AR glass composite under high speed loading was found to be 35% higher than that tested under quasi-static loading condition. Also a significant difference was noticed in the strength, toughness and maximum strain of carbon composite between static and dynamic testing conditions. Kim et al. [85] investigated the strain rate effect on the tensile behavior of high performance fiber reinforced cement composites (HPFRCC) using two deformed high strength steel fibers, namely hooked fibers and twisted (Torex) fibers. The strain rate ranged from pseudo static (strain rate of 0.0001 s^{-1}) to seismic (strain rate of 0.1 s^{-1}). The results showed that the tensile behavior of HPFRCC with twisted fibers is sensitive to the strain rate, while hooked fiber reinforced specimens show no rate sensitivity. It was also observed that lower fiber volume fraction (V_f = 1%) reinforced specimens show higher sensitivity than higher volume fractions (V_f = 2%). Maalej et al. [86] performed dynamic tensile tests in Engineered Cement Composites (ECC) containing 0.5 % steel and 1.5 % polyethylene fibers (in volume). The applied strain rate ranged from $2x10^{-6}$ to $2x10^{-1}$ s^{-1}. The results indicated that there is a substantial increase in the ultimate tensile strength from 3.1 to 6 MPa with increasing strain rate. The strain capacity did not appear to be affected by the strain rate. The tensile behavior of TRC under static and dynamic loading at different strain rates ranging from 0.0001 to 50 s^{-1} was studied by Silva et al. [87]. For tensile tests performed up to 0.1 s^{-1} an increase in tensile strength, strain capacity, work-to-fracture, and first crack strength both for TRC with plain matrix and TRC with short fibres was observed. When tested at high strain rates from 5 s^{-1} to 50 s^{-1} the

TRC continued to tend to increasing tensile strength and work-to-fracture, but to a decrease in the strain capacity. This lower strain capacity was traced back to the increase in the stiffness of the composite in the post-crack region during the tensile test.

The response of TRC under impact loading has already been investigated [88]. It was reported that the maximum stress increases when increasing the impact energy sustaining high ranges of energy absorption capacity. Nevertheless, the TRC response under high speed tensile load and the influence of strain rate on its mechanical performance yet needs to be understood.

The addition of short fibers is known to be able to increase both the tensile strength and tensile toughness when used at sufficiently high volume fractions. However, the main effect of fibers on tensile response is the increase in toughness as they change the mode of failure from a brittle fracture to ductile behavior. Aveston et al. [89] addressed the mechanics of toughening in brittle matrix composites. Using energy balance, they showed the analytical foundations of increase strain capacity in composite systems when the fiber volume fraction exceeds a critical level. In recent years researchers have performed several test series to investigate the influence of short fibres on various properties of textile-reinforced concrete [90, 91]. Adding PVA micro-fibers to a plain concrete matrix has little effect on its pre-cracking behavior but does substantially enhance its post-cracking response, which leads to a greatly improved ductility and toughness, reported by Hamoush et al [92]. Their study also reveals that the addition of micro-fibers enhances the ductile property of the materials, increases toughness, and

prevents the sudden brittle failure of the material, although it does not influence the compressive strength of concrete. However, the mechanisms inherent in the joint action of short fibre and textile reinforcement are still not fully understood. In order to gain more and better insight into the specific material behavior of the finely grained concrete with such hybrid reinforcement, a new investigative program has been initiated the TU Dresden. Hinzen et al. [93] investigated the addition of short glass, aramid and carbon fibers in the tensile response of TRC. It was found an increase in the first crack strength up to 40 % and a finer crack pattern leading to an increase in the ultimate strain. Barhum [94] studied the effect of the addition of glass and carbon short fibers on the tensile behavior of TRC. The first-crack strength was doubled due to the addition of 1.0% by volume dispersed short glass fibres. The energy absorption capacity also increased due to the addition of the short fibers. Silva et al. also investigated the strain effect on the tensile behavior on TRC with and without addition of short fibers. It is observed that the addition of short fibres increased first-crack and tensile strength for strain rates up to 0.1 s−1. The work-to-fracture showed a slight tendency to decrease with the addition of 0.5% of short glass fibres, which can be traced back to decrease in strain capacity [87]. The effect of the inclusion of short fibers, under high strain rates, steel needs to be investigated.

In the present work the dynamic tensile behavior of glass TRC has been studied. Tensile tests were performed under dynamic loading condition at three different strain rates 25, 50 and 100 s-1. The effect of the addition of short fibers on the dynamic response of TRC has been investigated. A Phantom v7 high speed

digital camera with sampling rate of 10,000 fps captured the cracking and failure behavior of the different composites. The camera was placed in front of the specimen observing its full size in between the grips, as shown in Figure 1.15**.** The images acquired have been analyzed using digital image correlation (DIC) technique to investigate strain response over the entire surface of the specimens.

4.2 Experimental Program

4.2.1 Materials and Processing

A finely grained matrix was used in mixing the textile-reinforced concrete which consisted of cement, fly ash, micro silica, and quartz sand. Table 4-1 summarizes the matrix composition. Superplasticizer with a basis of naphthalene-sulphonate was added in order to achieve sufficient flowability. The average slump flow value measured with a small cone (bottom diameter 100mm, top diameter 60mm, height 70mm) was 200mm.

Textile-reinforced concrete was produced with and without the addition of short glass fibres to the matrix. Polymer-coated biaxial fabric (see Figure 4.1) made of alkali-resistant glass (AR-glass) was used as reinforcement. The degree of reinforcement was calculated for one layer of fabric in volume as 66.33mm_2/m. In total 3 layers of fabric were applied. The fineness of the weft and warp threads as well as the mean spacing between the yarns are given in Table 4-1. The fineness is given in tex, which is equal to the weight of one kilometre of yarn in grams. Note that the spacing of the yarns is uniform in the warp direction while it is non-uniform in the weft direction (cf. **Figure 4.1**). Nevertheless, the mean yarn spacing is 7.4mm

in both directions. Dispersed AR-glass short fibres with an average diameter of 14_mand length of 6mmwere used as secondary reinforcement in a total volume fraction of 0.5%. These fibres disperse in water and are capable of being distributed in the mixture as single mono-filaments. The short glass fibres had a density of 2.68 g/cm$_3$, tensile strength of 1700MPa and Young's modulus of 72 GPa.

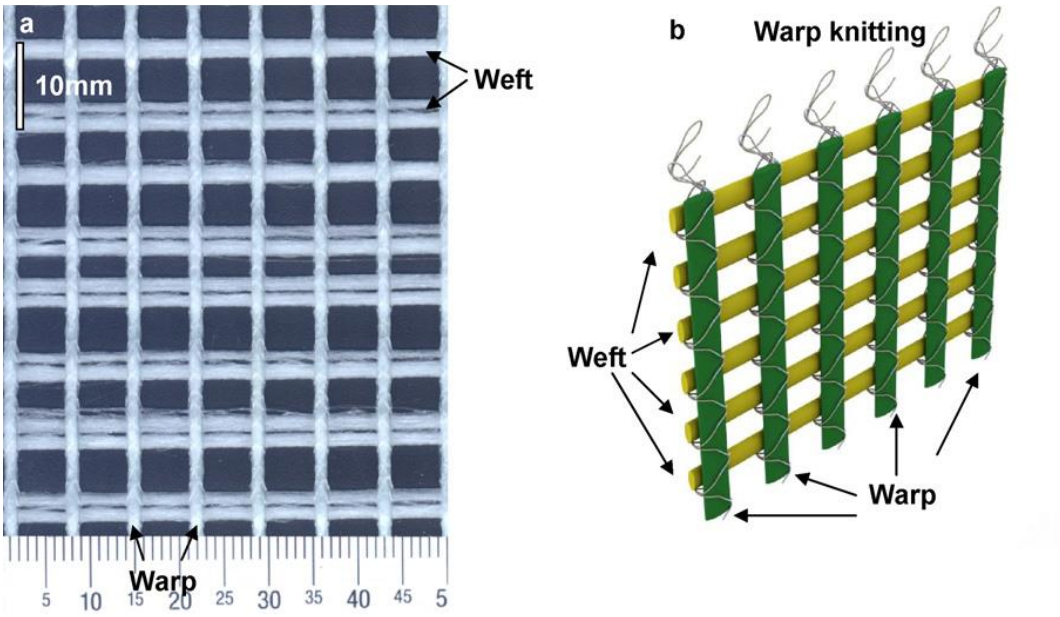

Figure 4.1 Biaxial textile reinforcement made of AR-glass: (a) photograph showing that the spacing between the yarns is uniform in the warp direction (with mean spacing of 7.4 mm), but not uniform in the weft direction and (b) sketch showing the details of the warp knitting.

Slender rectangular plates, 300 mm long and 50 mm wide, were cut from larger plates of length 525mm and width 425mm and were produced using a lamination technique. The laminating process started with the spreading of a thin concrete layer on the bottom of the mould. The first sheet of textile reinforcement was laid onto this fresh concrete layer and then, gently, partially pressed in and

smoothened. Complete embedment of the first textile layer took place during the application of the second concrete layer.

Table 4-1 Matrix composition (kg/m³).

Water-to-binder ratio	0.37
CEM III B 32.5 NW-HS-NA	632
Fly ash	265
Micro silica suspension*	101
Fine sand 0/1	947
Water	234
Superplasticizer	11

* solid : water = 50:50

Table 4-2 Textile properties.

NWM3-013-07-p2 (30%)			
Warp		Weft	
Fineness (tex)	Spacing (mm)	Fineness (tex)	Spacing (mm)
2*640	7.2	2*640	7.2

Subsequently these production steps were repeated until all three reinforcing layers were placed and incorporated into the finegrained concrete. The thickness of the plates was 10mm.

The plates were demoulded at the age of two days and stored in water until the age of 7 days. Subsequently, the plates were stored in a climate-controlled room at 20 °C and 65% RH until an age of 28 days.

4.2.2 High-speed tensile testing

The high-speed tensile tests were performed in a high-rate MTS testing machine. The setup and procedure of the dynamic tensile testing were addressed in Chapter 1[1.1]. The tension tests were performed at strain rates of 10, 25 and 50s^{-1}. Six specimens were tested for each strain rate.

Material parameters derived from the experimental data included tensile strength (peak stress), strain capacity (strain on reaching tensile strength) and work to fracture. Work to fracture was calculated using the total area under the stress-strain curve. Average value and standard deviation are given for each strain rate. Furthermore, tensile stress-strain curves of the specimens tested under static and dynamic conditions are compared.

Four different types of specimens including plain mortar, micro glass fiber reinforced concrete, textile reinforced concrete, and textile reinforced concrete with addition of micro fiber have been tested under high-speed tension loads at strain rates of 25 s^{-1}, 50 s^{-1}, and 100 s^{-1}(see Table 4-3). Results and parameters obtained from the experimental data include the stress-strain curves, Young's modulus, tensile strength (peak stress), strain capacity (strain at peak stress), and work-to-fracture. The work-to-fracture is evaluated using the total area under load vs. displacement curve. The reported results reflect both the average and standard

deviation values of each set tested. The high speed videos acquired by the phantom camera were used for image analysis to characterize the strain field.

Table 4-3 Testing matrix

Type	Mortar	Mortar+ micro fiber	TRC	TRC+ micro fiber
25 s^{-1}	x6	x6	x7	x6
50 s^{-1}	x5	x6	x7	x6
100 s^{-1}	x6	x4	x6	x6

4.2.3 Image analysis – digital image correlation (DIC) method

High speed videos were taken using a phantom camera, to be analyzed using DIC method. The setup of high speed camera, testing procedure, and discipline of DIC method were discussed in the first chapter [1.2].

4.3 Results, analysis and discussion

4.3.1 Effects of the addition of short fibers on plain mortar

Figure 4.2 Compares the representative stress-strain curves obtained from tensile testing under dynamic load on plain mortar specimens both with and without the addition of short glass fibers. The addition of short fiber was relatively low in this test series which is 0.5% by volume. The water-to-binder ratio of the matrix used was 0.30. As summarized by Table 4-4, with the addition of short fibers, the average tensile strengths of specimen slightly increased at strain rates 25 s^{-1} (from 4.71 MPa to 5.40 MPa) and 100 s^{-1} (2.66 MPa to 3.24 MPa), respectively. However, this parameter decreased from 3.30 MPa to 2.04 MPa when the strain rate was 50 s^{-1}. On the other hand, the work-to-fracture and strain capacity of the specimens were improved significantly by the addition of short fiber. The strain capacity rose from 1.06% to 3.44% (25 s^{-1}), 1.62% to 3.08% (50 s^{-1}), and 1.40% to 3.18% (100

s^{-1}), while the work-to-fracture increased from 0.36J to 0.51J, 0.45J to 0.59J and 0.28J to 1.01J, corresponding to three strain rates respectively. The improvements in ductility of the specimens can be traced back to the effect of lower w/b ratio on the quality of the fiber-matrix bond. The denser matrix with a w/b ratio of 0.30 contributes to a better bonding than the matrix with higher w/b ratio, reported by Barhum and Mechtcherine []. This means that the fibre embedded in the matrix can contribute to a great extent to the bearing of stress in the ascending branch of the stress – strain curve. The extent of this contribution, pointed out by Barhum and Mechtcherine, is not only limited by the tensile strength of the fiber (1,700 MPa for the glass fiber employed in this study), and the fibre content, but also depends on the distribution and orientation of short fibre. The concrete was likely to have more voids due to entrapped air, caused by the worse workability while content of short fibre is increased. It is more difficult to achieve an even fibre distribution over the volume of the matrix for a higher volume fraction of short fiber.

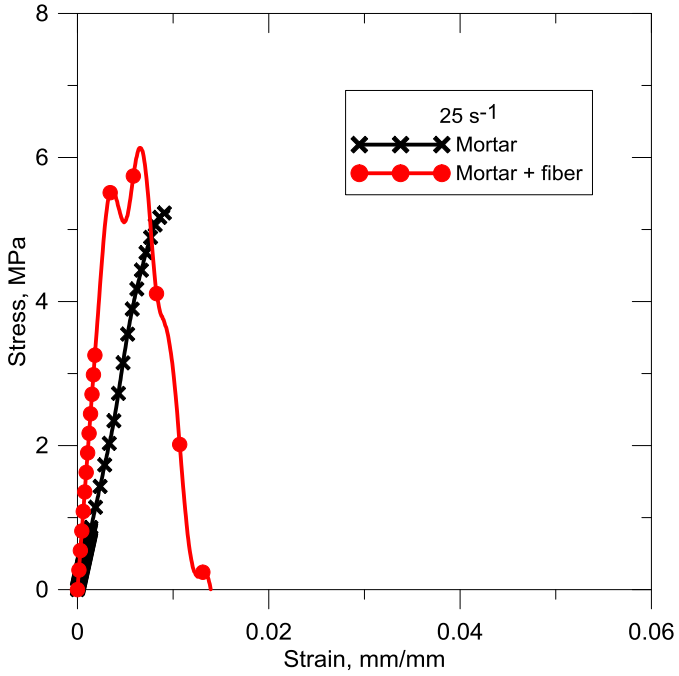
25 s-1
Mortar
Mortar + fiber
Stress, MPa
Strain, mm/mm
0
2
4
6
8
0
0.02
0.04
0.06

(a)

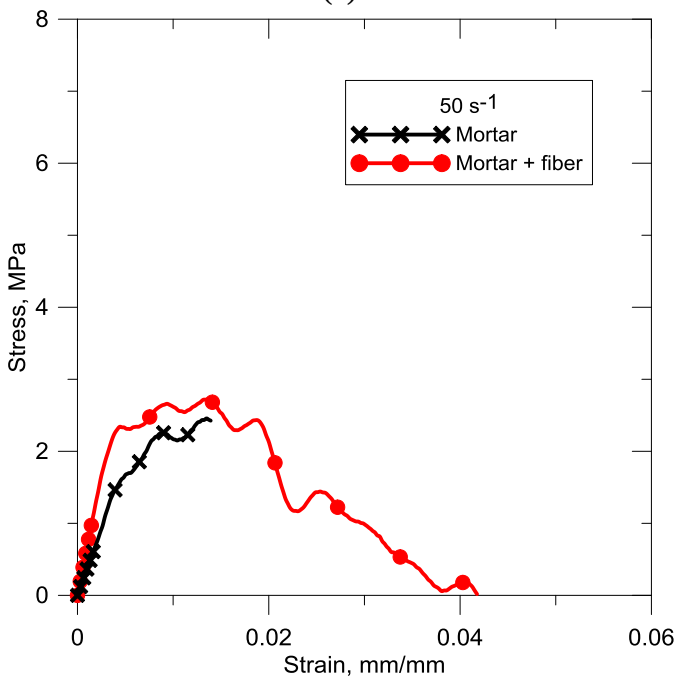
50 s-1
Mortar
Mortar + fiber
Stress, MPa
Strain, mm/mm
0
2
4
6
8
0
0.02
0.04
0.06

(b)

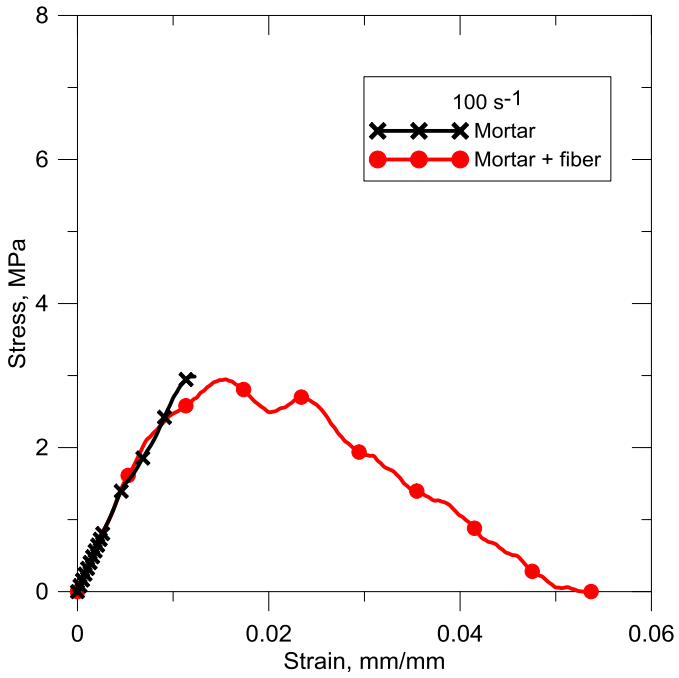

(c)

Figure 4.2 Stress-strain responses of plain mortar with and without the addition of short fibers at strain rates of (a) 25 s^{-1}, (b) 50 s^{-1}, and (a) 100 s^{-1}

4.3.2 Effects of the addition of short fibers on TRC behavior

Figure 4.6 shows the summarized stress-strain curves of TRC samples with and without short fibers, testing results and parameters are shown in Table 4-4. From a qualitative perspective, the addition of short fibers leads to slight increases in tensile strength and work-to-fracture and the stress at bend-over-point (BOP) at strain rats of 25 s^{-1} and 50 s^{-1}. The average tensile strengths of TRC at 25 s^{-1} (26.91 MPa) to and 50 s^{-1} (26.99 MPa) are almost same, while the work-to-fracture slightly increased from 19.28 J to 20.95 J. When the samples were tested at strain rate 50 s^{-1}, tensile strength increased from 31.42 MPa to 32.35 MPa, work-to-fracture from 14.77J to 19.01J. For the stresses at BOP, the improvements are 1.58 MPa and 1.09 MPa, respectively for the two cases.

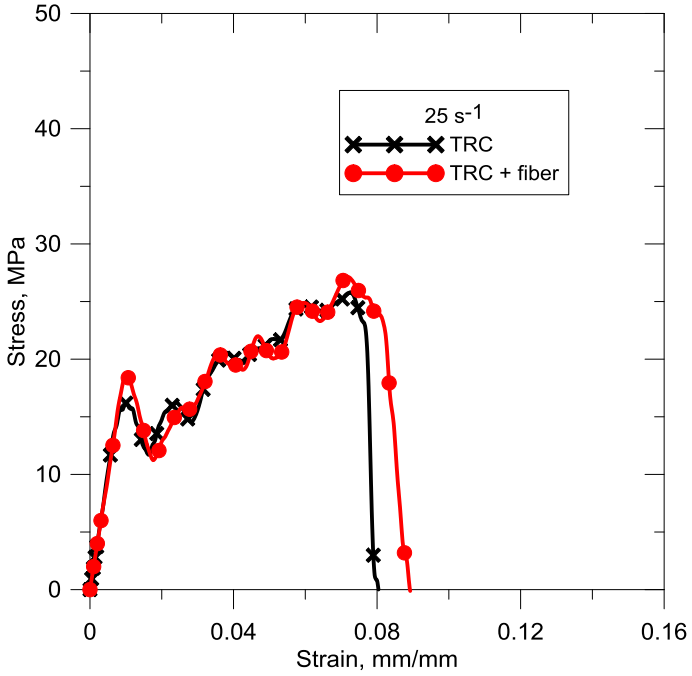
25 s-1
TRC
TRC + fiber
Stress, MPa
Strain, mm/mm
0
10
20
30
40
50
0
0.04
0.08
0.12
0.16

(a)

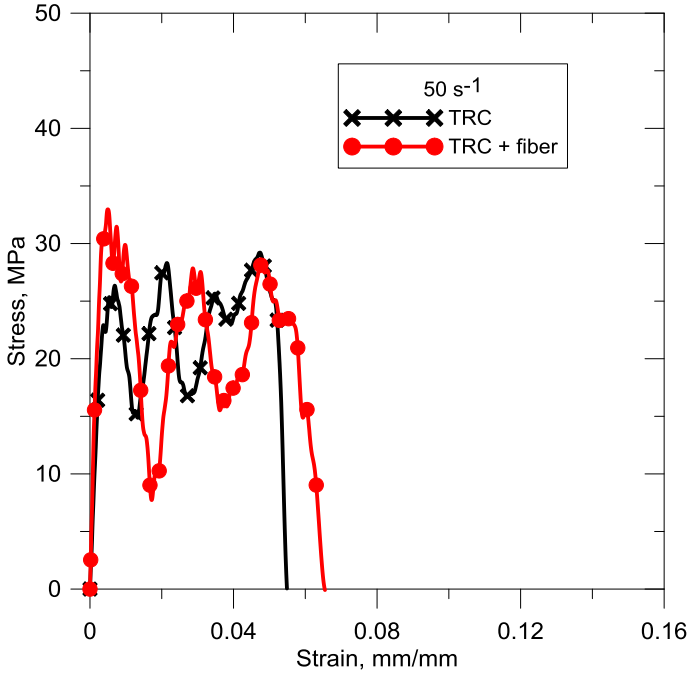
50 s-1
TRC
TRC + fiber
Stress, MPa
Strain, mm/mm
0
10
20
30
40
50
0
0.04
0.08
0.12
0.16

(b)

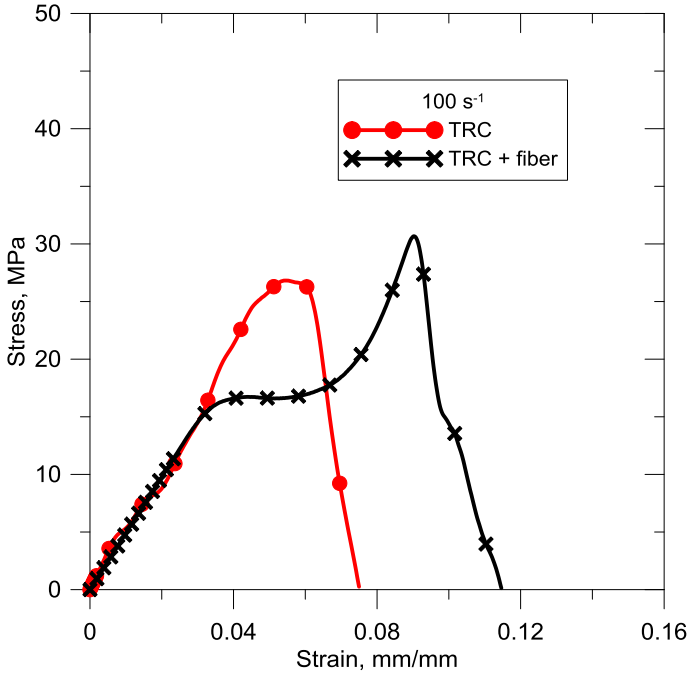

(c)

Figure 4.3 Stress-strain responses of TRC with and without the addition of short fibers at strain rates of (a) 25 s^{-1}, (b) 50 s^{-1}, and (a) 100 s^{-1}

However, for the highest strain rates in this test series, which is 100 s^{-1}, a decrease were observed for both tensile strengths (from 33.15 MPa to 25.42 MPa) and work-to-fracture (from 23.90J to 14.99J). This phenomenon of decreasing in both tensile strength and strain capacity agrees with the observations reported by Barhum and Mechtcherine [40].

4.3.3 Strain rate effects on mortar

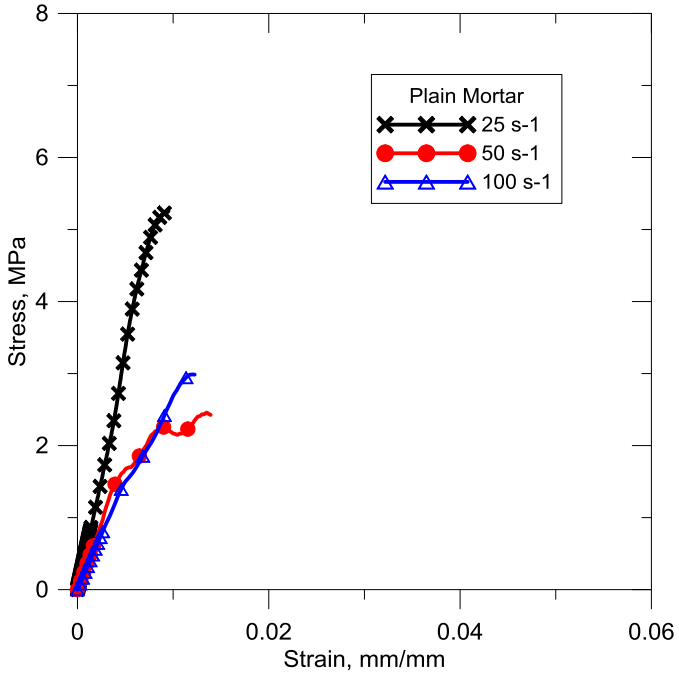
Plain Mortar
25 s-1
50 s-1
100 s-1
Stress, MPa
Strain, mm/mm
0
2
4
6
8
0
0.02
0.04
0.06

(a)

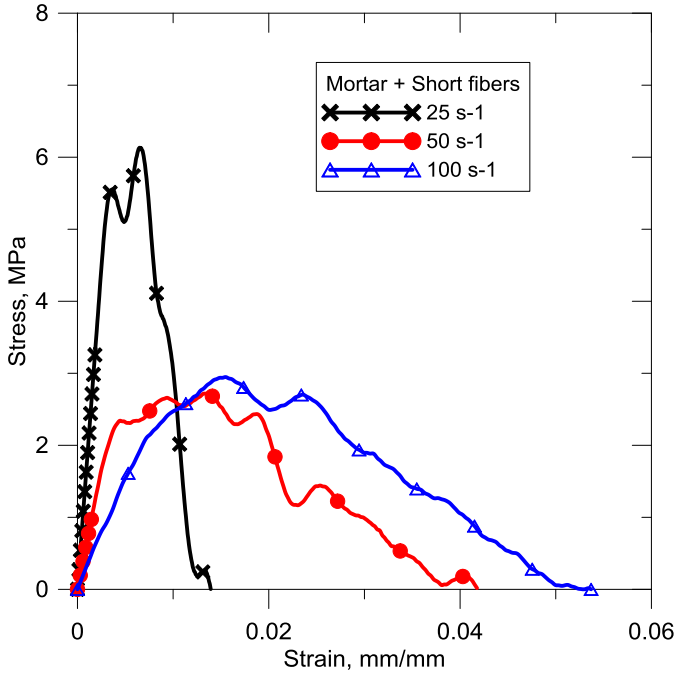
Mortar + Short fibers
25 s-1
50 s-1
100 s-1
Stress, MPa
Strain, mm/mm
0
2
4
6
8
0
0.02
0.04
0.06

(b)

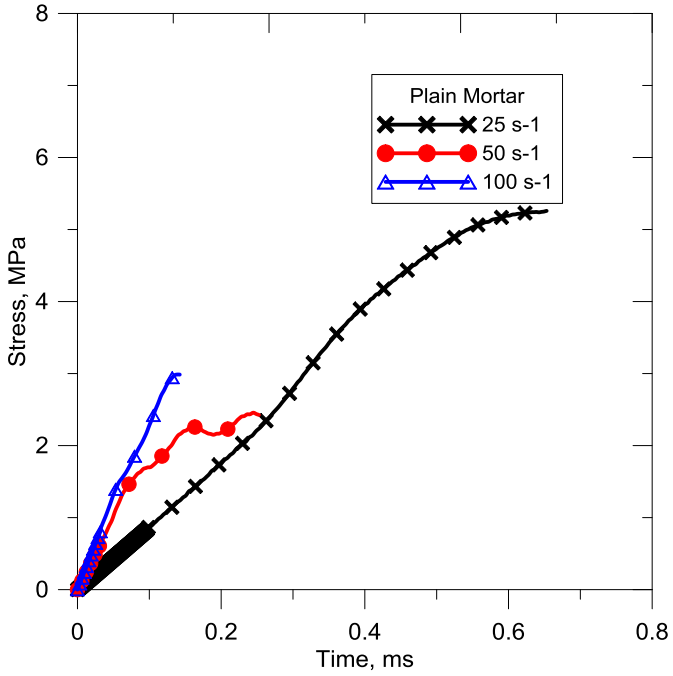

(c)

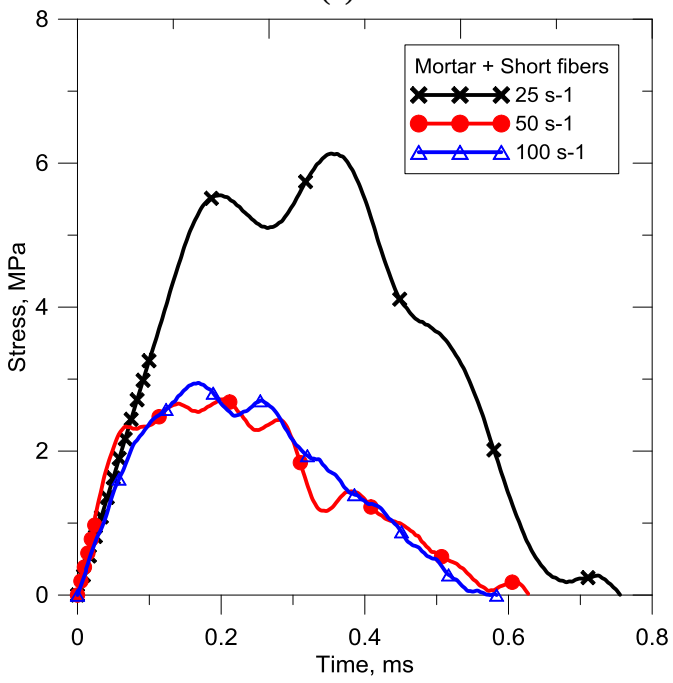

(d)

Figure 4.4 Tensile responses of plain mortar with and without short fibers under different testing strain rates: (a and c) plain mortar, (b) and (d) plain mortar + short fiber

Figure 4.4 compares the tensile responses of plain mortar with and without short fibers under dynamic loading with different strain rates. It can be observed that the average tensile strengths did not differ that much at from 50 s^{-1} to 100 s^{-1}, but found to be much higher when tested at 25 s^{-1}. This phenomenon can be attributed to the effect on testing response due to the system ring, pointed out by Xiao [46]. To address the specimen machine interaction, the testing system can be represented by a single-degree freedom under-damped spring-mass system as developed Xiao the response of which can be obtained when the impulse velocity, damping ratio, and natural frequencies are known. All the tests were conducted with an actuator velocity of approximately 1 m/s. The modal analysis showed that the natural frequencies of the testing system were 900, 1400, 1600 Hz and the damping ratio is about 0.02. Based on these parameters, the effect of system ringing at frequencies of 900, 1400, 1600 Hz on stress level was calculated for the carbon fabric – cement and AR glass fabric – cement composites, the system was excited by a sudden velocity change of 1 m/s, as shown in Figure 4.5**.** One should notice that for the system ringing at 0.9 kHz, the maximum stresses were about 3.5 MPa and 7 MPa for AR glass and carbon composite, respectively, at 0.25 ms and the ringing effect became negligible after 0.5 ms. For the system ringing at 1.6 kHz, the response first increased with time, peaked at about 0.15 ms, and then decreased. The maximum stresses were about 2 MPa and 4 MPa for AR glass and carbon composites, respectively. The ringing effect became negligible after 0.3 ms. This analysis reveals that the natural frequency of the testing system affects the test results in high rate testing by contributing to the magnitude of the system ringing.

When tested at 50 s^{-1} and 100 s^{-1}, the stresses reaches peak at about 0.2 ms before the ringing effect takes into place. But for the strain rate 25 s^{-1}, the test duration was about 0.8 ms and even longer which allows the system ringing to dominate the response in the loading process. The stress oscillation in Figure 4.4 is the coupled result of specimen failure and system ringing.

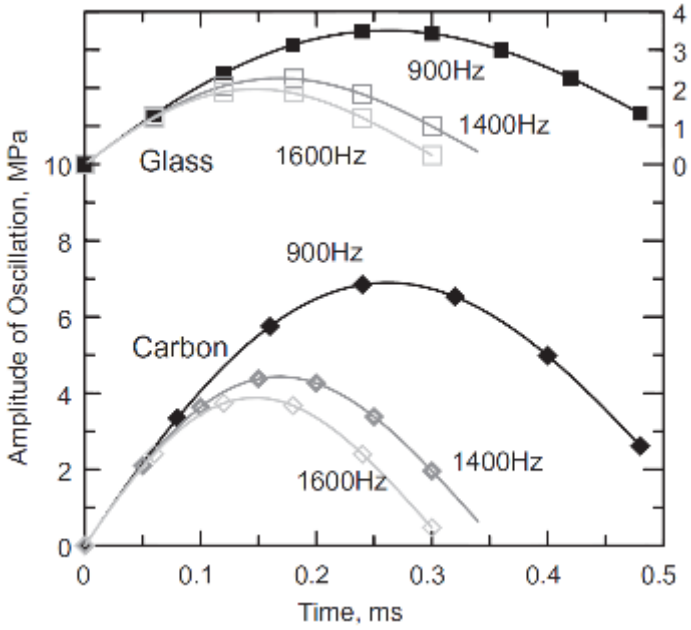

Figure 4.5 The effect of system ringing at frequencies of 900, 1400, 1600 Hz on stress level in carbon and AR glass composites. The system was excited by a sudden velocity change of 1m/s [84].

4.3.4 Strain rate effects on TRC

Figure 4.6 represents the effects of strain rates on TRC samples with and without short fibers. It is observed that the average tensile strength and σ_{BOP} of TRC samples with and without short fibers increased with the increasing strain rate up to 50 s-1. The average tensile strength of TRC rose from 26.91 MPa to 31.42 MPa, and 26.99 MPa to 32.35 MPa with addition of short fibers. Significantly increases

in σBOP were observed for both two cases, where the factor of increasing is about 1.6. However, both strain capacity and work-to-fracture reduced as the strain rate increased. The strain capacity decreased from 6.79% to 4.52% for TRC, and 6.66% to 5.99% for TRC with short fibers. While the work-to-fracture for TRC decreased from 19.28J to 14.77J with a loss of 31%. Nevertheless, the loss of work-to-fracture is found to be much smaller after the short fibers added, which slightly decreased from 20.95J to 19.01J. This can be attributed to the contribution of short fiber to the post-peak responses, that the post peak stresses were maintained at a relatively higher level compared to that of TRC samples without short fibers, which can be seen in Figure 4.6a and b. As a result, even though the strain capacity dropped dramatically, the area under the curve does not reduce a lot because the high level of post peak stresses.

However, these trends somehow changed when the strain rate increased to 100 s-1. First of all, the shapes of the curves differ significantly to those obtained at lower strain rates. Obvious oscillations of the system at its natural frequency were observed for specimens tested at 25 s-1 and 50 s-1 attributed to the interaction between specimen and machine. These oscillations decreased as the strain rate increased to 100 s-1, as shown in Figure 4.6a and b, which ends up leading to a different shape of stress-strain curve. Second difference is found to be the steep increase in strain capacity for TRC without short fibers when the strain rate is 100 s-1, from 4.52% to 10.62%. At the same time, a stage where the load stays but strain keeps increasing can be seen on the stress-strain curve, which contributes the most to the large strain capacity. This can be attributed to the pull out displacement

between fibers and matrix after the first macro crack formed, which was also included in the displacement acquired in the data. Moreover, according to the study of rate effects on fiber pull-out tests conducted by Boshoff et. al [95], the pull-out displacement at peak loads increased more than 100% when the pull-out rates rose from 0.01 mm/s to 100 mm/s. This effect can be caused by the higher inertia force generated by the acceleration of the actuator, and a higher acceleration is needed to excite higher strain rate, which results in a larger pull-out displacement. Nevertheless, this phenomenon disappeared with the addition of short fibers, as Figure 4.6b shows, which indicates the contribution to enhancing the entire bonding mechanism between fiber and matrix. In addition, the average tensile strengths dropped from 32.35 MPa to 25.42 MPa while the work-to-fracture decreased from 19.01J to 14.99 J as the strain rate rose up from 50 s^{-1} to 100 s^{-1}. The reduction of work-to-fracture can be traced back to the drop in strain capacity. The reason of the increase and decrease of average strength as the strain rates increase is not clear. A possible explanation could be the interaction between specimens and system, that the oscillation is observed to affect the shape of stress-strain curves mostly at 50 s^{-1}, as shown in Figure 4.6d. Moreover, the BOP was reached at about 0.1 ms followed by a series of vibrations and then leaded a steep drop at 0.4 ms As discussed before, the system ringing dominates the response within the time range from 0.1 ms to 0.3 ms for a system with a natural frequency of 1600 Hz, see Figure 4.5. An interesting finding is that the peak stresses happened to be the stresses at BOP, when the response is dominated by system ringing. While in contrast to it, the peak stresses of the specimens tested at 25 s^{-1} and 100 s^{-1} took place around 0.5 ms and 4.4 ms,

respectively, when the effect of system ring is negligible. Thus the effect of system ringing need to be taken into consideration when comparing the average strength at different strain rates. However, when it comes to the TRC specimens, the time when peak stresses were reached for all the strain rates are found to be out of the range when system ringing affects, which are 4.4 ms, 2.6 ms and 1.3 ms, respectively. Based on the discussions, authors would predict that the TRC with addition of short fibers is not that sensitive to strain rates.

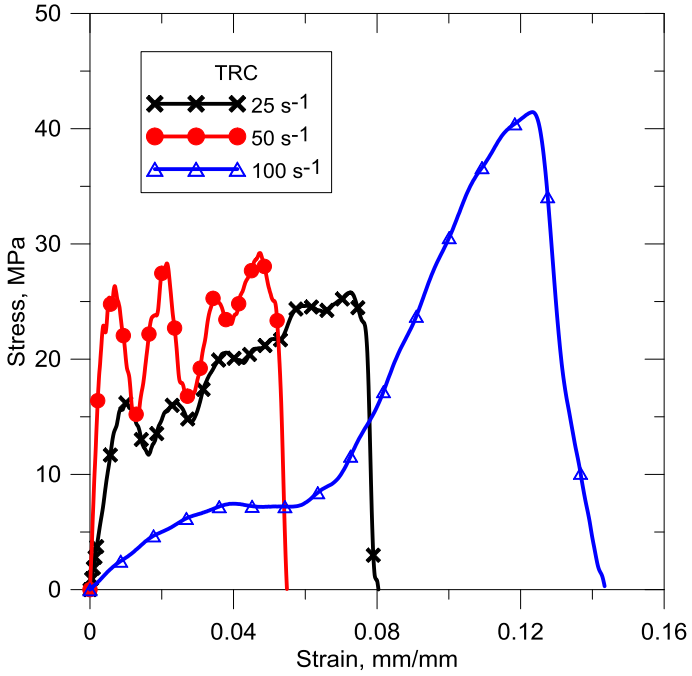
TRC
25 s-1
50 s-1
100 s-1
Stress, MPa
Strain, mm/mm
0
10
20
30
40
50
0
0.04
0.08
0.12
0.16

(a)

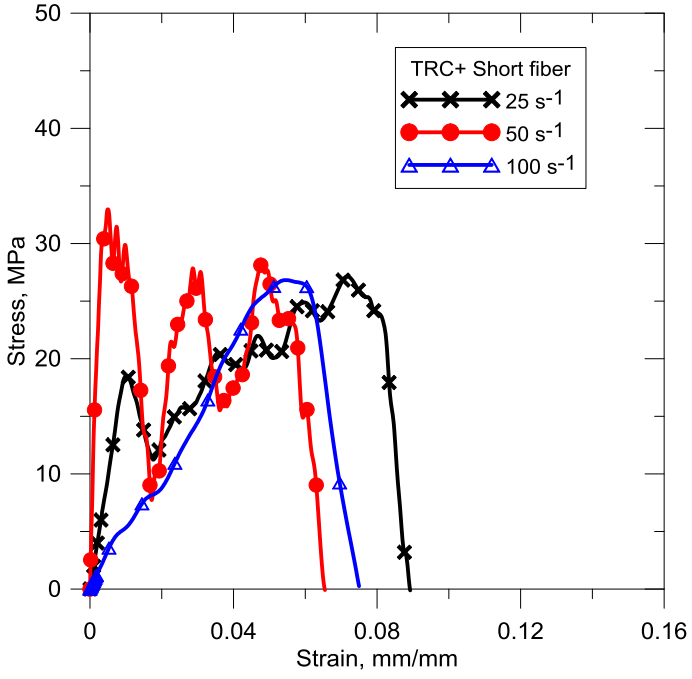
TRC+ Short fiber
25 s-1
50 s-1
100 s-1
Stress, MPa
Strain, mm/mm
0
10
20
30
40
50
0
0.04
0.08
0.12
0.16

(b)

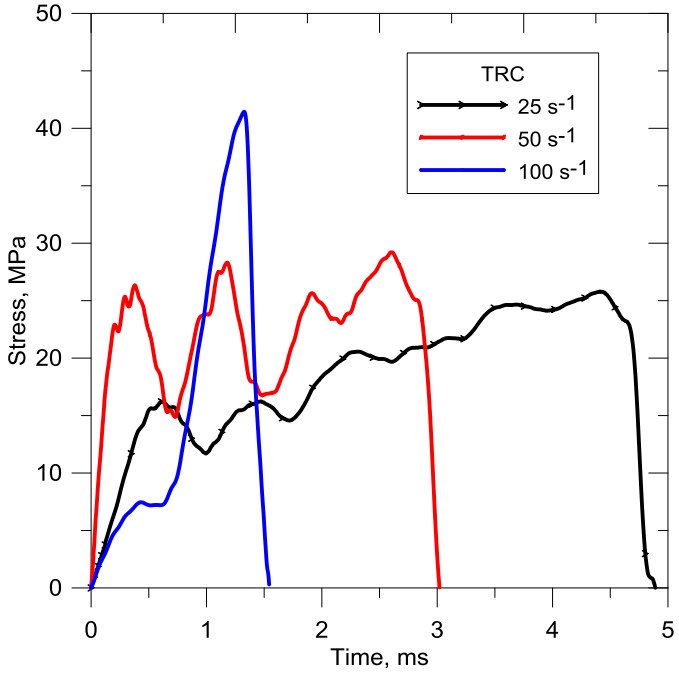

(c)

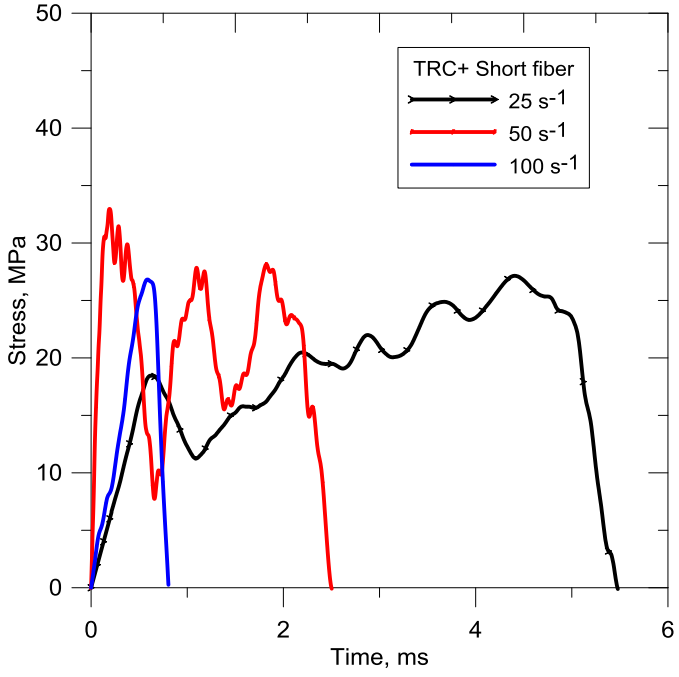

(d)

Figure 4.6 Tensile responses of plain mortar with and without short fibers under different testing strain rates: (a and c) TRC, (b) and (d) TRC + short fiber

4.3.5 Failure modes

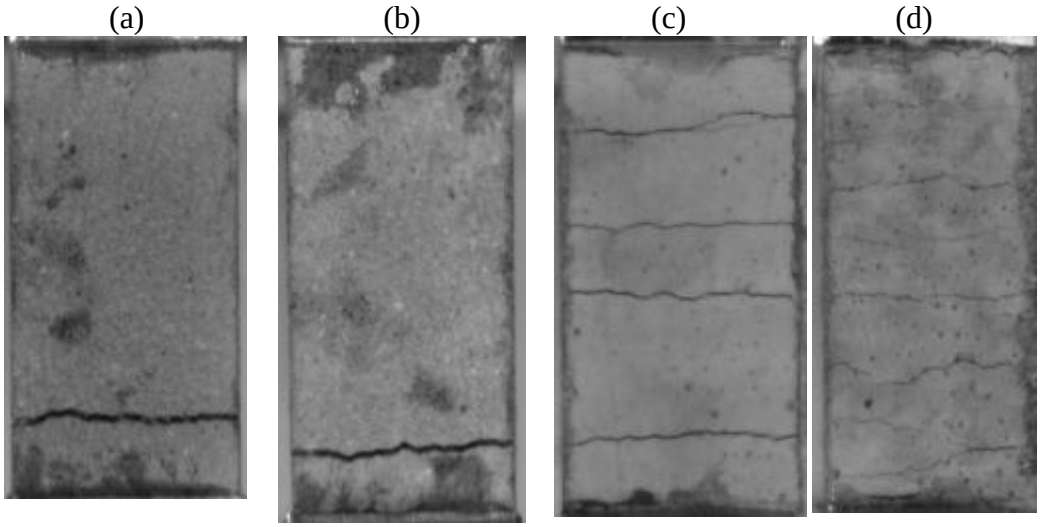

Figure 4.7 Failure modes of (a) Plain mortar, (b) Plain mortar with micro fiber, (c) TRC and (d) TRC with micro fiber

Figure 4.7 compares the failure modes (crack pattern) of the four types of specimens obtained by the high speed camera: Plain mortar, plain mortar with short fiber, TRC, and TRC with short fiber. When the plain mortar specimens were subjected to direct tension, only one macro crack formed followed by the failure of samples, which is attributed to the brittleness of the material. While with the addition of short fibers, specimens yielded to the same failure mode with that of plain mortar, which can be traced back to the low volume fraction (0.5%). Multiple macro cracks were formed when it comes to TRC samples, showing an obvious change in failure mode. Additionally, when short fibers were added to TRC, more finer cracks were propagated compared to that of TRC. The type of short fibres used mitigated cracking and bridged the small cracks, thus enabling a finer crack pattern and smaller crack widths when compared to TRC without short fibres. This behaviour can be attributed, to the higher stress levels reached in the specimens

with short fibres, which even prior to the development of the first macro-crack, lead to the formation of a greater number of micro-cracks over the entire specimen volume or length. In the present work micro-cracks are defined as short, very fine and not interconnected cracks which do not lead to a considerable decrease in stiffness or stress carrying capacity of the matrix. A macro-crack is defined as such if it is continuous and spread over a considerable part of the specimen cross-section leading to a considerable decrease in stiffness and stress transfer across the crack. Beginning from the first-crack stress, these micro-cracks grow to develop the macro-cracks. A greater number of finely distributed micro-cracks offer more nuclei for macro-crack formation, thus leading to more pronounced multiple cracking. On the other hand, as amacro-crack form, the matrix stress in its vicinity decreases. Depending on the type and interface properties of the used reinforcement, the next crack may not form within a distance corresponding to a threshold value. The addition of short fibres causes an additional stress transfer over the macro-cracks, which results in a less pronounced relaxation of the matrix in the vicinity of the cracks. A new crack can form at a smaller distance from an existing one; hence, more pronounced multiple cracking can be observed. So far the picture is clear. The short fibres bridging mechanism can lead to a non-uniform widening of the formed macro-cracks, which has still to be shown by precise measurements of crack opening history. However, depending on the orientation of short fibres, volume fraction and local bond properties, several cracks may be bridged in such an efficient manner that little or no macro-crack opening occurs. Consequently, with the increasing strain on the specimen, crack widening is located mainly at scattered

macrocracks which are less efficiently bridged by the short fibres. After these cracks exceed a specific opening, the load across them is transferred only by the textile reinforcement.

Table 4-4 Testing results of plain mortar with and without short fibers obtained from dynamic tensile testing subjected different strain rates

Material	Strain Rate	NO.	Tensile Strength	Young's Modulus (Gpa)	Strain capacity	Work-to-fracture (J)
Plain Mortar	25	1	3.6629	0.4767	0.0079	0.2041
		3	5.2603	0.5934	0.0144	0.4001
		4	5.2163	0.4143	0.0096	0.4868
		AVG.	4.7132	0.4948	0.0106	0.3637
		STD. DEV	0.7429	0.0742	0.0027	0.1183
	50	1	2.4667	0.3494	0.0132	0.3013
		2	5.1653	0.3293	0.0208	0.8025
		4	2.2747	0.1983	0.0145	0.2570
		AVG.	3.3022	0.2923	0.0162	0.4536
		STD. DEV	1.3197	0.0670	0.0033	0.2474
	100	1	2.2121	0.1459	0.0158	0.2461
		2	2.7692	0.2853	0.0142	0.3204
		5	2.9871	0.3195	0.0121	0.2657
		AVG.	2.6561	0.2502	0.0140	0.2774
		STD. DEV	0.3263	0.0751	0.0015	0.0314
Plain Mortar+ short fibers	25	3	4.4429	0.9424	0.0194	0.4756
		4	5.6228	1.2465	0.0492	0.4539
		6	6.1326	1.7459	0.0346	0.5879
		AVG.	5.3994	1.3116	0.0344	0.5058
		STD. DEV	0.7077	0.3312	0.0122	0.0587
	50	3	1.7416	0.2507	0.0244	0.3879
		5	2.7215	0.8839	0.0454	0.7654
		8	1.6655	0.1968	0.0226	0.6198
		AVG.	2.0429	0.4438	0.0308	0.5910
		STD. DEV	0.4809	0.3120	0.0103	0.1555
	100	1	4.8432	0.7957	0.022	1.1739
		2	1.9431	0.3289	0.0572	0.8001
		4	2.9477	0.303	0.0163	1.0678
		AVG.	3.2447	0.4759	0.0318	1.0139
		STD. DEV	1.2024	0.2264	0.0181	0.1573

Table 4-5 Testing results of TRC with and without short fibers obtained from dynamic tensile testing subjected different strain rates

Material	Strain Rate	NO.	Tensile Strength	σ_{BOP+}	Strain BOP+	Young's Modulus (Gpa)	Post-cracking stiffness (MPa)	Strain capacity	Work-to-fracture (J)
TRC	25	1	25.53	21.19	0.01	2.08	117.55	0.07	18.61
		4	25.68	16.21	0.01	2.04	213.40	0.07	19.30
		5	29.50	18.31	0.01	1.84	237.42	0.06	19.92
		AVG.	26.91	18.57	0.01	1.99	189.46	0.07	19.28
		STD. DEV	1.84	2.04	0.00	0.11	51.78	0.00	0.54
	50	1	33.72	32.29	0.01	7.66		0.04	14.27
		2	29.13	30.30	0.01	7.74		0.05	15.81
		5	31.43	26.03	0.01	8.13		0.05	14.24
		AVG.	31.42	29.54	0.01	7.84		0.05	14.77
		STD. DEV	1.87	2.61	0.00	0.20		0.00	0.73
	100	1	41.40	7.44	0.04			0.12	28.17
		2	31.00	17.03	0.05			0.09	20.90
		3	27.06	16.49	0.05			0.10	22.64
		AVG.	33.15	13.65	0.05			0.11	23.90
		STD. DEV	6.05	4.40	0.01			0.01	3.10
TRC+ short fibers	25	2	23.71	19.31	0.01	2.03	817.88	0.07	17.29
		3	30.15	22.60	0.01	1.91	899.12	0.06	24.57
		5	27.10	18.53	0.01	1.95	1038.38	0.07	20.99
		AVG.	26.99	20.15	0.01	1.97	918.46	0.07	20.95
		STD. DEV	2.63	1.76	0.00	0.05	91.05	0.00	2.97
	50	2	32.96	32.92	0.01	11.46		0.05	16.35
		3	36.99	31.92	0.00	10.59		0.07	23.94
		5	27.09	27.05	0.00	16.72		0.06	16.73
		AVG.	32.35	30.63	0.00	12.92		0.06	19.01
		STD. DEV	4.06	2.56	0.00	2.71		0.01	3.49
	100	1	26.93					0.05	14.81
		4	23.08					0.05	15.57
		5	26.25					0.06	14.59
			25.42					0.05	14.99
			1.68					0.01	0.42

4.3.6 Image analysis

The strain field of plain mortar specimens with and without fibers generated by the digital image correlation method is presented in Figure 4.8. As discussed in the previous section – failure modes, one macro crack was formed which leads to a failure of brittle. On the other hand, the formation of macro crack is attributed to highly stress concentration, which is required to store enough energy to create new surfaces, from the perspective of fracture mechanics. And this phenomenon of concentration was detected by DIC method, see Figure 4.8. According to the legend of the contour map, red color stands for maximum strain value while purple is the minimum, in this case, given the value of 0. Two bands in red can be seen on the deformed images on each side of the crack, followed by a gradually changed color path from yellow to blue. While the deformation of over rest area of the specimen appears to be extremely small that cannot be detected effectively. The concentration of axial strains refers to the concentration of stresses which is straightforward. However, it is difficulty to generate the stress field from perspective of quantification, due to several reasons including the non-homogeneity material, changing in material properties with formation of cracks, etc. Even so, the overall strain field was clearly observed and general stress distribution can be described.

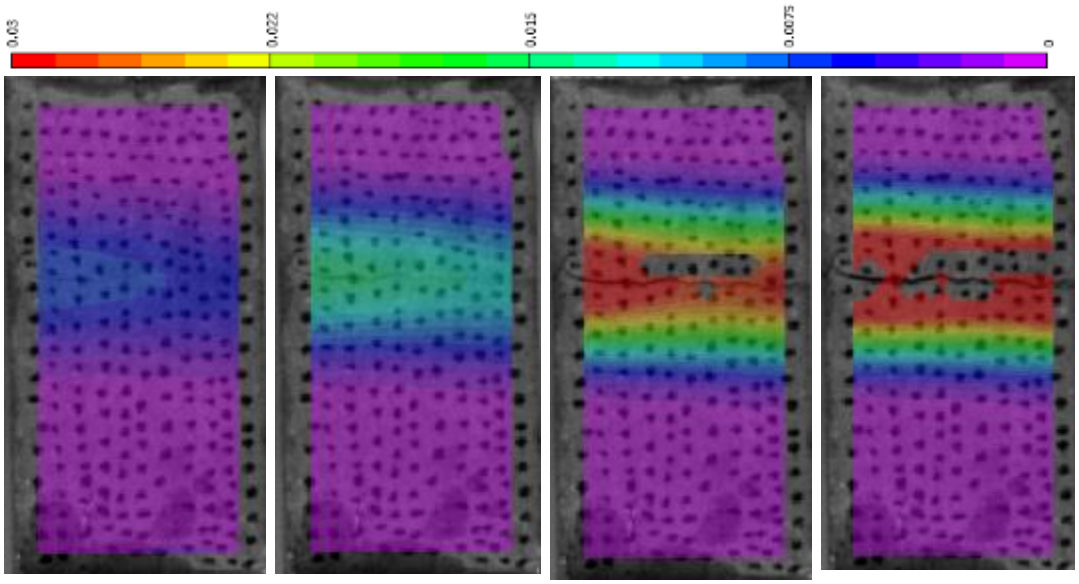

T = 0.1 ms T = 0.2 ms T = 0.4 ms T = 0.5 ms

(a)

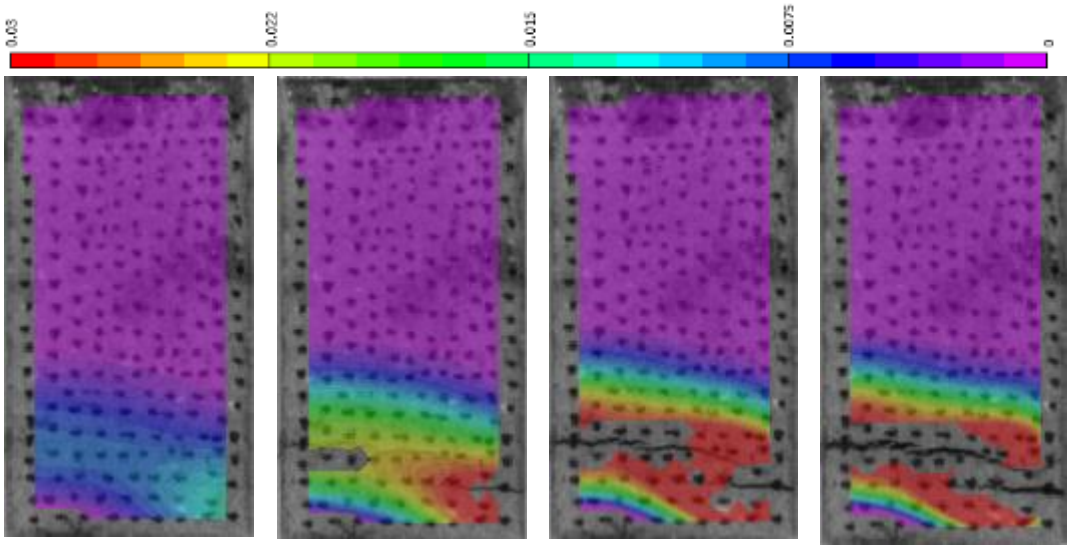

T = 0.1 ms T = 0.2 ms T = 0.3ms T = 0.4 ms

(b)

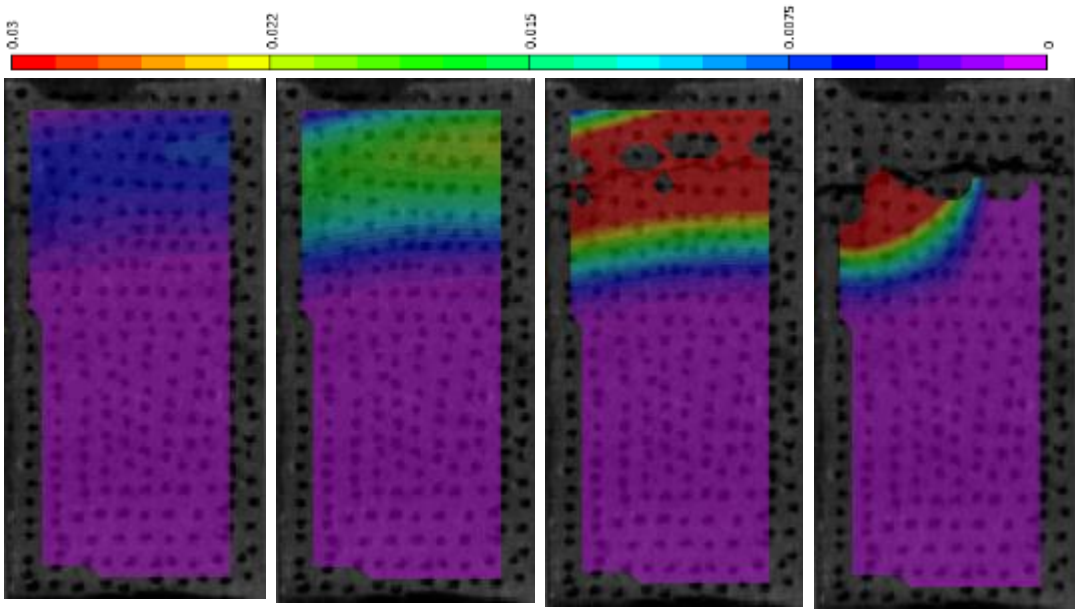

T = 0.1 ms T = 0.2 ms T = 0.3ms T = 0.4 ms

(c)

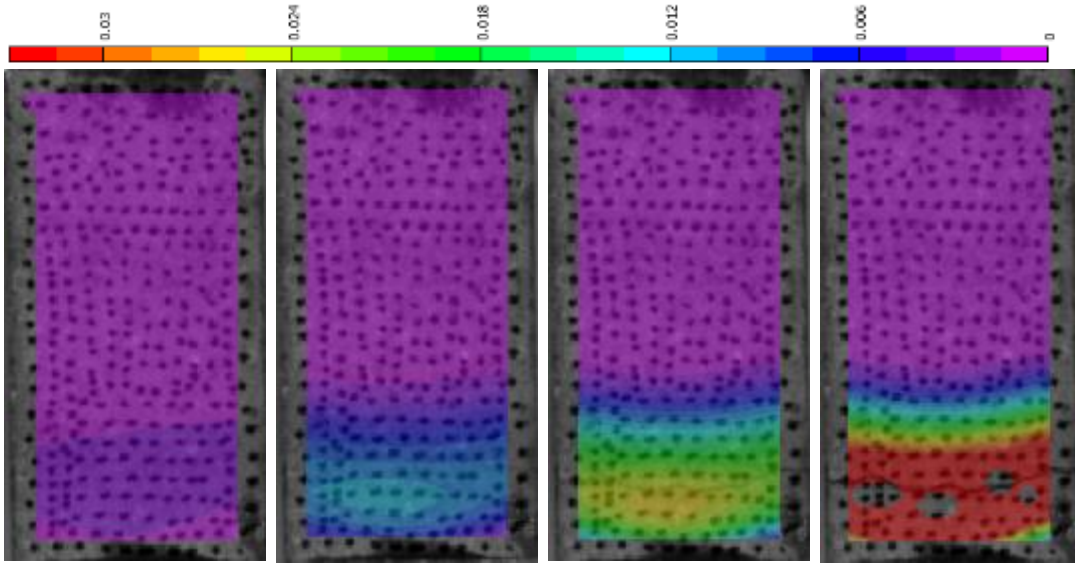

T = 0.1 ms T = 0.2 ms T = 0.3 ms T = 0.4 ms

(d)

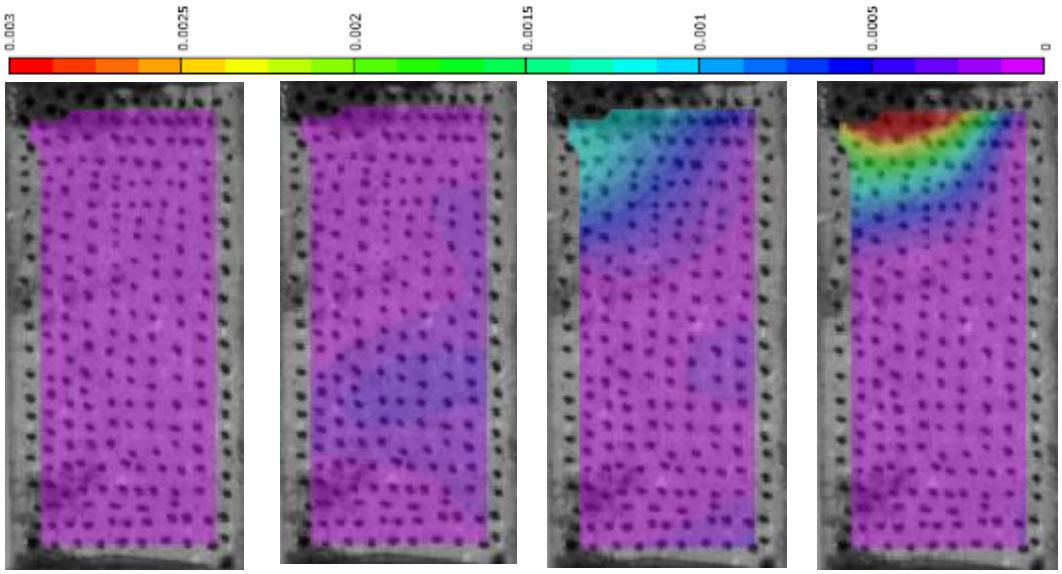

T = 0 T = 0.1 ms T = 0.2 ms T = 0.3 ms

(e)

Figure 4.8 Strain field (axial strain) obtained by DIC method for plain mortar specimens with and without short fibers tested at different strain rates: Plain mortar at (a) 25 s^{-1}, (b) 50 s^{-1}, (c) 100 s^{-1}, and mortar + fiber at (d) 25 s^{-1}, (e) 50 s^{-1}.

Figure 4.9 shows the strain filed of TRC samples with and without short fibers, tested at different strain rates. First of all, similar to mortar, intense concentration of strain took place close to cracks distributed over the specimen, see Figure 4.8a and c, which again, indicates the concentration of stress. However, the area of concentration is relatively larger than that of mortar specimen, which is attributed to the formation of multiple cracks instead of one. This phenomenon confirms well with the comparison of failure modes of composites before and after reinforced by TRC. Secondly, due to the existing of textile fabrics, the distribution of stress turns out to be more widely compared to plain mortar with and without short fibers. As can be seen in the figure, most area on the surface of specimens are in color of green, standing for strains from 1.5% to 3% according to the legend of

each set. While with respect to mortar specimens, most of them are in purple, i.e. zero strain, which means the potential properties of concrete were not utilized. The difference of strain distribution, directly related to stress distribution, implies the enhancement in overall strengthening and bonding, on the other word, behavior of tension stiffening, provided by textile fabrics.

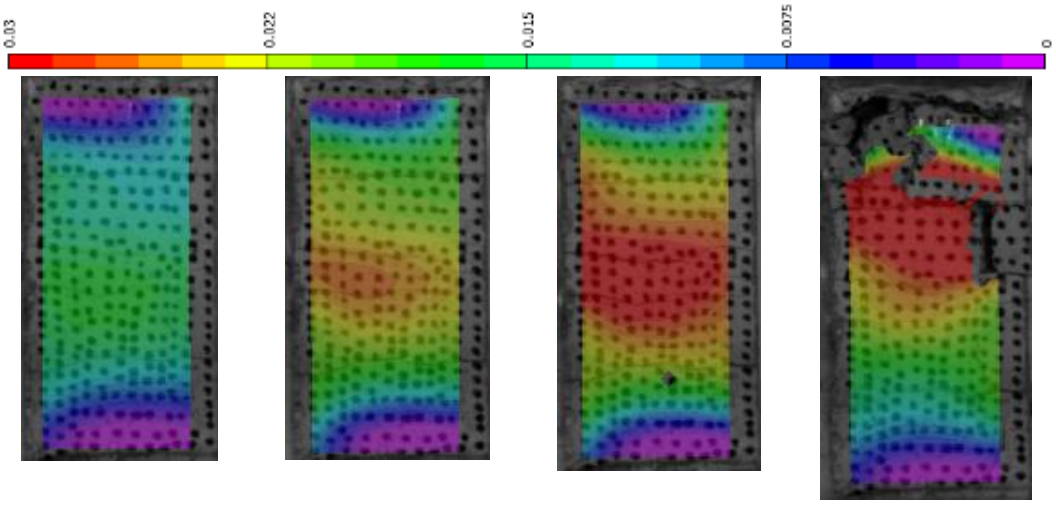

T = 1 ms T = 2 ms T = 3 ms T = 4 ms

(a)

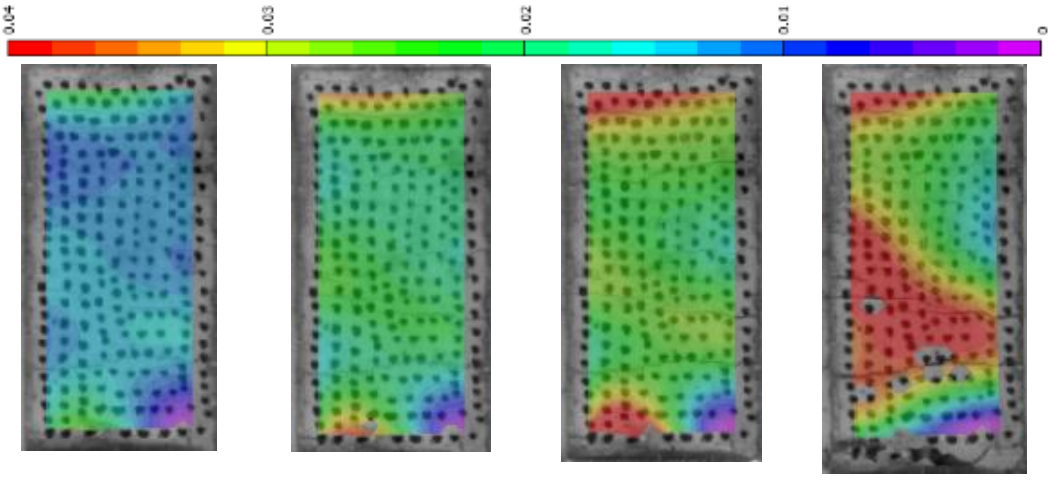

T = 0.5 ms T = 1 ms T = 2 ms T = 3 ms

(b)

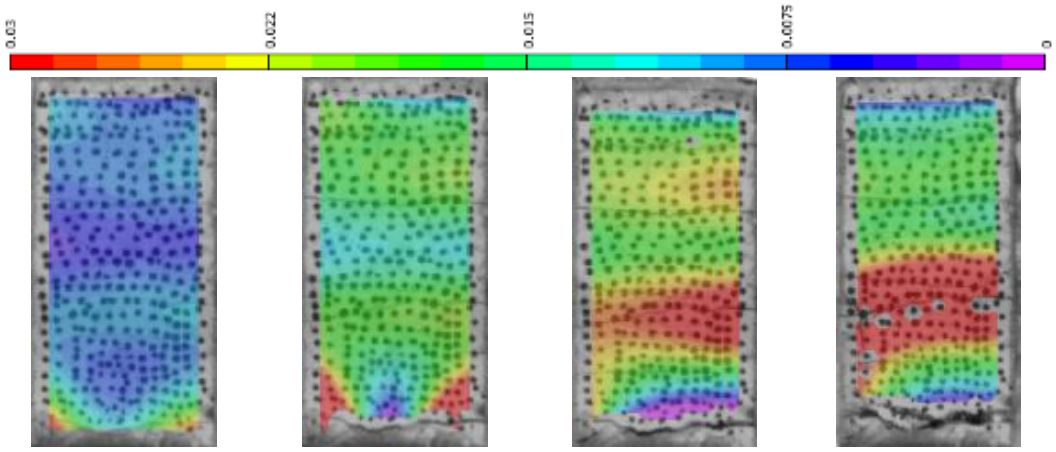

T = 0.2 ms T = 0.4 ms T = 0.6 ms T = 0.8 ms

(c)

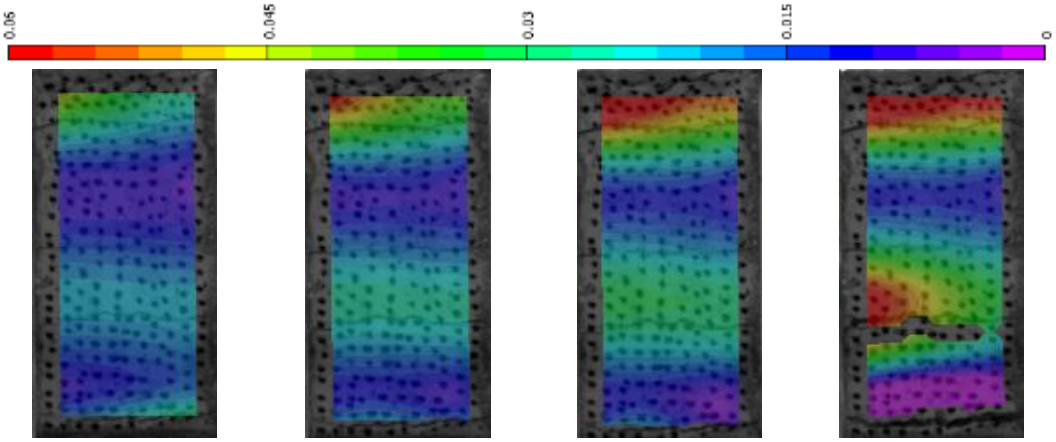

T = 2 ms T = 3 ms T = 4 ms T = 5 ms

(d)

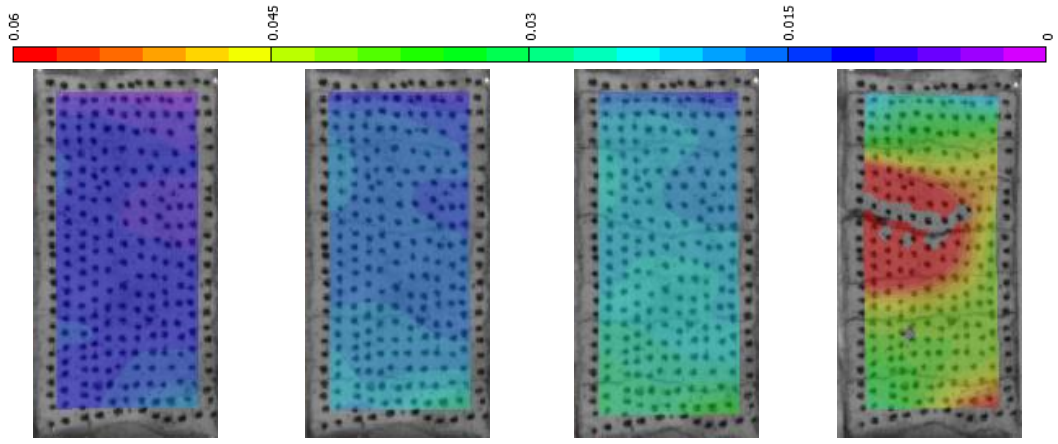

T = 1 ms T = 2 ms T = 3 ms T = 4 ms

(e)

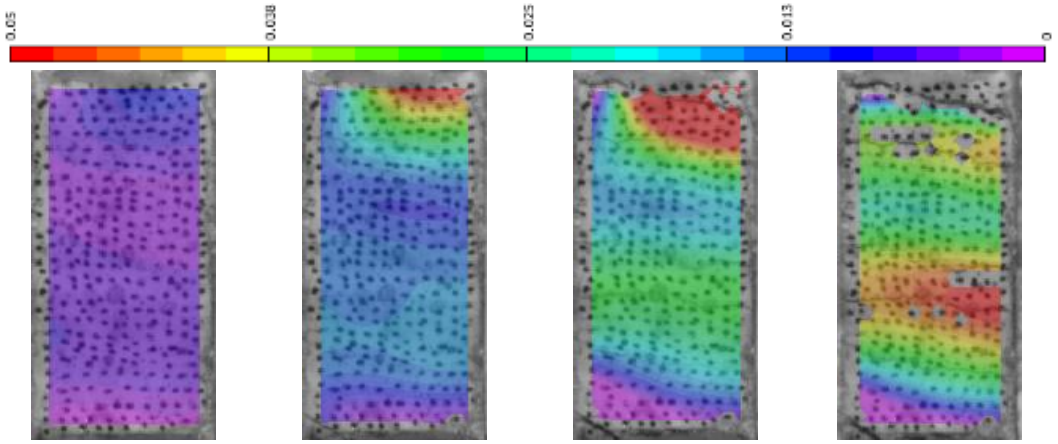

T = 0.2 ms T = 0.4 ms T = 0.6ms T = 0.8 ms

(f)

Figure 4.9 Strain field (axial strain) obtained by DIC method for plain mortar specimens with and without short fibers tested at different strain rates: TRC at (a) 25 s-1, (b) 50 s-1, (c) 100 s-1, and TRC + fiber at (d) 25 s-1, (e) 50 s-1, (f) 100 s-1.

4.4 Conclusions

High speed tests of four types of specimens were performed at three nominal strain rates of 25 s^{-1}, 50 s^{-1}, and 100 s^{-1} using a servo-hydraulic testing machine. Image analysis based on digital image correlation (DIC) method was

conducted to further study the failure modes. Following conclusions can be drawn from the present work:

For tensile tests performed up to 50 s^{-1}, an increase in tensile strength and stress and bend-over-point (BOP), and decrease in strain capacity and work-to-fracture were observed for TRC samples. However, this trend was changed when the strain rates increased to 100 s^{-1}, effected by system vibrations at different strain rates. Large pull-out displacement between fibers and matrix was observed at the highest strain rates, which results in an increase in strain capacity and work-to-fracture. But the trend of increasing in tensile strength was still verified.

The addition of short fibers brought the σ_{BOP} and work-to-fracture up for TRC specimens, while showing no obvious effect on tensile strength. Moreover, the modes of failure became more ductile since the short fibers bridging over micro cracks. With respect to the effect of strain rates, TRC with short fibers did not show a firm trend as the strain rates increased.

DIC was a powerful tool to determine the strain field in cement composites. The analysis results on different types of specimens clearly showed the contribution to the post-peak responses with the addition of textile fabrics, by identifying the effect and location of strain concentration and overall distribution.

References

[1] Post, D. Moiré Interferometry at VPI and SU. ExperimentalMechanics, 1983, 23(2), 203-210.

[2] Fottenburg, W. G. Some Applications of Holographic Interferometry. Experimental Mechanics, 1969, 8, 281-285.

[3] Wang, Y. Y., Chen, D. J. and Chiang, F. P. Material testing by computer aided speckle interferometry. Experimental Techniques, 1993, 17(5), 30-32.

[4] Po-Chih Hung and A. S. Voloshin, (2003), "In-plane strain measurement by digital image correlation", J. Braz. Soc. Mech. Sci. & Eng. vol.25 no.3 Rio de Janeiro July/Sept. 2003.

[5] Bastawros, A. F. and Voloshin, A. S. Thermal Strain Measurements in Electronic Packages through Fractional Fringe Moiré Interferometry. Journal of Electronic Packaging, 1990, 112(4), 303-308.

[6] Sutton, M. A., Wolters, W. J., Peters, W. H., Ranson, W. F. and McNeil, S. R. Determination of Displacements Using an Improved Digital Correlation Method. Image and Vision Computating, 1983, 1(3), 133-139.

[7] Sutton, M. A., Cheng, M. Q., Peters, W. H., Chao Y. J. and McNeill, S. R. Application of an Optimized Digital Correlation Method to Planar Deformation Analysis. Image and Vision Computing, 1986, 4(3), 143-151.

[8] Sutton, M. A., McNeill, S. R., Jang, J. and Babai, M. Effects of Subpixel Image Restoration on Digital Correlation Error. Journal of Optical Engineering, 1988, 27(10), 870-877.

[9] Sutton, M. A., Turner, J. L., Bruck, H. A. and Chae, T. A. Full-field Representation of Discretely Sampled Surface Deformation for Displacement and Strain Analysis. Experimental Mechanics, 1991, 31(2), 168-177.

[10] Bruck, H. A., McNeil, S. R., Sutton, M. A. and Peters, W. H. Digital Image Correlation Using Newton-Raphson Method of Partial Differential Correction. Experimental Mechanics, 1989, 29(3), 261-267.

[11] Tung, S., Shih, M., Kuo, J., (2010), "Application of digital image correlation for anisotropic plastic deformation during tension testing", Optics and Lasers in Engineering 48(2010), 636-641

[12] F.M. Sánchez-Arévalo, T. García-Fernández, G. Pulos, and M. Villagrán-Muniz, (2009), "Use of digital speckle pattern correlation for strain measurements in a CuAlBe shape memory alloy", MATERIALS CHARACTERIZATION, 60 (2009) 775–782.

[13] Stephen R. Heinz, Jeffrey S. Wiggins, (2010), "Uniaxial compression analysis of glassy polymer networks using digital image correlation", Polymer Testing 29 (2010) 925–932

[14] S.Sozen, and M.Guler, (2011), "Determination of displacement distributions in bolted steel tension elements using digital image techniques", Optics and Lasers in Engineering 49 (2011) 1428–1435.

[15] X.F. Yao, L.B. Meng, J.C. Jin, H.Y. Yeh, (2005), "Full-field deformation measurement of fiber composite pressure vessel using digital speckle correlation method", Polymer Testing 24 (2005) 245–251.

[16] Ghiassi, B., Xavier, J., Oliveira, D.V., Lourenço, P.B., "Application of Digital Image Correlation in Investigating the Bond Between FRP and Masonry", Composite Structures (2013), doi: http://dx.doi.org/10.1016/j.compstruct.2013.06.024

[17] R.L. VijayaKumar, M.R.Bhat,C.R.L.Murthy, (2013), "Evaluation of kissing bond in composite adhesive lap joints using digital image correlation", International Journal of Adhesion & Adhesives 42 (2013) 60–68.

[18] S. Giancane*, F.W. Panella, R. Nobile, V. Dattoma, (2010), "Fatigue damage evolution of fiber reinforced composites with digital image correlation analysis", Procedia Engineering 2 (2010) 1307-1315.

[19] François Hild, Stéphane Roux, Néstor Guerrero, Maria Eugenia Marante, Julio Flórez-López, (2011), "Calibration of constitutive models of steel beams subject to local buckling by using digital image correlation", European Journal of Mechanics A/Solids 30 (2011) 1-10.

[20] Simon Rouchier, Geneviève Foray, Nathalie Godin, Monika Woloszyn, Jean-Jacques Roux, (2013), "Damage monitoring in fibre reinforced mortar by combined digital image correlation and acoustic emission", Construction and Building Materials 38 (2013) 371 – 380.

[21] Cristina Goidescu, Hélène Welemane, Christian Garnier, Marina Fazzini, Romain Brault, Elodie Péronnet, Sébastien Mistou, (2013), "Damage investigation in CFRP composites using full-field measurement techniques:

Combination of digital image stereo-correlation, infrared thermography and X-ray tomography", Composites: Part B 48 (2013) 95 – 105.

[22] Yihong He, Andrew Makeev, Brian Shonkwiler, (2012), "Characterization of nonlinear shear properties for composite materials using digital image correlation and finite element analysis", Composites Science and Technology 73 (2012) 64 – 71.

[23] H. Koerber, J. Xavier, P.P. Camanho, (2010), "High strain rate characterisation of unidirectional carbon-epoxy IM7-8552 in transverse compression and in-plane shear using digital image correlation", Mechanics of Materials 42 (2010) 1004 – 1019.

[24] Flavio de Andrade Silva, Deju Zhu, Barzin Mobasher, Chote Soranakom, Romildo Dias Toledo Filho, (2010), "High speed tensile behavior of sisal fiber cement composites", Materials Science and Engineering A 527 (2010) 544 – 552.

[25] B. Mobasher, S.D. Rajan, Image Processing Applications for the Study of Displacements and Cracking in Composite Materials, American Society of Civil Engineers, 2004.

[26] Sutton A, Jose Orteu Jean, Hubert W Schreier. Image correlation for shape motion and deformation measurements, basic concepts, theory and applications. 1st ed. New York: Springer publications; 2009.

[27] Li, V.C., Wang, S., Wu, C. (2001) "Tensile-Strain hardening behavior of polyvinyl alcohol engineered cementitious composites (PVA-ECC)." ACI Materials Journal, 98, 483-492.

[28] Mechtcherine, V., Schulze, J. (2005) "Ultra-ductile concrete – material design concept and testing." CPI Concrete Plant International, (5), 88-98.

[29] Li, V.C., Wang, S., Wu, C. (2001) "Tensile-Strain hardening behavior of polyvinyl alcohol engineered cementitious composites (PVA-ECC)." ACI Materials Journal, 98, 483-492.

[30] Lepech, M. and Li, V.C. (2005) "Design and Field Demonstration of ECC Link Slabs for Jointless Bridge Decks." In: 3rd International Conference on Construction Materials: Performance, Innovations and Structural Implications, Vancouver, British Columbia, 2005.

[31] Li, V.C. (2004) "High Performance Fiber Reinforced Cementitious Composites as Durable Material for Concrete Structure Repair." International Journal for Restoration, 10 (2), 163–180.

[32] Rokugo, H. (2005) "Applications of Strain Hardening Cementitious Composites with multiple cracks in Japan." In: Mechtcherine, V. (Ed.) Ultra-ductile concrete with short fibre – Development, Testing, Applications, Verlag, 121-133.

[33] Kim, S., Yun, H., (2011), "Crack-damage mitigation and flexural behavior of flexure-dominant reinforced concrete beams repaired with strain-hardening cement-based composite", Composites: Part B 42(2011), 645-656.

[34] Banthia, N., Bindiganavile, V., Mindess, S. (2004) "Impact and blast protection with fiber reinforced concrete." In: 6th Rilem Symposium on Fiber Reinforced Concretes – BEFIB, Varenna, Italy, 2004, 31-44.

[35] Maalej, M., Quek, S.T., Zhang, J. (2005) "Behaviour of hybrid-fibre engineered cemetitious composites subjected to dynamic tensile loading and projectile impact." Journal of Materials in Civil Engineering, 17 (2), 143–152.

[36] Yang, E., Li, V.C. (2005) "Rate dependence in engineered cementitious composites." In: HPFRCC RILEM Conference, Hawaii, 2005.

[37] Douglas, K.S., Billington, S.L. (2005) "Rate dependencies in high-performance fibre reinforced cement-based composites for seismic application." In: HPFRCC RILEM Conference, Hawaii, 2005.

[38] Boshoff, W.P., Mechtcherine, V., van Zijl, G.P.A.G. (2009) "Characterising the time-dependant behaviour on the single fibre level of SHCC: Part 2: The rate effects on fibre pull-out tests." Cement and Concrete Research, 39 (9), 787-797.

[39] Mechtcherine, V. Silva, F., Butler, M., Zhu, D., Mobasher, B., Gao, S. L., Mäder, E., "Mechanical behaviour of strain-hardening cement-based composites (SHCC) under low and high tensile strain rates", Journal of Advanced Concrete Technology, Vol. 9 No. 1, 51-62. (2011). doi:10.3151/jact.9.51

[40] Mechtcherinea, V., Silva, F.A., Müller, S., Jun, P., Filho, R.D.T., (2012), "Coupled strain rate and temperature effects on the tensile behavior of strain-hardening cement-based composites (SHCC) with PVA fibers", Cement and Concrete Research, 42(2012), 1417-1427.

[41] Naaman, E. A., Namur, G. G., Alwan, J. M., and Najm, H. S. (1991a). "Fiber Pullout and Bond Slip. I: Analytical Study." J. of Structural Eng., 117, 2769-2790.

[42] Naaman, E. A., Namur, G. G. Alwan, J. M. and Najm, H. S. (1991b). "Fiber Pullout and Bond Slip. II: Experimental Validation" J. of Structural Eng., 117, 2791-2800.

[43] Sueki, S., Soranakom, C., Mobasher, B., and Peled, A. (2007). "Pullout-Slip Response of Fabrics Embedded in a Cement Paste Matrix." J. Mater. Civ. Eng., 19(9), 718–727.

[44] Gupta P. and Banthia N. (2000). Fiber Reinforced Wet-mix Shotcrete under Impact, J. of Materials in Civil Engineering (ASCE), pp. 81-90.

[45] Banthia, N., Bindiganavile, V., and Mindess, S. (2004). Impact Blast Protection with Fiber Reinforced Concrete, Proceedings of RILEM Conference on Fiber reinforced Concrete, BEFIB, pp. 31-44.

[46] Xiao, X.R. (2008). Dynamic Tensile Testing of Plastic Materials. Polymer Testing, 27, 164-178.

[47] Xu, H., Mindess, S., and Duca, I.J. (2004). Performance of Plain and Fiber Reinforced Concrete Panels Subjected to Low Velocity Impact Loading, 6th RILEM Symposium on Fiber-Reinforced Concretes (FRC), BEFIB, Varenna, Italy, pp. 1257-1268.

[48] Zhang, J., Maalej, M., Quek, S.T., Teo, Y.Y. (2005). Drop Weight Impact on Hybrid-Fiber ECC Blast / Shelter Panels. Proceedings of Third International Conference on Construction Materials: Performance, Innovation and Structural Applications, Vancouver, Canada.

[49] Bharatkumar, B.H. and Shah, S.P. (2004), Impact Resistance of Hybrid Fiber Reinforced Mortar. International RILEM Symposium on Concrete Science and Engineering: A Tribute to Arnon Bentur, e-ISBN: 2912143926, RILEM Publication SARL.

[50] Meyers, M.A. (1994). Dynamic Behavior of Materials, John Wiley & Sons, New York.

[51] Nicholas, T. (1981). Tensile Testing of Material at High Rates of Strain. Experimental Mechanics, 21, 177-185.

[52] Kenneth, G. H. (1966). Influence of Strain Rate on Mechanical Properties of 6061.T6 Aluminum under Uniaxial and Biaxial States of Stress. Experimental Mechanics, 6(4), 204-211.

[53] Zabotkin, K., O'Toole, B. and Trabia, M. (2003). Identification of the Dynamic Properties of Materials under Moderate Strain Rates. 16th ASCE Engineering Mechanics Conference. Seattle, WA.

[54] Bastias, P.C., Kulkarni, S.M., Kim, K.Y. and Gargas, J. (1996). Non-contacting Strain Measurements during Tensile Tests. Experimental Mechanics, 78, 78–83.

[55] Bruce, D.M., Matlock, D.K., Speer, J.G. and De, A.K. (2004), Assessment of the Strain-Rate Dependent Tensile Properties of Automotive Sheet Steels. SAE, 0507.

[56] Hill, S. and Sjöblom, P. (1998). Practical Considerations in Determining High Strain Rate Matererial Properties, SAE, 981136.

[57] Fitoussi, J., Meraghni, F., Jendli, Z., Hug, G., and Baptiste, D. (2005). Experimental Methodology for High Strain Rates Tensile Behavior Analysis of Polymer Matrix Composites. Composite Science Technology, 65, 2174–2188.

[58] Hill, S.I. (2004). Standardization of High Strain Rate Test Techniques for Automotive Plastics Project, UDRI: Structural Test Group, UDR-TR-2004-00016.

[59] Society of Automotive Engineers (SAE), (2006). High Strain Rate Testing of Polymers. J2749.

[60] Borsutzki, M., Cornette, D., Kuriyama, Y., Uenishi, A., Yan, B. and Opbroek, E. (2003). Recommended Practice for Dynamic Tensile Testing for Sheet Steels. International Iron and Steel Institute: High Strain Rate Experts Group.

[61] ISO. (2003). Plastics—Determination of Tensile Properties at High Strain Rates. a draft of ISO/CD 18872.

[62] Häuβler-Combe, U., Jesse, F., Curbach, M. (2004). Textile Reinforced Composites – Oerview, Experimental and Theoretical Investigations. Proc., 5th International Conference on Fracture Mechanics of Concrete and Concrete Structures, Ia-FraMCos 204, Vail, Colorado, pp.749-756.

[63] Peled, A., and Mobasher, B. (2007). Tensile Behavior of Fabric Cement-Based Composites: Pultruded and Cast, ASCE, J. of Materials in Civil Engineering, 19(4), 340-348.

[64] Mobasher, B., Peled, A., and Pahilajani, J. (2006). Distributed Cracking and Stiffness Degradation in Fabric-Cement Composites, Materials & Structure (RILEM) J. 39(3), 317-331.

[65] Peled, A. and Bentur, A. (2003). Fabric Structure and Its Reinforcing Efficiency in Textile Reinforced Cement Composites, Composites, Part A, 34, 107-118.

[66] Kruger, M. Ozbolt, J., and Reinhardt, H.W. (2003). A New 3D Discrete Bond Model to Study the Influence of Bond on Structural Performance of Thin Reinforced and Prestressed Concrete Plates." Proc., High Performance Fiber Reinforced Cement Composites (HPFRCC4), RILEM, Ann Arbor, MI, pp.49-63.

[67] Peled, A. (2007). Textiles as Reinforcements for Cement Composites under Impact Loading, Workshop on High Performance Fiber Reinforced Cement Composites (RILEM) HPFRCC-5, (Eds. H.W. Reinhardt and A.E. Naaman), Mainz, Germany, July 10-13, pp.455-462.

[68] Butnariu, E., Peled, A., and Mobasher, B. (2006). Impact Behavior of Fabric-Cement Based Composites, Proceedings of the 8th International Symposium on Brittle Matrix Composites (BMC8) in Warsaw, October 23-25, pp.293-302.

[69] Zhu, D., Gencoglu, M., Mobasher, B. (2009). Low Velocity Impact Behavior of AR Glass Fabric Reinforced Cement Composites in Flexure. Cement and Concrete Composites, 31(6), 379-387.

[70] Farsi, D. B., Nemes, J. A. and Bolduc, M. (2006). Study of Parameters Affecting the Strength of Yarns. Journal of Physics IV, 134, 1183-1188.

[71] Wagner, H.D., Aronhime, J. and Marom, G. (1990). Dependence of Tensile Strength of Pitch-based Carbon and Para-aramid Fibres on the Rate of Strain. Proceeding of the Royal Society of London, A428, 493-510.

[72] Amaniampong, G. and Burgoyne, C. J. (1994). Statistical Variability in the Strength and Failure Strain of Aramid and Polyester Yarns. Journal of Material Science, 29, 5141-5152.

[73] Xia, Y., and Wang, Y. (1999). The Effects of Strain Rate on the Mechanical Behaviour of Kevlar Fibre Bundles: An experimental and Theoretical Study. Composites Part A, 29A, 1411-1415.

[74] Cheng, M., Chen W., Weerasooriya, T. (2005). Mechanical Properties of Kevar KM2 Single Fiber. Journal of Engineering Materials and Technology, 127, 197-204.

[75] Zhu, D., Mobasher, B., Juan Ermi, Saurabh Bansal, Rajan, S.D., Strain Rate and Gage Length Effects on Tensile Behavior of Kevlar 49 Single Yarn. Composites: Part A 43 (2012) 2021–2029, Composites Part A, 2012.

[76] Kravaev, P., Janetzko, S., Gries, T., Kang, B., Brameshuber, W., Zell, M., Hegger, J., "Commingling Yarns for Reinforcement of Concrete", 4th Colloquium on Textile Reinforced Structures (CTRS4), 2009.

[77] C. Soranakom, Multi scale modeling of fiber and fabric reinforced cement based composites, PhD dissertation, Arizona State University, 2008.

[78] Xiao, X.R. (2008). Dynamic Tensile Testing of Plastic Materials. Polymer Testing, 27, 164-178.

[79] Birkimer, D.L., and Lindemann, R. (1971), " Dynamic tensile strength of concrete materials," Journal of the American Concrete Institute, 68, 47-49.

[80] Oh, B. H. (1987), "Behavior of concrete under dynamic tensile loads," ACI Materials Journal, 84, 8-13.

[81] Rossi, P., Van Mier, J.G.M., Toutlemonde, F., Le Maou, F., and Boulay, C. (1994), "Effect of loading rate on the strength of concrete subjected to uniaxial tension," Materials Structure, 27, 260 - 264.

[82] Cadoni, E., Labibes, K., Albertini, C., Berra., M., and Giangrasso, M. (2001), "Strain-rate effect on the tensile behaviour of concrete at different relative humidity levels," Materials and Structure, 34,21 - 26.

[83] Malvar, L.J., and Ross, C.A. (1998), "Review of static and dynamic properties of concrete in tension," ACI Materials Journal, 95, 735 - 739.

[84] Zhu, D., Peled, A., and Mobasher, B. (2011), "Dynamic tensile testing of fabric - cement composites," Construction and Building Materials, 25, 385 - 395.

[85] Kim, D.J., El-Tawil, S., and Naaman, A.E. (2009), "Rate-dependent tensile behavior of high performance fiber reinforced cementitious composites," Materials and Structure, 42, 399 - 414.

[86] Zhang, J., Maalej, M., Quek, S.T., and Teo, Y.Y. "Drop Weight Impact on Hybrid-Fiber ECC Blast/Shelter Panels." Proceedings of Third International Conference on Construction Materials: Performance, Innovation and Structural Applications, Vancouver, Canada, 2005.

[87] Silva, F.A, Butler, M., Mechtcherine, Viktor., Zhu, D. and Mobasher, B. (2010), "Strain rate effect on the tensile behavior of textile-reinforced concrete under static and dynamic loading," Materials Science and Engineering A, 528(2011), 1727-1734.

[88] Zhu, D., Gencoglu, M., and Mobasher, B. (2009), "Low velocity impact behavior of AR glass fabric reinforced cement composites in flexure," Cement and Concrete Composites, 31(6), 379 – 387.

[89] Aveston, J., Cooper, G. A., and Kelly, A. (1971). "The Properties Fibre Composites," Conference Proceedings of the National Physical Laboratory, IPC Science and Technology Press Ltd., Guildford, pp. 15 – 26.

[90] Butler M, Hempel R, Schiekel M. The influence of short glass fibres on the working capacity of textile reinforced concrete. In: Hegger J,Brameshuber W,Will N, editors. Textile reinforced concrete: Proc. of the 1st International RILEM Symposium. Aachen; 2006. p. 45 – 54.

[91] Hinzen M, Brameshuber W. Influence of short fibres on strength, ductility and crack development of textile reinforced concrete. In: Reinhardt HW, Naaman AE, editors. High performance fibre reinforced cement composites (HPFRCC5). Proc. of the 5th International RILEM workshop. Mainz; 2007. p.105 – 12.

[92] Hamoush, S., Abu-Lebdeh, T. and Cummins, T., "Deflection behavior of concrete beams reinforced with PVA micro-fibers", Construction and Building Materials, 24(2010), 2285-2293.

[93] M. Hinzen, W. Brameshuber, in: M. Curbach, F. Jesse (Eds.), Textilbeton Theorie und Praxis, 4th Colloquium on Textile Reinforced Structures (CSTR4), 2009, pp. 261 – 272.

[94] R. Barhum, V.Mechtcherine, in: B.H. Oh, et al. (Eds.), "Influence of Textile Alignment, Moisture and Shape of Specimens on First Crack Load and Load Bearing Behavior of Textile Reinforced Concrete Containing Short Fibers " Fracture Mechanics of Concrete and Concrete Structures, Korea Concrete Institute, 2010, pp. 1498 – 1503.

[95] Boshoff, W.P., Mechtcherine, V. and Zijl, G., "Characterising the time-dependant behaviour on the single fibre level of SHCC: Part 2: The rate effects on fibre pull-out tests", Cement and Concrete Research, 39(2009), 787-797.